ALUMINIUM AND GOLD FUNCTIONALIZED GRAPHENE QUANTUM DOTS AS ELECTRON ACCEPTORS FOR INVERTED SCHOTTKY JUNCTION TYPE RAINBOW SOLAR CELLS

By

PENNY MATHUMBA

BSc Honours Chemistry (University of Limpopo), MSc Chemistry (University of Johannesburg)

A thesis submitted in fulfilment of the requirements for the degree of

PHILOSOPHIAE DOCTOR

In the

Department of Chemistry
Faculty of Science
University of the Western Cape, South Africa

Supervisor: Prof. Emmanuel Iwuoha
November 2019

ABSTRACT

The main aim of this study was to prepare band gap-engineered graphene quantum dot (GQD) structures which match the different energies of the visible region in the solar spectrum. These band gap-engineered graphene quantum dot structures were used as donor materials in rainbow Schottky junction solar cells, targeting all the energies in the visible region of the solar spectrum for improved solar-to-electricity power conversion efficiency. Structural characterisation of the prepared nanomaterials under solid-state nuclear magnetic resonance spectroscopy (SS-NMR) showed appearance of bands at 40 ppm due to the presence of sp^3 hybridised carbon atoms from the peripheral region of the GQD structures. Other bands were observed at 130 ppm due to the presence of polycyclic aromatic carbon atoms from the benzene rings of the GQD backbone, and around 180 ppm due to the presence of carboxylic acid carbons from oxidation due to moisture. Fourier-transform infrared resonance (FTIR) spectroscopy further confirmed the presence of aromatic carbon atoms and oxidised carbons due to the presence of C=O, C=C and -OH functional groups, concurrent with SS-NMR results. To evaluate the effect of the synthesis temperature of the electronic structure of the nanomaterials, transmission electron microscopy (TEM), ultra-violet visible spectroscopy (UV-vis), Photoluminescence (PL) and electrochemical studies were conducted. A reduction in the particle size was observed on TEM with increasing synthesis temperature, suggesting a shift/change in the electronic structure of the quantum dots; i.e., electron confinement. The UV-vis spectroscopy showed appearance of n-π* and π-π* transitions due to the sp^2-hybridised carbons in GQD benzene ring backbones, supporting the FTIR and SS-NMR results. The observed blue-shift on the photoluminescence and UV-vis spectra with respect to increasing synthesis

temperature (i.e., decreasing particle size) evidenced the quantum confinement effect and edge effects, which confirmed the existence of quantum dot structures in the materials. The obtained band gaps from the optical and electrochemical results were; 0.99 eV, 1.08 eV, 1.14 eV, 1.15 eV, 1.35 eV, 1.90 eV, 2.32 eV and 2.43 eV, all which proved to correspond to all energies in the visible region of the solar spectrum. The corresponding accepting materials (aluminium, Al; gold, Au and graphene, Gr metal nanoparticles) were prepared and physically mixed with the GQD donor materials to create the charge-transfer complexes/Schottky junction (i.e., GQD:Al, GQD:Au and GQD:Gr). The interaction between the metal nanoparticles and semiconducting graphene quantum dots was supported by the appearance of Al-C, Au-OH and C=C functional groups on FTIR. The XRD crystallographic analysis of the nanocomposites showed a retained 002 RXD plane from the graphitic structure of graphene quantum dots (GQDs). Introduction of the metal nanoparticles to the GQD structure shows a shift in the cubic structure from a primitive cubic to a face-centred cubic signifying interaction of the materials. Morphological studies of the materials showed appearance of metal nanoparticles embedded on GQD structures. When the charge-transfer properties of the materials were studied through quenching of the GQD at different metal ion concentrations, it was found that the complexes followed both the static and dynamic quenching. However, there is good electron flow between the donor (GQD) and the acceptor (metal ions). This is confirmed by the low resistance observed on the Nyquist plots.

The Schottky junction photoactive films composed of graphene quantum dots (GQDs), Aluminium (Al), gold (Au) and graphene (Gr) metals have been prepared by spin coating to establish optimal concentration and composition of these materials of interest. Amongst the prepared donor to acceptor ratios of 1:1, 1:3. 1:6 and 3:1, the 1:3 ratio was found to possess optimal electrochemical efficiency and thus was used for fabrication of the solar cells. The metal/semiconductor Schottky junction solar cells were thereafter successfully prepared and characterised. Different concentrations (i.e., 10 mg/mL, 15 mg/mL and 20 mg/mL) of the active layer were prepared for optimisation of the solar cells. The optimal concentration was found to be 20 mg/mL and was used to fabricate all other solar cell devices. When the solar cell devices were fabricated using the three different types of metals, the solar cell with GQD:Au as the active layer possessed high solar-to-electricity conversion efficiency upon light illumination. This can be ascribed to the reduction of the hot-electrons produced upon illumination by light. The results obtained in this study (2.69%) are comparable to the optimal Schottky junction solar cell, 3.8% obtained thus far.

KEYWORDS

Band-gap engineering

Graphene quantum dots

Schottky junction solar cells

Solar energy

Solar spectrum

Abstract 2

Project 2: Graphene materials for fuel cell applications

Fuel cells are electrochemical devices which transform heat of combustion of fuel (hydrogen, natural gas, methanol, ethanol, hydrocarbon, etc.) directly into electricity. The power output and lifetime of FCs are directly linked to the behaviour of the cathode, where most of the polarization losses occur, because the oxygen reduction reaction (ORR) is a slow reaction compared to the hydrogen oxidation at the anode. Therefore, cathode development requires special attention to find the best catalyst and electrode structure to combine performance and stability. Platinum is the most commonly used and active electro-catalyst for the ORR and all the Pt-group metals reduce oxygen in alkaline media according to the direct 4-electron process. However, their large-scale commercial application has been precluded due to high cost of Pt. In addition, the Pt-based electrodes suffer from low selectivity to ORR in the presence of other reactions (e.g., methanol oxidation derived from fuel crossover in FCs) and CO deactivation. Therefore, in this study, sulphur and nitrogen dual doped graphene (S,N-Gf) was evaluated for its activity for ORR under alkaline conditions against cobalt and manganese loaded graphene catalysts. Characterisation techniques such as FTIR, Raman, TEM and XRD confirmed the structure of the catalysts. When oxygen reduction reactions were conducted under alkaline conditions, it was found that the cobalt containing S,N-doped graphene exhibited the optimal activity for the production of water molecules through a $4e^-$ route. The stability and durability test of the materials were also conducted and Co/S_3N_2-GF catalyst still had high selectivity towards ORR even in the presence of methanol, which renders it attractive for the development of alkaline fuel cells.

KEY WORDS

Fuel cell

Graphene doping

Renewable energy

Oxygen reduction reactions

Spinel metal oxide impregnation

LIST OF ABBREVIATIONS

Al	Aluminium
A	Ampere
Au	Gold
Co	Cobalt
FTIR	Fourier Transform Infrared Spectroscopy
FF	Fill factor
G	Graphene
GQD	Graphene quantum dots
J_{sc}	Short circuit current density
mg/L	Milligrams per litre
Mn	Manganese
mW	Milliwatts
NP	Nanoparticles
P_{max}	Maximum Power
SEM	Scanning electron microscopy
Si	Silicon
SJSC	Schottky junction solar cell

TEM	Transmission Electron Microscopy
UV-Vis	Ultraviolent-Visible spectroscopy
V	Volts
V_{oc}	Open circuit voltage
XRD	X-ray diffraction spectroscopy

DECLARATION

I declare that **Aluminium and Gold functionalized Graphene quantum dots as Electron Acceptors for Inverted Schottky Junction type rainbow solar cells** is my own work, that it has not been submitted before for any degree or examination in any other university, and that all the sources I have used or quoted have been indicated and acknowledged as complete references.

Signature ---------- ----------

First name Middle name Surname **Day** **Month** **Year**

DEDICATION

I would like to dedicate this PhD degree to my father Johannes M. Mathumba, my mother Lillian Mathumba, my sister Mondy Mathumba and all the disadvantaged people in South Africa with no access to electricity.

ACKNOWLEDGEMENTS

I would like to acknowledge the following people and institutions

- I would like to thank Prof. Emmanuel I. Iwuoha for his guidance, encouragement and counsel throughout the entire period of my research work. I am also indebted to my colleagues Sabelo Sifuba, Tshepo Sekgobela, Ntalane Sello Seroka and Bangile Rolihlahla whose passion for their work inspired me to take my own passions seriously. I also give a special thanks to my mentor Dr. Usisipho Feleni for her exceptional mentorship during the period of my studies.

- I would also like to extend my heartfelt gratitude of appreciation to my supervisors Prof. Emmanuel I. Iwuoha, Cristina Freirre and Diana M. Fernandes, for their support and guidance during my research study.

- I am grateful to the National Research Foundation of South Africa and Erasmus Mundus Plus programme for their financial support during my studies at the University of the Western Cape and University of Porto, respectively.

- I would like to thank my family; my mother, Lillian Mathumba; my sisters, Alleta Mathumba, Mondy Mathumba, Sharlotte Mathumba and Bridget Mathumba. I will also, thank my brother Archibald S. Mathumba and my father Johannes M. Mathumba for their love, patience and support during my studies at University of the Western Cape (UWC).

- Finally, I thank the technical staff of the Department of Chemistry, University of the Western Cape for assistance with the use of research instruments. I thank the University of the Western Cape and its Department of Chemistry for providing me the opportunity to pursue my Doctoral studies.

LIST OF PUBLICATIONS

The work presented in this dissertation has been published and submitted for publication in scientific journals in partial fulfilment of University regulations

Publications

- D.M., Fernandes, P., Mathumba, A.J., Fernandes, E.I. Iwuoha, and C., Freire, (2019). Towards efficient oxygen reduction reaction electrocatalysts through graphene doping. *Electrochimica Acta*, *319*, pp.72-81.
- P. Mathumba, N. Raleie, E.I. Iwuoha (2019). Preparation of graphene quantum dots with different band gaps to match the visible region of the solar spectrum, potential for application as donor materials for solar cells (Submitted to *Journal of Solar Energy Materials and Solar Cells*)
- P., Mathumba, N., Raleie, E.I., Iwuoha (2019). Effect of S,N-dopant on graphene quantum dots for oxygen reduction reactions in fuel cells (Submitted to *Journal of Energy*)
- P., Mathumba, E.I., Iwuoha, D.M., Fernandes, C., Freire (2019). Efficient oxygen reduction reaction (ORR) electrocatalysts based on metal oxide (Submitted to *Journal of American Chemical Society*)

TABLE OF CONTENTS

Section ***Page***

LIST OF FIGURES

Figure ***Description*** ***Page***

LIST OF TABLES

CHAPTER 1

INTRODUCTION

Summary

Due to the rising human population and industrial development, the continued fossil fuel supply and consumption is approaching its physical limits. These limits are set by the planet's ability to adapt to climate change, as well as the availability of resources. To sustain the quality of life for future society, alternatives for conventional carbon-based energy sources is required. An overview of the current state of photovoltaics is presented here, with a promising solution for combating environmental problems due to the depletion of current energy sources (fossil fuels). The desirable properties of photovoltaic technology have fuelled the need to critically shift away from fossil fuel-based energy sources. Consequently, the energy produced from photovoltaics is technologically feasible (economically viable), environmental benign, sustainable, and socially equitable. The chapter provides a concise background of the study which emphasises, amongst other things, the significance of evolution from non-renewable to renewable energy sources (photovoltaic cells). The prominence is more proclaimed on the application of graphene quantum dots as electron donors to improve the efficiency of Schottky junction photovoltaic cells.

1.1 Introduction

80% of the world's energy generation is sourced from fossil fuels which are extracted from deep within the Earth's crust (Kibria et al. 2019; Barreto 2018). The world has used up more than 135 billion tonnes of crude oil to drive cars, fuel power stations and heat homes since the commercial oil drilling began in 1859 (Hahn & Passell 2010; Zendehboudi et al. 2017). That figure increases every day (i.e., from 86 million barrels a day in 2018 to 100.6 million barrels per day in 2019), but the world's gas gulping over the past two centuries has taken a catastrophic toll on the planet. Climate change, global warming and the rising of greenhouse gases' in the Earth's atmosphere are directly linked to the burning of coal, oil and gas (Wang et al. 2018; Squalli 2017; Pandey et al. 2018). As a result, the world scientists agree that we are on a path towards disaster that can only be stopped by ceasing the use of fossil fuels (Olson-Hazboun 2018; Hubacek & Baiocchi 2018; Monasterolo & Raberto 2019).

It is envisaged that growth in non-fossil energy sources will dominate electricity generation by 2060, driven by solar and wind capabilities (Tsai et al. 2017; Aldenius *et al.*, 2019). In 2014, solar and wind energy accounted only 4% of power generation, whereas by 2060 it would account for about 39% of power generation worldwide (Zendehboudi et al. 2018; Chang & Starcher 2019; Troshichev & Sormakov 2019). This present project specifically focusses on solar cells as renewable energy sources. A solar cell is any device that converts solar energy directly into electrical energy through the photovoltaic effect (Khudhair et al. 2018; Yoon et al. 2018). The photovoltaic effect was first demonstrated by Edmond Becquerel in 1839, using an electrochemical cell. The demonstration showed that

electron transitions from the valence band to the conduction band requires concentrated sunrays (i.e., energy of the photon), (Krishna *et al.*, 2019; Pérez-Tomás *et al.*, 2019).

Figure 1.1 illustrates the process by which the p-type semiconductor material and the p-n junction diode consecutively receive these energetically excited electrons via the built-in potential, while some are lost in the process. The process continues (i.e., electron flow and separation) in the p-n junction; and thus some of the light energy is converted into electric energy (Luceño-Sánchez, Díez-Pascual and Capilla, 2019).

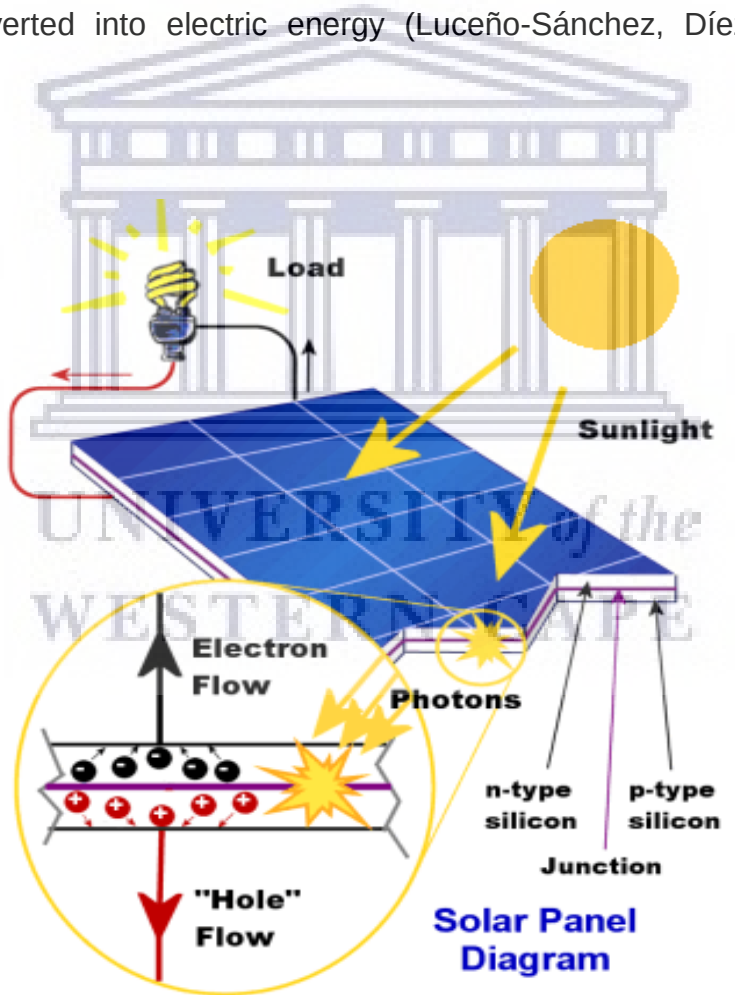

Figure 1.1: A demonstration of the photovoltaic effect in solar cells (Voudoukis, 2018).

Previously reported solar cells include the first, second and third generation solar cells. The first-generation solar cells are based on monocrystalline, polycrystalline, amorphous and hybrid solar cells (Olyaeefar, Ahmadi-Kandjani and Asgari, 2018; Li *et al.*, 2019). The monocrystalline solar cells are made of thin silicon (Si) wafers. They have highly reported solar-to-electricity conversion efficiencies up to 24.2% at low surface areas. However, they suffer from high cost of installation and decreased efficiencies at temperatures above 25 °C (Kim *et al.*, 2019; Basher et al. 2018). The polycrystalline solar cells are made from affordable materials (i.e., Si wafers in moulds), and this makes their costs to be lowered as compared to that of monocrystalline solar cells. They are also thermo-stable, meaning the temperatures do not need to be regulated. However, there is a trade-off between cost and efficiency since the efficiency decreases to 19.3% (Nabavi et al. 2017; Fébba *et al.*, 2018). This means that while the cost is reduced and made accessible to more people, the efficiency is compromised.

Amorphous solar cells are made of a thin layer of non-crystalline silicon coated on any substrate. These solar cells can work at low light intensities, can be used in small devices such as calculators and they can also be taken along to camping since they are portable. However attractive they sound, their reported efficiencies are much less than that of polycrystalline solar cells (i.e., 10%) and they also require large geographical areas for installation (Rahmani and Vatankhah, 2017; Chen et al. 2018; W. Li *et al.*, 2019). Hybrid solar cells are made of amorphous silicon, which is distributed over a crystalline silicon wafer. They offer the advantage of a good efficiency at minimal light intensities and are less likely to lose efficiencies with increased temperatures (Wang et al. 2017; Zhang *et al.*, 2020).

The three commonly known second-generation solar cells include cadmium telluride (CdTe) solar cells, amorphous silicon solar cells and copper indium gallium diselenide (GIGS) solar cells. CdTe solar cells are produced and sold worldwide due to their high affordability (R14.00/watt going to R9.80/watt) (Krasikov et al. 2016; Camacho-Espinosa *et al.*, 2019; Yan Li *et al.*, 2019). The famous GIGS solar cells offer efficiencies which are approximately 20%, however their high costs hinder them from commercialisation (Yan Li *et al.*, 2019). The high costs of the second-generation solar cells have forced researchers to shift focus to the third-generation solar cells. The third-generation solar cells are made from a variety of new materials, including nanostructured materials. This technology is highly attractive since it offers newer solar cells that are less expensive, flexible, compact, light-weight and efficient (Grace et al. 2017; Kusuma *et al.*, 2018; Ouyang, 2019). This technology is driven by material choice with good properties, including organic dyes, nanotubes, silicon wires, solar inks (using conventional printing press technologies) and conductive plastics (Grace et al. 2017; Peksu & Karaagac 2019). Due to the trade-off between the efficiency and cost of solar cells, researchers are working on a goal to improve the solar-to-electricity absorption efficiency over a wider solar spectrum (e.g., including infrared) and reduce cost by using cheap materials during fabrication.

The project is centred on the third-generation solar cells, where the quantum dot technology is used. The semiconducting nanocrystals used in the technology exhibit quantisation effects observed on the solar conversion devices. However, the conventional bimetallic quantum dots have been found notoriously toxic, non-biodegradable and environmentally unfriendly. Graphene quantum dots are quite the opposite of the former. Therefore, in this study, graphene quantum dots of

different size regimes (i.e., different band gaps) are prepared and used as the donor material for the Schottky junction solar cell. Schottky junction solar cells (SJSCs) result from contact between a metal and a semiconductor, with or without an insulating layer in-between (Alnuaimi *et al.*, 2018). They were invented in 1883 by Charles Fritts when he coated selenium with a thin layer of gold to make one of the world's first solar cells (Lamont 2012). However, since then, they have only commanded a small amount of attention from researchers and corporations. This is because the single junction employed on the architecture and the poor solar absorption of the materials used in the active layer render their solar conversion efficiencies very low and this opens room for improvement. This study therefore seeks to improve on this class of solar cells by using band gap-engineered graphene quantum dots in the active layer for improved solar-to-electricity efficiencies (i.e., improved light absorption).

1.1.1 Problem statement

The world's future energy production is currently unforeseeable as the predominantly used energy sources, i.e., fossil fuels, approach depletion. The production of greenhouse gases as by-products from burning of coal, oil and gas has prompted global warming to reach unprecedented levels worldwide. In conjunction to the already mentioned problems, the rising human population and industrial development demands for rising energy needs. This constraint demands humanity to shift focus towards finding alternative renewable energy sources. The currently available renewable energy sources under review and consideration worldwide are the wind, hydroelectricity and solar energy; which constitutes 24.5% to the total electricity generation. The world seeks to strive into an era on which the total energy production is 100% dominated by renewable energy sources. Compared to the other renewable energy sources, solar energy stands superior due to its sustainability, economic viability and its promise to reduce the emission of greenhouse gases, which renders it environmentally friendly. According to climatologists, Africa receives a high concentration of sunrays compared to other continents in the world. Therefore, the geographical location of South Africa renders it highly favourable for solar renewable energy investment (as shown in Figure 1.2). This research study therefore explores solar energy as an alternative renewable energy source to meet South Africa's future energy demands.

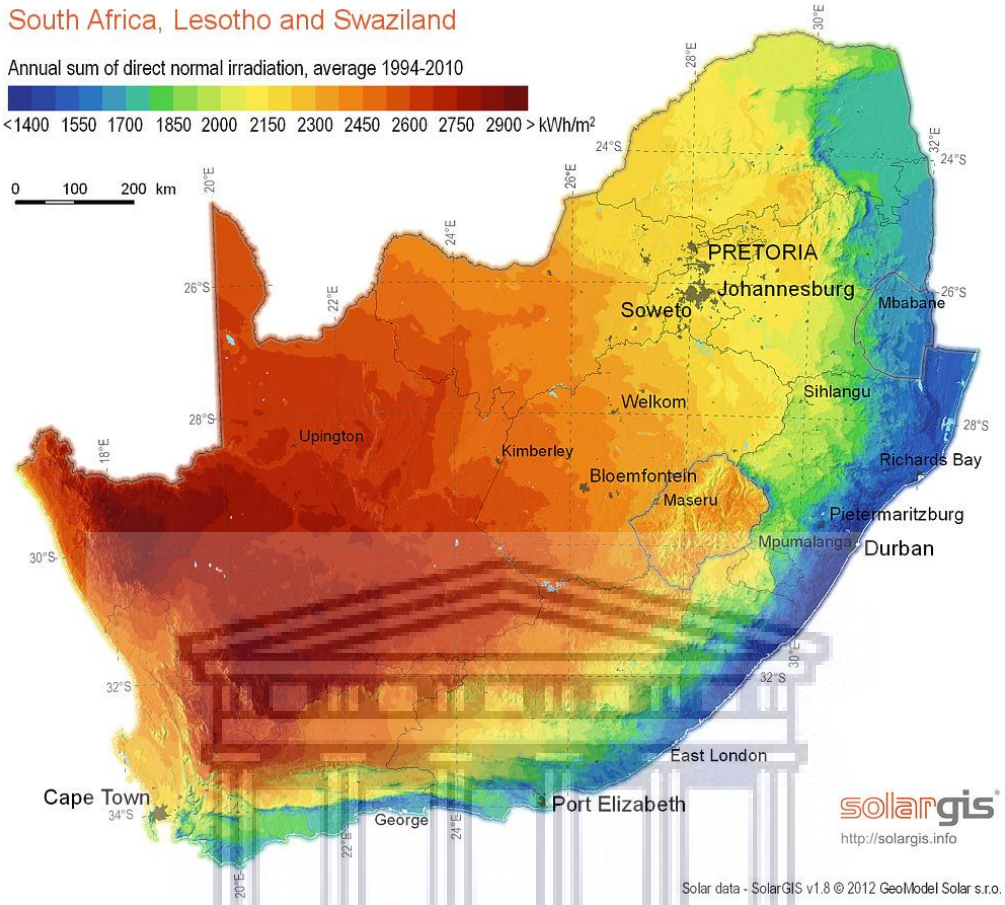

Figure 1.2: South African map showing areas with a high concentration of sunlight, favourable for solar cell installation (Grant, 2008).

1.1.2 Rationale and motivation

The solar cell markets are still lagging due to the trade-off between cost and efficiency of the currently available solar cells. Although the state-of-the-art silicon solar cells have already made it to commercialisation, there are rising concerns linked to their high costs associated to manufacturing, scarcity of silicon and complex fabrication processes. Second to the silicon solar cells in terms of solar-to-electricity conversion efficiency are organic solar cells which have high manufacturing costs, loss of material during fabrication and narrow absorption wavelengths. This therefore opens room to explore other solar cell technologies available. Schottky junction solar cells have easy fabrication processes, low material usage and present a cheap alternative renewable energy. However, they suffer from low efficiencies and this opens room for improvement. Other researchers have made some advancements to increase the efficiency of SJSCs by creating a contact between silicon and graphene, however, the use of Si during fabrication increases the cost. Therefore, in this study, graphene quantum dots of different sizes (i.e., different band gaps) are used to as the donor materials, targeting the full solar spectrum for increased solar-to-electricity conversion efficiency. These GQDs will be harvested from coal and thereafter used as the solar absorbing semiconductor nanocrystal, immobilised with gold (Au) metal nanocrystals against Aluminium (Al) metal nanocrystals in the quantum dot size range for quantum confinement effects to create the Schottky junction. Studies show that metallic contacts with a high work function possess low electron injections and low open circuit voltage (V_{oc}) of solar cell. In this study therefore, a low work function metal such as Aluminium is used

against a high work function metal such as gold to produce a Schottky junction solar cell with improved electron injections and thus improved efficiencies.

1.2 Aims and Objectives of the study

The aim of this study was to produce an effective and efficient Schottky junction photovoltaic cell made from contact between metal nanocrystals and graphene quantum dots of different band gaps to target the full solar spectrum, and thus a high energy harvesting potential. This aim was achieved through execution of the following objectives, which were:

- To prepare graphene-based quantum dots from a three types of cheap coal materials, namely; anthracite coal, bituminous coal and coke.

- To characterise of the prepared graphene quantum dots using techniques such as; Transmission Electron Microscope, TEM (to evaluate the morphology and size of the quantum dots as a function of the band gap), Ultraviolet visible, UV-vis, spectroscopy (to evaluate the band gap of the nanomaterials) and Photoluminescence, PL, spectroscopy (to evaluate the optical properties of the quantum dots as a function of the band gap, since optical properties of the QD's can be fine-tuned by the QD's size).

- To evaluate the purity of the prepared GQDs using solid state ^{13}C nuclear magnetic resonance spectroscopy (SS-^{13}C-NMR).

- To prepare Aluminium and gold metal nanoparticles using the sol-gel methods and evaluate them using characterisation techniques such as; TEM and XRD.

- To determinate the redox potentials using electrochemical studies which involve Cyclic Voltammetry (CV) and Electrochemical Impedance spectroscopy (EIS).

- To use the actual prepared nanomaterials in the fabrication of inverted SJSC

- To determine the power conversion efficiency (PCE) was determined by illuminating the cells with simulated sunlight AM1.5 with specific voltage and measuring current output.

1.3 Thesis outline

The following dissertation outline gives a brief description of the content on chapters to follow:

Chapter 1: The chapter gives a brief introduction into the study presented in the thesis. It gives a brief introduction on the current energy crisis and then an introduction into our study. The aim of the study is also discussed in the chapter, including the objectives that were followed.

Chapter 2: This chapter gives intensive literature of the overall study. Detailed literature on the electron flow in Schottky junction solar cells is discussed. Problems associated with the currently available energy sources are outlined, and an alternative material for application in energy is also discussed. Also, the literature on processes involved in these technologies are discussed in this section of the thesis.

Chapter 3: The results and discussions on the structural characterisations of the graphene quantum dot materials prepared for solar energy applications as donor materials are discussed in detail in this chapter.

Chapter 4: The results and discussions on the prepared redox couple, Schottky junction materials (metal-graphene quantum dots) prepared in Chapter 3 are discussed.

Chapter 5: Fabrication and characterisation of the Schottky junction solar cell is also discussed on and the power output of the device is also evaluated**.**

Chapter 6: The chapter deals with the application of graphene-based materials in renewable energy processes (i.e., oxygen reduction reactions in fuel cells). The analytical methods, experimental procedure, results, discussion and conclusions are explained.

Chapter 7: Conclusions based on interpretations and discussions in Chapter 4, Chapter 5 and Chapter 6 are drawn. Furthermore, recommendations for future work are presented in this section.

References: All literature cited in this thesis is listed in this section, at the end of each chapter.

Appendix: Consists of raw data and other results obtained during this study.

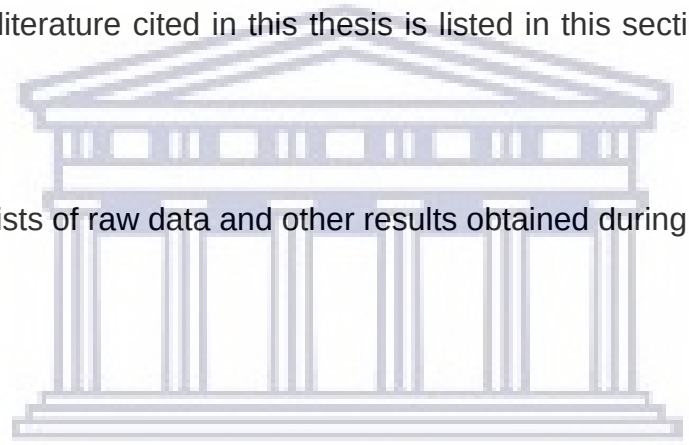

References

Aldenius, M. *et al.* (2019) 'BP Technology Outlook' *BP Energy Outlook 2019*, 134, p. 43.

Alnuaimi, A. *et al.* (2018) 'High performance graphene-silicon Schottky junction solar cells with HfO2 interfacial layer grown by atomic layer deposition' *Solar Energy*, 164, pp. 174–179.

Barreto, R.A. (2018) 'Fossil fuels, alternative energy and economic growth', 75, pp.196–220.

Basher, M.K. *et al.* (2018) 'Study and investigation of phosphorus doping time on emitter region for contact resistance optimization of monocrystalline silicon solar cell' *Results in Physics*, 10, pp.205–211.

Camacho-Espinosa, E. *et al.* (2019) 'All-sputtered CdTe solar cell activated with a novel method' *Solar Energy*, 193, pp. 31–36.

Chang, B. & Starcher, K. (2019) 'Evaluation of wind and solar energy investments in Texas' *Renewable Energy*, 132, pp.1348–1359.

Chen, A., Yossef, M. & Zhang, C. (2018) 'Strain effect on the performance of amorphous silicon and perovskite solar cells' *Solar Energy*, 163, pp.243–250.

Fébba, D. M. *et al.* (2018) 'Impacts of temperature and irradiance on polycrystalline silicon solar cells parameters' *Solar Energy*, 174, pp. 628–639.

Garca-Santamara, F. *et al.* (2009) 'Suppressed auger recombination in “Giant” nanocrystals boosts optical gain performance' *Nano Letters*, 9, pp.3482–3488.

Grace, T. *et al.* (2017) 'Use of Carbon Nanotubes in Third-Generation Solar Cells' *Industrial Applications of Carbon Nanotubes*, pp.201–249.

Grant, K. (2008) 'Concentrated Solar Power in South Africa' p. 26.

Hagfeldt, A. & Graetzel, M. (1995) 'Light-Induced Redox Reactions in Nanocrystalline Systems' *Chemical Reviews*, 95, pp.49–68.

Hubacek, K. & Baiocchi, G. (2018) 'Fossil Fuel Assets May Turn Toxic' *Joule*, 2(8), pp.1407–1409.

Hagfeldt, A. & Graetzel, M. (1995) 'Light-Induced Redox Reactions in Nanocrystalline Systems' *Chemical Reviews*, 95, pp.49–68.

Hubacek, K. & Baiocchi, G. (2018) 'Fossil Fuel Assets May Turn Toxic' *Joule*, 2(8), pp.1407–1409.

Hahn, R. & Passell, P. (2010) 'The economics of allowing more U.S. oil drilling' *Energy Economics*, 32, pp.638–650.

Hopfenberg, R. (2019) 'Population Density and Redistribution of Food Resources' *Encyclopedia of Food Security and Sustainability*, pp.26–30.

Horváth, Z.J. *et al.* (2002) 'Modification of Al/Si interface and Schottky barrier height with chemical treatment' *Applied Surface Science*, 190, pp.441–444.

Jakob, M., Levanon, H. & Kamat, P. V. (2003) 'Charge distribution between UV-irradiated TiO2 and gold nanoparticles: Determination of shift in the Fermi-level' *Nano Letters*, 3, pp.353–358.

Krishna, J. V. S. *et al.* (2019) 'Recent Advances on Porphyrin Dyes for Dye-Sensitized Solar Cells' *Dye-Sensitized Solar Cells*, pp. 231–284.

Khudhair, A.M., Ajeel, F.N. & Mohammed, M.H. (2018) 'Engineering and design of simple models from dye-sensitive of solar cells and photovoltaic cells applications: Theoretical study' *Chemical Physics Letters*, 713, pp.166–171.

Kibria, A., Akhundjanov, S.B. & Oladi, R. (2019) 'Fossil fuel share in the energy mix and economic growth' *International Review of Economics & Finance*, 59, pp.253–264.

Krasikov, D.N. et al. (2016) 'Study of optimization options for second generation solar cell materials by multilevel modelling' *Modern Electronic Materials*, 2, pp.66–69.

Kim, C. U. *et al.* (2019) 'Optimization of device design for low cost and high efficiency planar monolithic perovskite/silicon tandem solar cells' *Nano Energy*, 60, pp. 213–221.

Li, Y. *et al.* (2019) 'Crack detection in monocrystalline silicon solar cells using air-coupled ultrasonic lamb waves' *NDT & E International*, 102, pp. 129–136.

Li, W. *et al.* (2019) 'Fabrication and characteristics of N-I-P structure amorphous silicon solar cells with CdS quantum dots on nanopillar array' *Physica E: Low-dimensional Systems and Nanostructures*, 109, pp. 152–155.

Li, Yan *et al.* (2019) 'Enhance short-wavelength response of CIGS solar cell by CdSe quantum disks as luminescent down-shifting material' *Solar Energy*, 193, pp. 303–308.

Luceño-Sánchez, J. A., Díez-Pascual, A. M. and Capilla, R. P. (2019) 'Materials for photovoltaics: State of art and recent developments' *International Journal of Molecular Sciences*, 20, p. 976.

Monasterolo, I. & Raberto, M., (2019) 'The impact of phasing out fossil fuel subsidies on the low-carbon transition' *Energy Policy*, 124, pp.355–370.

Monasterolo, I. & Raberto, M. (2019) 'The impact of phasing out fossil fuel subsidies on the low-carbon transition' *Energy Policy*, 124, pp.355–370.

Nabavi, S.R. et al. (2017) 'Monte-Carlo simulation of the cofiring process in polycrystalline silicon solar cells: Effects of material heterogeneity and thickness uncertainties' *Solar Energy Materials and Solar Cells*, 170, pp.263–277.

Olyaeefar, B., Ahmadi-Kandjani, S. and Asgari, A. (2018) 'Classical modelling of grain size and boundary effects in polycrystalline perovskite solar cells' *Solar Energy Materials and Solar Cells*, 180, pp. 76–82

Olson-Hazboun, S.K., (2018). "Why are we being punished and they are being rewarded?" views on renewable energy in fossil fuels-based communities of the U.S. west. *The Extractive industries and Society*, 5(3), pp.366–374.

Pandey, B., Gautam, M. & Agrawal, M., (2018) 'Greenhouse gas emissions from coal mining activities and their possible mitigation strategies' *Environmental Carbon Footprints*, pp.259–294.

Pérez-Tomás, A. *et al.* (2019) 'Giant bulk photovoltaic effect in solar cell architectures with ultra-wide bandgap Ga2O3 transparent conducting electrodes' *Materials Today Energy*, 14, p. 100350.

Peksu, E. & Karaagac, H., (2019) 'A third-generation solar cell based on wet-chemically etched Si nanowires and sol-gel derived Cu2ZnSnS4 thin films' *Journal of Alloys and Compounds*, 774, pp.1117–1122.

Rand, B.P. et al. (2007) 'Solar Cells Utilizing Small Molecular Weight Organic Semiconductors' *Prog. Photovolt: Res. Appl.*, 15, pp.659–676.

Rahmani, A. and Vatankhah, S. (2017) 'Improving the Efficiency of Thin Film Amorphous Silicon Solar Cell by Changing the Location and Material of Plasmonic Metallic Nanostructures' *Energy Procedia*, 141, pp. 8–12.

Royston, S., Selby, J. & Shove, E. (2018) 'Invisible energy policies: A new agenda for energy demand reduction' *Energy Policy*, 123, pp.127–135.

Squalli, J. (2017) 'Renewable energy, coal as a baseload power source, and greenhouse gas emissions: Evidence from U.S. state-level data' *Energy*, 127, pp.479–488.

Subramanian, V., Wolf, E.E. & Kamat, P. V. (2004) 'Catalysis with TiO2/Gold Nanocomposites. Effect of Metal Particle Size on the Fermi-level Equilibration' *Journal of the American Chemical Society*, 126, pp.4943–4950.

Troshichev, O.A. & Sormakov, D.A. (2019) 'PC index as a proxy of the solar wind energy that entered into the magnetosphere: 4. Relationship between the solar wind dynamic pressure (PSW) impulses and PC, AL indices' *Journal of Atmospheric and Solar-Terrestrial Physics*, 182, pp.200–210.

Tsai, S.-B. *et al*. (2017) 'Models for forecasting growth trends in renewable energy' *Renewable and Sustainable Energy Reviews*, 77, pp.1169–1178.

Wang, J. *et al*. (2018) 'The spatiotemporal features of greenhouse gases emissions from biomass burning in China from 2000 to 2012' *Journal of Cleaner Production*, 181, pp.801–808.

Wang, W. *et al*. (2017) 'Hybrid solar cells from Sb2S3 nanoparticle ink' *Solar Energy Materials and Solar Cells*, 172, pp.335–340.

Yoon, S. *et al.* (2018) 'Photoreflectance study on the photovoltaic effect in InAs/GaAs quantum dot solar cell' *Current Applied Physics*, 18(6), pp.667–672.

Zendehboudi, A., Baseer, M.A. & Saidur, R. (2018) 'Application of support vector machine models for forecasting solar and wind energy resources: A review' *Journal of Cleaner Production*, 199, pp.272–285.

Zendehboudi, S. *et al.* (2017) 'Exploration and Drilling in Shale Gas and Oil Reserves' *Shale Oil and Gas Handbook*, pp.81–121.

Zhang, T. *et al.* (2020) 'Recent advances in highly efficient organic-silicon hybrid solar cells' *Solar Energy Materials and Solar Cells*, 204, p. 110245.

CHAPTER 2

LITERATURE REVIEW

Summary

Global warming as well as the depletion of fossil fuels on the Earth's crust has made the world to shift to renewable energy sources such as solar, hydro-energy and wind. Solar energy stands superior compared to the other energy sources due to environmental friendliness, low carbon emissions and the geographical location of the study (i.e., South Africa). A solar cell is any device that can convert solar energy directly into electrical energy. In most cases, semiconductors (p and n-doped) are used in the active layer as the solar absorbing materials in the active layer. The electrical energy generation starts with absorption of light energy on the device active layer, then the production of electron and hole pairs in the semiconductors and finally charge carrier separation. Charge separation usually occurs on the p-n junction. However, in this study, a metal-semiconductor junction (Schottky junction) produced from metal-graphene quantum dots was used in the active layer for charge carrier separation. Therefore, the chapter presents an immense overview of concepts which were briefly introduced in the previous chapter. Amongst others, these concepts include: the working principles and the charge separation of Schottky junction solar cells. This is followed by the important properties and parameters involved in photovoltaic cells.

Application of Schottky junction as a charge separator in the development of solar cells for renewable energy

Abstract

Schottky junction solar cells result from contact between a semiconductor and a metal. It is envisaged that introduction of an impurity energy level in the band gap (i.e., doping/decreasing the bandgap energy by creating a Schottky junction) will increase the efficiency of solar cells. The impurity can absorb low energy photons, improving the power conversion efficiency of the cell. However, research indicates that the reported power conversion efficiencies of Schottky junction solar cells thus far are very low; linked to the primary processes which occur within the solar cell. Charge separation processes in Schottky junction solar cells (SJSC) which involve the transfer of electrons from an excited semiconductor to a metal nanoparticle have not been extensively discussed in literature. This is because the low power conversion efficiencies of these solar cells hinder them from commercialisation. In this chapter, the working principles, primary processes, as well as how these processes influence the basic properties of SJSC are discussed.

2.1 Brief history of Schottky junction solar cells (Historical background of Schottky junction solar cells)

The first solar cell was a Schottky junction device made from selenium semiconductor which was sandwiched between gold and another metal and this architecture was built by Charles Fritts in 1894 (Sudhakar *et al.*, 2018). Research and development on solar cells remained low until the 1950s, when the high quality silicon became available, fuelling advancements in homojunction architectures (Arabpour Roghabadi *et al.*, 2018; Ono, Qi and Liu, 2018). Solar cell research was focussed on space applications until the late 1970's when they were developed for terrestrial use commercially (Lv *et al.*, 2018; Zhao *et al.*, 2018). Schottky junction solar cells (SJSC) offer improved electrical and optical properties which promise to drive them to commercialisation (PCE ≥ 15%) (Ansari *et al.*, 2019; Shin *et al.*, 2019). As compared to normal p-n junction solar cells, SJSCs promise a wealth of desirable properties such as; improved charge separation, a higher photocurrent and photovoltage (Ye *et al.*, 2011; Nematpour and Nikoufard, 2018; Qiu *et al.*, 2018). However, since discovery, they have only commanded a small amount of attention from researchers and corporations due to their low power conversion efficiencies caused by the solar cell's limited absorption in the solar spectrum (Liu, Stradins and Wei, 2016; Ju *et al.*, 2018). The power conversion efficiency (PCE) of SJCS is affected by factors such as low barrier height (Φ), low open circuit voltage (V_{oc}) and low short circuit current (J_{sc}). As equation [2.1] depicts, an increased PCE in solar cells is usually linked to high V_{oc} and high J_{sc} with respect to the following equation:

$$\eta = \frac{FF.V_{oc}.J_{sc}}{P_i} \qquad [2.1]$$

where FF is the fill factor, Pi is the incident power and η is the power conversion efficiency (Carey *et al.*, 2015; Zhang *et al.*, 2019). Electron injection also influences the PCE of solar cells, since it governs the speed of electron transport. This chapter explores the parameters affecting the electron injection on Schottky junction solar cells. Both p-n junctions and Schottky junction solar cells were extensively researched, and the metal-insulator-semiconductor inversion layer (MIS-IL) devices achieved an optimal efficiency of 17.6% (Green and Godfrey, 1976; Marnadu *et al.*, 2019). Since Godfrey and Green's high performing MIS structure, solar cell designs have been explored extensively by exploiting advances in polymer science for organic devices, using new technologies to fabricate high quality thin film structures, developing novel light trapping techniques, and creating hybrid structures. The chemical and physical processes that occur in photovoltaics need to be understood to understand developments occurring in their research.

2.2 The working principle of a solar cell

To select the materials suitable for application in solar cells, the band gap of the materials should be explored first. Large bandgap semiconductors are suitable for collection of high energy photons, while small bandgap materials waste high energy photons as heat (Lee, Lee and Park, 2014; Ahmad *et al.*, 2018; Zhang *et al.*, 2018). Therefore, small bandgap materials are ascribed to an infrared absorption layer (low energy) in multi-junction solar cells. The energy from the solar spectrum has an average temperature of 5526,85 °C, however the radiation received at the top of the Earth's atmosphere is different from that in space due to interferences (i.e., enhanced absorption and scattering from gas and water vapor and the oblique angle at which the radiation hits the terrestrial surface) (Sun, Sun and Xie, 2018). Shown

in **Figure 2.1** are the relevant solar spectra at the top and bottom of earth's atmosphere compared to a 5250 °C black body spectrum.

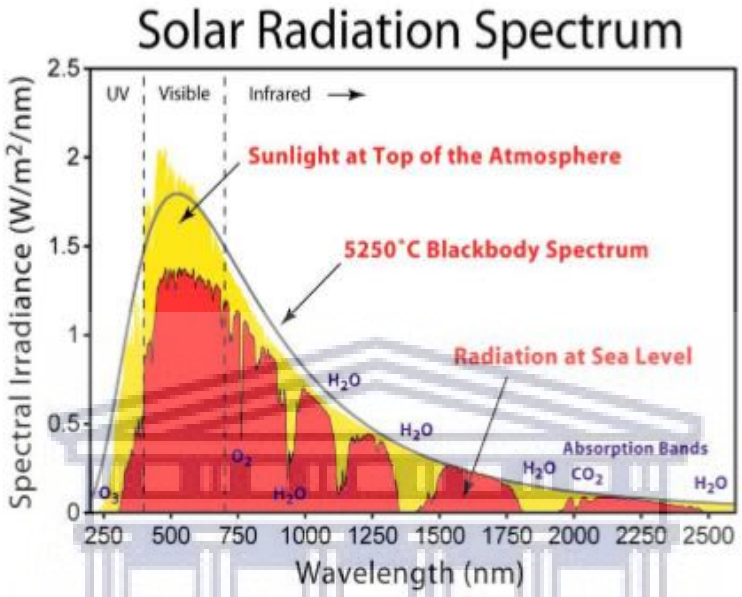

Figure 2.1: The solar spectrum received at the surface of the Earth and outside the Earth's atmosphere. Image created by Robert A. Rohde for Global Warming Art (Ipung and Tjandrasa, 2017).

Comparisons of solar cell power conversion efficiencies are only valid if all the devices have been tested under the same conditions. To create consistency among reported performances, scientists have agreed upon a solar spectrum corresponding to the average radiation received at the mid-latitudes, Air Mass 1.5 Global (AM1.5G). Equivalent to 100 mW/cm^2, this spectrum approximates the solar irradiance at the Earth's surface when the sun hits the Earth at angle of 48.2° and accounts for scattering by the atmosphere. Zero atmospheres (AM0) is the solar irradiance at the top of the atmosphere (roughly equivalent to a blackbody spectrum at 5800K), a higher fluence that overestimates photon flux for solar cell installations in the United States of America. Absorption of a photon on the semi-conducting

material of a solar cell excites an electron to the conduction band, leaving behind a hole in the valence band. Extraction of this electron only occurs if there is a driving force moving the electron or hole towards the electrodes. Extraction of the charges is predicated on transport of the charge to the electrodes, necessitating an internal mechanism to move the photo-generated carriers. While both drift (due to an internal electric field) and diffusion (due to concentration gradient) can contribute to the current, the former is more efficient at quickly separating electron hole pairs and ferrying them to their irrespective electrodes. This driving force is found within diodes, and the total current in a solar cell can be represented by the Shockley diode equation with an additional term corresponding to the photocurrent:

$$J_{total} = J_{photo} + J_{diode} \quad [2.2]$$

$$J_{total} = J_0 \exp(qVkT - 1) \quad [2.3]$$

where J_0 is the dark current and it gives important information regarding recombination at the junction. The binding energy of the electron hole pair varies depending on the absorber material: in silicon it is only 99.4 eV, low enough for the pair to be dissociated at room temperature. In contrast, the binding energy in organic materials is on the order of 0.5 1 eV, necessitating a mechanism for dissociation to separate and then extract the photo-generated carriers.

Schottky junction solar cells are like p-n junction solar cells, the only difference is that they have one semiconductor replaced with a metal in the active layer. The equilibration of the metal with the semiconductor creates the depletion layer in-between, which must be made so thick that it is opaque. To get light to the semiconductor, the metal is patterned as a grid of narrow lines to allow the light to get into the semiconductor between the opaque lines. Schottky junctions are also majority carrier devices fabricated with low temperature processes, but up until the

mid-1970s, they have suffered from lower open circuit voltages (V_{oc}) than p-n junction solar cells. This low V_{oc} is partly due to the higher dark current inherent in devices that rely on thermionic emission of majority carriers for transport across the junctions (as in Schottky junctions). Moreover, the surface states that pin the Fermi-level also increase recombination and dark current. A V_{oc} and corresponding low PCE kept Schottky junction devices from competing with p-n solar cells until Godfrey and Green developed a 17.6% metal-insulator-semiconductor (MIS) PV cell with an open circuit voltage of over 0.65V (Green and Godfrey, 1976). This excellent performance was discovered through introducing a thin (<2nm) insulating layer between the metal and semiconducting layer, passivating the silicon surface and reducing recombination while negligibly affecting current transport.

2.2.1 Preparation of SJSC

Traditional solar cells produce electricity from the internal potential difference created at the p-n junction (Liu *et al.*, 2016; Fatima Rasheed and Suresh Babu, 2019; Pylypova *et al.*, 2019). Consequently, Schottky junction solar cells create the internal potential difference at the interface between the metal and the semiconductor. When a metal and a semiconductor are joined, two possible types of contact can result, depending on the combination of metal and semiconductor used (Gupta, Rajawat and Malik, 2019; Huang *et al.*, 2019). The contact may be rectifying, which only allows current to pass in one direction (Zhao *et al.*, 2018). Alternatively, it could be Ohmic, in which case current can pass in either direction (Xie *et al.*, 2010; He *et al.*, 2019). This metal-semiconductor interface is governed by the difference in the work function between the metal and the semiconductor

(Sutty, Williams and Aziz, 2013; Jayenta Singh *et al.*, 2019). The semiconductor might be p-type or n-type, depending on the type of doping subjected to (Adaine, Ould Saad Hamady and Fressengeas, 2016; Lancellotti *et al.*, 2016). The interface between a metal and semiconductor causes a shift in the Fermi-level to align at equilibrium as shown in **Figure 2.2** below (Barala, Bhati and Kumar, 2017; Almadori *et al.*, 2019).

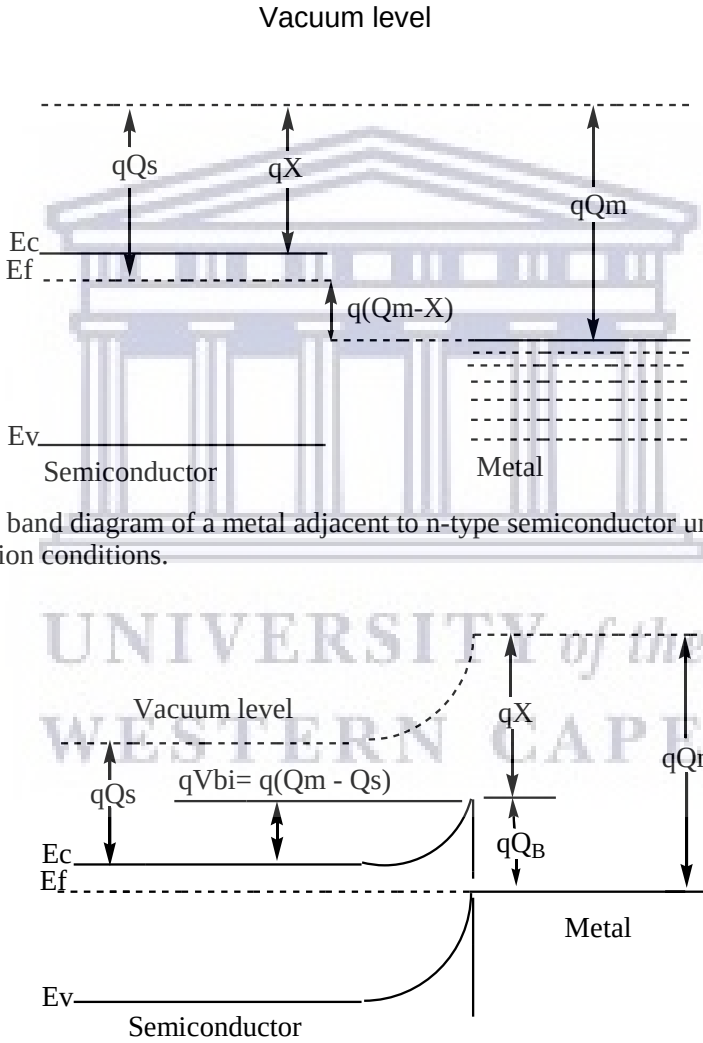

a) Energy band diagram of a metal adjacent to n-type semiconductor under thermal equilibration conditions.

b) Metal-semiconductor contact in thermal equilibrium

Figure 2.2: Formation of the contact between a metal and semiconductor for the Schottky junction solar cells.

Since discovery, researchers have been working on improving the efficiency of Schottky junction solar cells from 0% to 40% power conversion efficiency. A lot of focus has been recently shifted to graphene/silicon based Schottky junction solar cells due to the attractive properties of graphene and the fact that silicon is already commercial. Currently, Si the predominantly used material for commercial solar cells due to its compatibility with conventional semiconductor device processes. Unfortunately, its high refractive index (approximately 3.5) prevents electron-hole pairs from being efficiently generated, and this limits the PCE of Si solar cells. Graphene is one of the fascinating two-dimensional materials that potential applications in post-CMOS and other novel optoelectronic devices. Semiconductor-graphene Schottky junctions have been widely evaluated for their possible applications in chemical/biological sensors, barrister, photo-detectors and solar cells. Nanostructured Si is recognized superior compared to other semiconducting nanomaterials for the generation of graphene-based Schottky junctions due to its compatibility with the existing Si CMOS processes.

2.3 The SJSCs processes that influence the PCE of the solar cell devices

The power conversion efficiency (PCE) is a widely used parameter to characterise the solar cell's performance (Liu *et al.*, 2019; Li *et al.*, 2019). This efficiency is usually extrapolated from the photocurrent-voltage curve as can be seen in **Figure 2.3**, and typically calculated using equation [2.1]. The optimal power generated is obtained from the product of J_{max} and V_{max}, as shown on **Figure 2.3.**

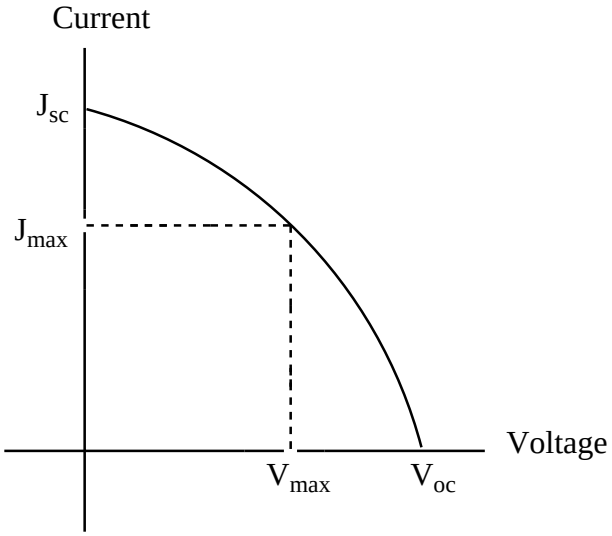

Figure 2.3: Representative photocurrent-voltage (J-V) curve of solar cell

The Fill factor is given by the ratio of ($J_{max}V_{max}/J_{sc}V_{oc}$) (Kiermasch *et al.*, 2019; Xie *et al.*, 2019). The relationship between the processes and parameters are discussed in the following sections. The spectral response of the solar cells with respect to the type of light used is also important (i.e., monochromatic light of polychromatic light). Monochromatic light is usually used to characterise the mechanism of solar cells.

2.3.1 Operational principles

2.3.1.1 Primary processes

The primary processes that occur on Schottky junction solar cells are illustrated in **Figure 2.4**. When a semiconductor and a metal are in contact, Fermi-level equilibration is induced. Electron storage within the particles may occur if the metal in contact with the semiconductor quantum dot is also in the particulate form (Hu *et al.*, 2016; Singh *et al.*, 2018). For example, gold nanoparticles possess the property of storing electrons in a quantised way. Electron storage within the gold nanoparticles is facilitated by the double layer charging around these metal

nanoparticles. Photo-generated electrons are distributed between the semiconductor and metal nanoparticles when they are in contact (Choi, Chen and Kamat, 2012; Yu *et al.*, 2018; Anjana, Bindhu and Rakhi, 2019; Yang *et al.*, 2019). The resultant Fermi-level of the composite shifts closer to the conduction band of the semiconductor as may be seen in **Figure 2.4**, since the electron accumulation increases the Fermi-level of the metal to more negative potentials.

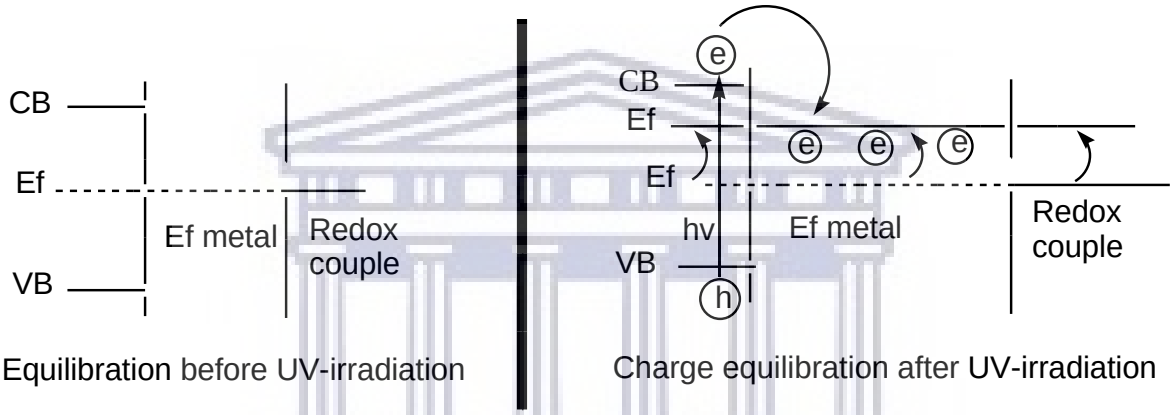

Figure 2.4: Mechanism of electron flow on a Schottky junction (semiconductor-metal) solar cells, before and after irradiation with UV light.

Improved charge separation and more reductive power for the composite system is supported by the negative shift in the Fermi-level (Sinha and Lee, 2014; Zhang *et al.*, 2018). This negative shift in the Fermi-level has been predicted to improve the performance of the solar cell and thus the PCE.

2.3.1.2 Open-circuit voltage (V_{oc})

The open circuit voltage is the voltage between the terminals of an open circuit. In order to drive the efficiency of Schottky junction solar cells to commercialisation (PCE ≥ 15%), an attractive strategy is to improve the V_{oc} without losing other properties such as the J_{sc} and FF of the solar cells (Auf der Maur and Di Carlo, 2019; Venkatesh *et al.*, 2019). The V_{oc} of Schottky junction solar cells usually undergo degradation under stress, caused by aging, prolonged irradiation, elevated temperature, long term bias and air moisture exposition (Darvishzadeh *et al.*, 2016; Alnuaimi *et al.*, 2018; Kanale *et al.*, 2019; Song, Yu and Yang, 2019). The open circuit voltage mathematical expression is:

$$V_{oc} = \frac{nkT}{q} \ln\left(\frac{J_{sc}}{J_0} + 1\right) \qquad [2.4]$$

…where nkT/q = 26 meV and n=1,2 is the ideality factor (1 for biomolecular recombination and 2 for Shockley-Read-Hall, SRH) (Bayhan and Kavasoglu, 2007; Singh and Ravindra, 2012). The low V_{oc} in Schottky junction solar cells is associated with a poor energy barrier for hole injection into the electron extraction electrode.

2.3.1.3 Short-circuit current density

Short circuit current is the highest current in the solar cell that can exist under short circuit conditions, when the voltage is zero (Darvishzadeh *et al.*, 2017). J_{sc} has a high dependence on the spectrum of the incident light, optical properties, collection probability, the area of the solar cell and the number of photons striking the solar cell (Konovalov, Strikha and Breitenstein, 1998; Scagliotti *et al.*, 2019). Therefore, this short circuit current is increased in order to remove the dependence of the solar cell on the area of the solar cell (Breitenstein, Frühauf and Turek, 2016; Shi *et al.*,

2018). The short circuit current density is directly proportional to the surface passivation and diffusion length. For a solar cell with a perfectly passivated surface and uniform generation, the short circuit current can be approximated as;

$$J_{sc} = qG(L_n + L_p) \quad [2.5]$$

…where, G is the generation rate, L_n and L_p are the electron and hole diffusion lengths (Xu *et al.*, 2018). Alternatively, the J_{sc} may be related to other efficiencies by the following expression;

$$J_{sc} \propto (\Phi_{LH} * \Phi_G * \Phi_C) \quad [2.6]$$

…where, Φ_{LH} is the solar cell's light harvesting efficiency, Φ_G is the generation efficiency of electron under light irradiation and Φ_C is the collection efficiency from the device to the external circuit (Quan *et al.*, 2018; Azzouzi, Kirchartz and Nelson, 2019). For Schottky junction solar cells, the Φ_{LH} is expected to increase when semiconductor materials of smaller band gaps are used (Lee, Lee and Park, 2014). This makes it possible to harness energy from light of lower wavelengths. A large barrier height in Schottky junction solar cells eliminates hot electrons. Whilst on the p-n junction solar cells, these electrons are lost as heat, and this damages solar cells. Literature reports show that the theoretical Shockley-Queisser limit is 33% (Choi *et al.*, 2013; Tian *et al.*, 2019). However, the maximum efficiency of Schottky junction solar cells reported in literature by Li *et. al.* (2014) is 15.5% for a SJSC based on graphene/GaAs hetero-structures (Li *et al.*, 2014). This opens room for improvement in the efficiency of Schottky junction solar cells.

2.3.1.4 Power conversion efficiency

The power conversion efficiency of solar cells is the most important part as it dictates the success of the solar cell architecture (Namvar *et al.*, 2016; Datt *et al.*, 2019). It also contains crucial information about the primary processes that occur in a solar cell. The power conversion efficiency of solar cells obtained at a wavelength, PCE(λ_{ex}), can be calculated as;

$$\mathrm{PCE}(\lambda_{ex}) = \Phi A(\lambda_{ex}) * \Phi_{inj} * \Phi_{reg} * \Phi_{c} \quad [2.7]$$

…where, $\Phi A(\lambda_{ex})$ is the light harvesting efficiency at a particular wavelength (Baxter and Aydil, 2005; Manjceevan and Bandara, 2018; Zheng *et al.*, 2018). It is worth noting that, $\Phi A(\lambda_{ex})$ is not equal to $\Phi_{LH,}$ since Φ_{LH} is the light harvesting efficiency at a single wavelength. If the absorbance at λ_{ex} is defined as A, $\Phi A(\lambda_{ex})$ can be written as $(1\text{-}10^{-A})$ which can be evaluated using conversional absorption spectroscopy (Manjceevan and Bandara, 2018; Y. Zhang *et al.*, 2019). The efficiency of light reflection on the surface of the glass on the solar cell should be included in all calculations of $\Phi A(\lambda_{ex})$ for a detailed analysis. The product of Φ_{inj} Φ_{reg} Φ_{C} can be obtained from the measurements of the power conversion efficiency, from which the primary processes of Schottky junction solar cells can be discussed.

2.3.2 Electron injection efficiency

2.3.2.1 Methods for evaluating electron injection

Most inorganic solar cells, crystalline Si solar cells and Schottky junction solar cells today are based on the classical Schottky diode equation that was derived under the assumption of continuous energy band semiconductor systems where electron-hole pairs dissociate immediately upon their generation and travel at high charge mobility (Güllü *et al.*, 2010; Sinha and Lee, 2014; Missoum *et al.*, 2016).

$$J = J_S\left(\frac{V_D}{e^{nV_T}} - 1\right)^1 \qquad [2.8]$$

…where V_D is the voltage across the diode, V_T is the thermal voltage, n is the ideality factor J is the diode current and J_S is the reverse bias. However, electron flow in Schottky junction solar cells does not follow this trend since they have a poor electron barrier for hole injection into the electron extraction electrode (Pattantyus-Abraham *et al.*, 2010; Lin *et al.*, 2014). This therefore gives rise to a decreased fill factor and open circuit voltage, resulting in a diminished power conversion efficiency. For further improvement of Schottky junction solar cells, optimisation of the barrier height is very essential (Feng *et al.*, 2011; Foldyna, Yu and Roca i Cabarrocas, 2012). The injection efficiency of a Schottky junction solar cell made from a metal and an organic/inorganic semiconductor may be calculated using equation [2.9];

$$\Phi_{inj} = \frac{N_{ox}}{N_p^A} = \frac{N_{electrons}}{N_p^A} \qquad [2.9]$$

…where N_{ox} is the number of oxidized organic molecules, $N_{electrons}$ is the number of electrons, N_p^A is the number of absorbed photons and Φ_{inj} is the electron injection efficiency (Kampen, Park and Zahn, 2002; Willis *et al.*, 2011). N_{ox} and $N_{electrons}$

which can be used for calculation of the electron injection efficiency of solar cells can be evaluated by experimental techniques such as ambient absorption spectroscopy (Lee *et al.*, 2012; Roy, Das and Sarkar, 2016).

2.3.2.2 Evaluating electron injection through fluorescence measurements

Organic semiconductors or semiconductor nanoparticles undergo fluorescence measurements to evaluate the electronic transitions that occur within the molecules (Lunt, Benziger and Forrest, 2010; Mishra, Kaur and Ganguli, 2019). A study by Edwards *et. al.* (2000) illustrates that luminescence measurements such as electroluminescence and photoluminescence provide useful information on crystal defects in solar cells (Edwards, Galloway and Durose, 2000). The luminescence of semiconductor materials may be used to detect the number of electrons that undergo injection since those electrons do not fall back to ground state. This might imply that the less fluorescent a material is, the more electrons are injected into the acceptor material. Literature reports show that the electron injection may be calculated from luminescence using equation [2.10];

$$\Phi_{\mathrm{inj}} = 1 - \frac{\mathrm{N}_{\mathrm{non-inject}}}{\mathrm{N}_{\mathrm{P}}^{\mathrm{A}}} = 1 - \frac{\mathrm{I}_{\mathrm{F}}^{\mathrm{DSC}}}{\mathrm{I}_{\mathrm{F}}^{\mathrm{Inert}}} \qquad [2.10]$$

…where, $\mathrm{I}_{\mathrm{F}}^{\mathrm{Inert}}$ is the luminescence intensity of the semiconductor and $\mathrm{I}_{\mathrm{F}}^{\mathrm{DSC}}$ is the luminescence intensity of the metal electrode (Katoh, 2012). The experimental difficulties associated with the quantification of the luminescence of organic semiconductors are experienced since these semiconductors release poor luminescence when the electron injection efficiency is high. It may be argued that physically adsorbed (rather than chemically adsorbed) semiconductors give a very

high luminescent signal, hence, contribute very little to electron injection (Cherepy *et al.*, 1997; Kumar *et al.*, 2016). Time-resolved luminescent measurements are very useful for obtaining the luminescent properties of the semiconductor materials (Collier and McShane, 2013).

2.3.3 Factors limiting electron injection

2.3.3.1 Effect of an electrolyte on electron injection efficiency

A study by Wadhwa *et al.* demonstrates that the use of an electrolyte in Schottky junction solar cells improves the power conversion efficiency of these solar cells (Wadhwa *et al.*, 2011). As can be seen in the figure below, instead of using a continuous carbon nanotube film to form the junction, the film is etched in a grid pattern to cover only a fraction of the n-Si surface.

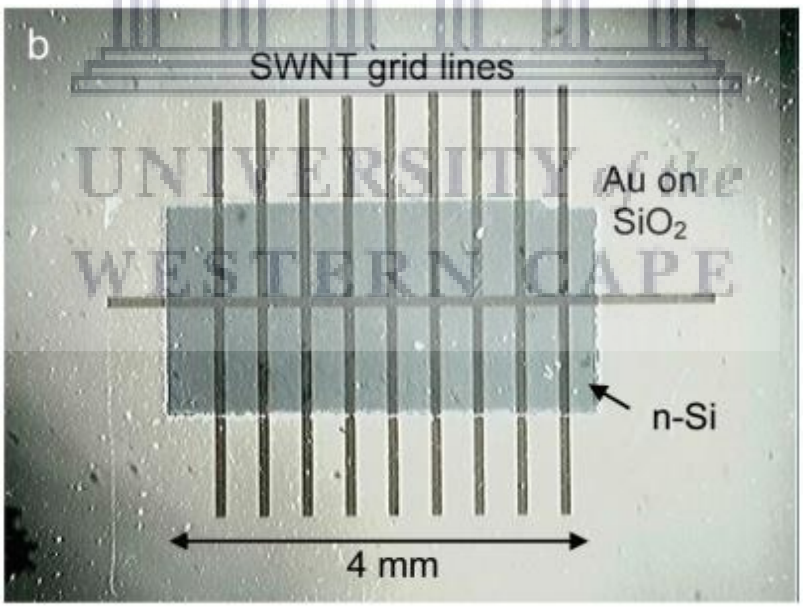

Figure 2.5: Schematic of the electrolytic Schottky junction solar cells (Wadhwa *et al.*, 2011).

Figure 2.5 illustrates that a liquid electrolyte creates a depletion (inversion) layer in an n-type silicon wafer, same as a photo-electrochemical cell. However, there is no

regenerative redox couple present to transport charge between the silicon and a counter electrode. Instead holes trapped in the electrolyte-induced inversion layer diffuse along the layer until they come to widely spaced grid lines; where they are extracted. Although the former findings by Wadhwa *et al.* (2011) seem to be ground-breaking, other studies reveal that since electrolytes also contain charged materials, the electrons and holes produced in the solar cell tend to react with the electrolyte. This therefore reduces the efficiency of the Schottky junction solar cells (Fabregat-Santiago *et al.*, 2005; Garca-Santamara *et al.*, 2009; Xie *et al.*, 2010).

2.3.3.2 Influence of applied electrical bias

A study by Aydogan and Turut reported on the influence of applied electrical bias on the performance of Au/Carmine/p-Si/Al Schottky junction solar cell (Aydoĝan and Türüt, 2011). These authors claim to have found that the electrical characteristics of the Au/Carmine/p-Si/Al device are very sensitive to 12 MeV energy electrons irradiation and to white light illumination. This is because under electrical bias of 12 MeV, higher values of ideality factors (<1) are obtained as an indication of electron/hole recombination. Moreover, the solar cell undergoes degradation in the Au/Carmine/p-Si/Al diode due to the introduction of radiation-induced interfacial defects (between Au and n-Si), and lattice defects via displacement damage (Ö. Güllü *et al.*, 2010; Aydoğan, Şerifoğlu and Türüt, 2011).

2.3.3.3 Energy dependence on injection kinetics

There are three specifically dominant colloidal quantum dot (CQD) solar cell architectures; Schottky-diode, heterojunction and CQD sensitized solar cells. Compared with the other two architectures, the efficiency of Schottky-diode based CQD solar cells is highly influenced by the energy barrier height for hole injection into the electron-extraction electrode (Hu *et al.*, 2016). Improving the efficiency by manipulating the open circuit voltage involves complex mechanisms such as thermodynamic losses, charge behaviour, interfacial energetics, electronic properties and charge transfer (CT) states (Lee *et al.*, 2015).

2.4 General review of Schottky junction solar cells using semiconducting quantum dots in the active layer

2.4.1 Graphene quantum dots as electron donors for Schottky junction solar cells

Graphene possesses extraordinary properties which include high optical transparency, large sheet conductivity, outstanding mechanical properties, and excellent physical/chemical stability. For this reason, there is a large and growing interest to explore its potential applications in energy-related fields, including solar cells, lithium ion batteries, and supercapacitors. Studies by Gao *et al.* (2014) show that a graphene film can form Schottky junctions with n-type Si. Separation of photoinduced electron−hole pairs at the graphene/Si interface can be facilitated by the existence of built-in electric field. However, the fabrication of large-scale graphene films facilitates high-temperature chemical vapor deposition (CVD) growth and complicated transfer processes. This inevitably increases the cost of the

devices made from graphene. Recent studies have demonstrated marvellous properties of graphene quantum dots (GQDs) arising from the strong quantum confinement and edge effects. GQDs show continuous absorption in the UV−visible region of the solar spectrum because of the overlap of electronic absorption bands caused by closely spaced electronic energy levels and vibrionic coupling. The extraordinarily long lifetimes of hot carriers in GQDs could potentially allow for efficient hot-carrier harvesting or multi-exciton generation that could exceed the Shockley-Queisser limit in solar energy utilisation. With their large abundance, nontoxicity, high mobilities, and tunable band gaps, GQDs could hold great promise for efficient photovoltaic devices as light absorbers. Gao *et al.* (2014) studied the Schottky junction formed at the interface between GQD and crystalline silicon. The large junction gap between GQDs and n-Si was shown to allow for the efficient separation of photogenerated electron−hole pairs at the junction interface, while the low GQDs' LUMO level with respect to the silicon's conduction band ensures a low interface recombination. As a result, both the open-circuit voltage and short-circuit current of the c-Si/GQDs heterojunction solar cells have been substantially improved as compared to those of the device counterparts without GQDs. The results obtained in the study showed an optimal efficiency of 6.63% when GQD are used in device fabrication as opposed to when they are not used. **Figure 2.6** shows J-V curves obtained from the study conducted by Gao *at el.* (2014) (Gao *et al.*, 2014).

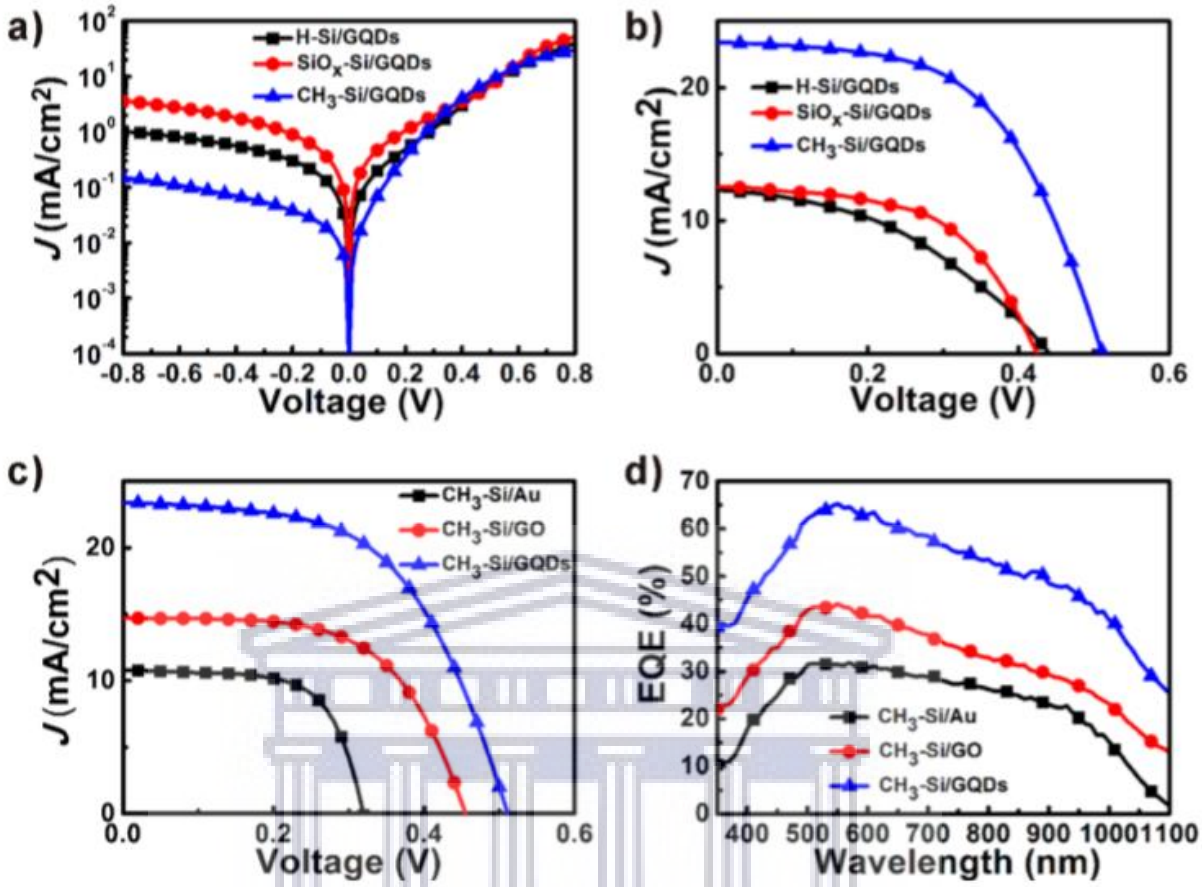

Figure 2.6: J-V curves of c-Si/GQDs heterojunctions with different surface terminations of H-, SiO_x-, and CH_3- (a) in the dark and (b) under AM 1.5 G P_i, respectively. (c) J-V curves and (d) external quantum efficiency (EQE) spectra of CH_3-Si/Au, CH_3−Si/ GO, and CH_3-Si/GQDs devices (Gao *et al.*, 2014).

2.4.2 Silicon quantum dots as electron donors in Schottky junction photodetectors

Graphene readily forms Schottky junctions with semiconductors, and as a result, graphene-based optoelectronic devices employ Schottky junctions. For example, Schottky-junction photodetectors have been recently developed by using graphene and bulk silicon (Si). The n-type Si is usually used for graphene/Si Schottky-junction photodetectors. The enhanced performance of graphene/Si Schottky junction photodetectors is a result of an increased built-in potential from the lowered Fermi-level of graphene. Up to now, chemical doping has been the most popular for the lowering of the Fermi-level of graphene (i.e., p-type doping). However, it has been found that chemical doping does no produce stable graphene structures and it also damages the graphene structure. In addition, chemical doping processes may decrease the optical absorption of devices. It has been recently shown that charge transfer may occur between graphene and semiconductor quantum dots (QDs). This means the Fermi-level of graphene may be tuned by coupling graphene with semiconductor QDs. As one type of the most important semiconductor QDs, Si quantum dots have been gaining popularity due to the abundance and non-toxicity of silicon. In a study by Yu *et al.*, graphene was coupled with Silicon Quantum Dots to create Bulk-Silicon-Based Schottky-Junction Photodetectors and the results are presented in **Figure 2.7**.

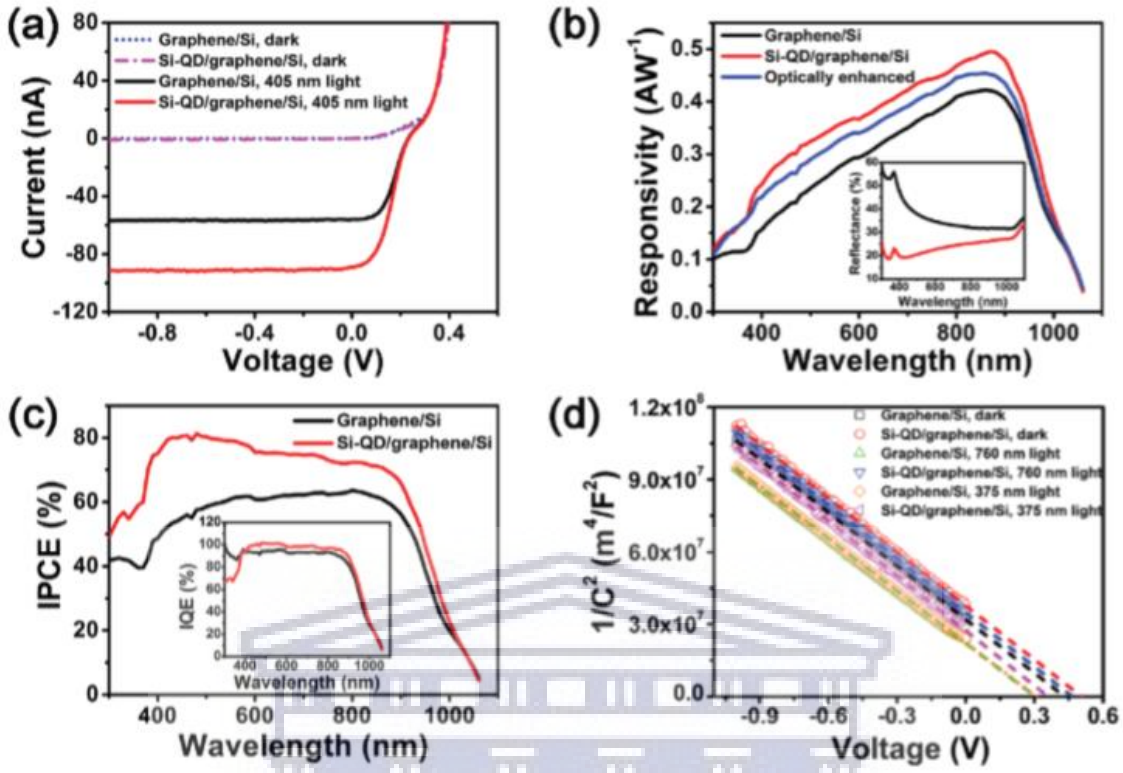

Figure 2.7: a) I-V curves of the graphene/Si and Si-QD/graphene/Si photodetectors either in the dark or under the illumination of 405 nm light. b) Responsivity of the graphene/Si and Si-QD/graphene/Si photodetectors under the bias of -1 V with the result of only considering the optical enhancement of Si QDs. The optical reflectance of the graphene/Si and Si-QD/graphene/Si photodetectors are shown on the inset. c) IPCE along with the IQE (inset) of the graphene/Si and Si-QD/graphene/Si photodetectors. d) Shows the plot of the inverse square capacitance (1/ C2) against applied bias (V) for the graphene/Si and Si-QD/graphene/Si photodetectors obtained under different illuminations at 300 K and 5 kHz. The linear fitting is carried out by assuming the Schottky-Mott model (Yu et al., 2016).

In their study, they found that V_{bi} is ≈0.43 (0.51) eV when graphene is not (is) coupled with Si QDs. By using V_{bi} and the work function (W_{Si}) of bulk Si (4.30 eV), they found that the work function (W_{Gr}) is ≈4.73 (4.81) eV for graphene without (with)

the coupling of Si QDs. Their results were close to those directly measured with a Kelvin probe. The work-function of graphene, approximately 4.73 eV, was consistent with the nearly intrinsic value of work-function for graphene originally grown on copper foils by CVD, indicating that bulk Si hardly affects graphene work-function. Experimental studies on the original state of graphene shows that it is a p-type doped material. This inspires the formation of the graphene/Si Schottky junction. When Si quantum dots are coupled with graphene, the graphene work-function increases from approximately 4.73 to 4.81 eV. This means that there is electron transfer from graphene to Si QDs, lowering the Fermi-level of graphene. Therefore, V_{bi} increases when graphene is coupled with Si QDs. A large V_{bi} means a wide depletion region, and this results in more effective separation of photon-generated carriers. Thus, we state that the increase of V_{bi} induced by the coupling of graphene with Si QDs contributes to the improvement of the photo-response (Yu *et al.*, 2016).

2.4.3 Colloidal PbS quantum dots as electron donors for Schottky junction solar cells

Colloidal quantum dot solar cells offer great potentials in solar energy conversion because of their compatibility with solution processing, enabling rapid large area and low-cost fabrication processes. Compared to organic and polymer solar cells, solar cells based on PbS, PbSe and PbSSe CQDs access a greater portion of the solar spectrum in the infrared range using low band gap PbS and PbSe nanoparticles. Tang *et al.* (2010) studied the stability of Schottky junction solar cells based on PbS colloidal quantum dots. In their study, they used two hypothesis that might result in possible degradation of the cells.

- GQDs films may lose passivation and/or develop midcap recombination centres. This means that labile ligands such as butylamine and ethane-diol make the films exposable to attack by oxygen and moisture.
- The shallow-work-function metals at the interface of the films are known to be oxidized rapidly, such that they may also react with ligands in the film.

Therefore, different metal contacts were used to evaluate the stability of the cells (Ag, Al and Au), irrespective of the air-sensitivity of PbS quantum dots. In the study by Tang *et al.* (2010), it was found that the Ag contacts improved the air-stability for 4 days in ambient storage. This was attributed to the air stability of the Ag contacts compared to the other metals. However, unfortunately there was a trade-off between the air-stability and efficiency of the solar cells, as the use of Ag contacts resulted in lower V_{oc} (0.24V) compared to Al (V_{oc} = 0.42V). Therefore, a thin layer of LiF was introduced between PbS QD and Al contact in the presence of Ag contacts to form: ITO/PbS/LiF/Al/Ag. Introduction of the LiF showed improvement in air-stability and

photovoltaic efficiency. The outcome of this study shows that in PbS devices, the degradation at Al contact from interfacial reaction and oxidation is the main cause of degradation in Schottky junction solar cells (Tang *et al.*, 2010).

2.5 Current outstanding limitations found in literature

This review has demonstrated the use of Schottky junction to improve the performance of solar cells. However, the use of graphene quantum dots as electron donors for Schottky junction solar cells have not been extensively explored. Therefore, in this study, graphene quantum dots of different band gaps to match the visible region of the solar spectrum are used for optimal efficiency. These GQDs are used with three different metals; Al, Au and graphene to create the Schottky junction in the active layer of the solar cell.

References

Adaine, A., Ould Saad Hamady, S. and Fressengeas, N. (2016) 'Simulation study of a new InGaN p-layer free Schottky based solar cell', *Superlattices and Microstructures*, 96, pp. 121–133.

Almadori, Y. *et al.* (2019) 'Fermi-level shift in carbon nanotubes by dye confinement', *Carbon*, 149, pp. 772–780.

Alnuaimi, A. *et al.* (2018) 'Interface engineering of graphene-silicon Schottky junction solar cells with an Al2O3 interfacial layer grown by atomic layer deposition', *RSC Advances*, 8, pp. 10593–10597.

Arabpour Roghabadi, F. *et al.* (2018) 'Bulk heterojunction polymer solar cell and perovskite solar cell: Concepts, materials, current status, and opto-electronic properties', *Solar Energy*, 173, pp. 407–424.

Anjana, P. M., Bindhu, M. R. and Rakhi, R. B. (2019) 'Green synthesized gold nanoparticle dispersed porous carbon composites for electrochemical energy storage', *Materials Science for Energy Technologies*, 2, pp. 389–395.

Ansari, Z. A. *et al.* (2019) 'Photovoltaic solar cells based on graphene/gallium arsenide Schottky junction', *Optik*, 182, pp. 500–506.

Auf der Maur, M. and Di Carlo, A. (2019) 'Analytic approximations for solar cell open circuit voltage, short circuit current and fill factor', *Solar Energy*, 187, pp. 358–367.

Azzouzi, M., Kirchartz, T. and Nelson, J. (2019) 'Factors Controlling Open-Circuit Voltage Losses in Organic Solar Cells', *Trends in Chemistry*, 1, pp. 49–62.

Ahmad, U. *et al.* (2018) 'Synthesis and characterization of InN quantum dots for optoelectronic applications', *Optik*, 173, pp. 97–100.

Aydoğan, Ş., Şerifoğlu, K. and Türüt, A. (2011) 'The effect of electron irradiation on

the electrical characteristics of the Aniline Blue/n-Si/Al device', *Solid State Sciences*, 13, pp. 1369–1374.

Aydoğan, Ş. and Türüt, A. (2011) 'Influence of 12MeV electron irradiation on the electrical and photovoltaic properties of Schottky type solar cell based on Carmine', *Radiation Physics and Chemistry*, 80, pp. 869–875.

Barala, S. S., Bhati, V. S. and Kumar, M. (2017) 'High energy photon induced Fermi-level shift of Ba0.5Sr0.5TiO3 thin films', *Thin Solid Films*, 639, pp. 107–112.

Badawy, W. A. (2015) 'A review on solar cells from Si-single crystals to porous materials and Quantum dots', *Journal of Advanced Research*, 6(2), pp. 123–132.

Baxter, J. B. and Aydil, E. S. (2005) 'Nanowire-based dye-sensitized solar cells', *Applied Physics Letters*, 86, pp. 1–3.

Bayhan, H. and Kavasoglu, A. S. (2007) 'Exact analytical solution of the diode ideality factor of a pn junction device using Lambert W-function model', *Turkish Journal of Physics*, 31, pp. 7–10.

Breitenstein, O., Frühauf, F. and Turek, M. (2016) 'Improved empirical method for calculating short circuit current density images of silicon solar cells from saturation current density images and vice versa', *Solar Energy Materials and Solar Cells*, 154, pp. 99–103.

Cherepy, N. J. *et al.* (1997) 'Ultrafast electron injection: Implications for a photoelectrochemical cell utilizing an anthocyanin dye-sensitized TiO2 nanocrystalline electrode', *Journal of Physical Chemistry B*, 101, pp. 9342–9351.

Choi, H. *et al.* (2013) 'Increased open-circuit voltage in a Schottky device using PbS quantum dots with extreme confinement', *Applied Physics Letters*, 102, pp. 3–7.

Choi, H., Chen, W. T. and Kamat, P. V (2012) 'Know Thy Nano Neighbor. Plasmonic versusElectron Charging Effects of Metal Nanoparticles in Dye-Sensitized Solar

Cells', *ACS nano*, 6, pp. 4418–4427.

Collier, B. B. and McShane, M. J. (2013) 'Time-resolved measurements of luminescence', *Journal of Luminescence*, 144, pp. 180–190.

Darvishzadeh, P. *et al.* (2016) 'Modeling the degradation/recovery of open-circuit voltage, Voc(t), in perovskite and thin film solar cells', *Materials & Design*, 114, pp. 339–344.

Darvishzadeh, P. *et al.* (2017) 'Modeling the degradation/recovery of short-circuit current density in perovskite and thin film photovoltaics', *Organic Electronics: physics, materials, applications*, 43, pp. 247–252.

Datt, R. *et al.* (2019) 'Dual-functional cathode buffer layer for power conversion efficiency enhancement of bulk-heterojunction solar cells', *Synthetic Metals*, 255, p. 116112.

Edwards, P., Galloway, S. and Durose, K. (2000) 'EBIC and luminescence mapping of CdTe/CdS solar cells', *Thin Solid Films*, pp. 284–291.

Fatima Rasheed, J. and Suresh Babu, V. (2019) 'Performance evaluation of composition graded layer of aSi1-xGex: H in n+aSi:H/i-aSi:H/p+aSi1-xGex:H graded band gap single junction solar cells', *Materials Today: Proceedings*, xxx, p. xxx.

Feng, T. *et al.* (2011) 'Graphene based Schottky junction solar cells on patterned silicon-pillar-array substrate', *Applied Physics Letters*, 99, p. 233505.

Gao, P. *et al.* (2014) 'Crystalline Si / Graphene Quantum Dots Heterojunction Solar Cells', *Journal of Physical Chemistry*, 118, pp. 5164–5171.

Garca-Santamara, F. *et al.* (2009) 'Suppressed auger recombination in "Giant" nanocrystals boosts optical gain performance', *Nano Letters*, 9, pp. 3482–3488.

Green, M. A. and Godfrey, R. B. (1976) 'MIS solar cell - General theory and new experimental results for silicon', *Applied Physics Letters*, 29, pp. 610–612.

Gupta, A., Rajawat, S. and Malik, M. M. (2019) 'Investigations on ITO/Ag-WO3/Ag heterojunction Schottky solar cell: Fabrication and characterization through I–V and C–V', *Optik*, 194, p. 163104.

Güllü, Ö. *et al.* (2010) 'Electrical characterization of the Al/new fuchsin/n-Si organic-modified device', *Physica E: Low-Dimensional Systems and Nanostructures*, 42, pp. 1411–1416.

He, Y. *et al.* (2019) 'Ohmic contacts simultaneously formed on n-type and p-type 4H-SiC at low temperature', *Journal of Alloys and Compounds*, 805, pp. 999–1003.

Huang, H. *et al.* (2019) 'Analytical model for accurate extraction of metal-semiconductor ohmic contact parameters using a novel electrode-pair layout scheme', *Physica E: Low-Dimensional Systems and Nanostructure*, 108, pp. 197–201.

Hu, L. *et al.* (2016) 'Imbalanced charge carrier mobility and Schottky junction induced anomalous current-voltage characteristics of excitonic PbS colloidal quantum dot solar cells', *Solar Energy Materials and Solar Cells*, 155, pp. 155–165.

Jayenta Singh, T. *et al.* (2019) 'Flexible organic solar cells with graphene/PEDOT:PSS Schottky junction on PET substrates', *Optik*, 181, pp. 984–992.

Ju, S. *et al.* (2018) 'Graphene/silicon Schottky solar cells: Technical strategies for performance optimization', *Optics Communications*, 428, pp. 258–268.

Kampen, T. U., Park, S. and Zahn, D. R. T. (2002) 'Barrier height engineering of Ag/GaAs(100) Schottky contacts by a thin organic interlayer', *Applied Surface*

Science, 190, pp. 461–466.

Kanale, A. *et al.* (2019) 'Stability of 4H-SiC JBS Diodes under Repetitive Avalanche Stress', *IEEE International Reliability Physics Symposium Proceedings*. IEEE, 2019-March, pp. 1–6.

Konovalov, I., Strikha, V. and Breitenstein, O. (1998) 'Activation Energy of Local Currents in Solar Cells Measured by Thermal Methods', *Progress in Photovoltaics: Research and Applications*, 6, pp. 151–161.

Kumar, P. *et al.* (2016) 'Femtosecond insights into direct electron injection in dye anchored ZnO QDs following charge transfer excitation', *Phys. Chem. Chem. Phys.*, 18, pp. 20672–20681.

Kiermasch, D. *et al.* (2019) 'Effects of Masking on Open-Circuit Voltage and Fill Factor in Solar Cells', *Joule*, pp. 16–26.

Li, Y. *et al.* (2019) 'Enhanced power conversion efficiency and preferential orientation of the MAPbI3 perovskite solar cells by introduction of urea as additive', *Organic Electronics*, 73, pp. 130–136.

Liu, Z. X. *et al.* (2019) 'Achieving efficient organic solar cells and broadband photodetectors via simple compositional tuning of ternary blends', *Nano Energy*, 63, p. 103807.

Lancellotti, L. *et al.* (2016) 'Combined effect of double antireflection coating and reversible molecular doping on performance of few-layer graphene/n-silicon Schottky barrier solar cells', *Solar Energy*, 127, pp. 198–205.

Lee, C. C. *et al.* (2015) 'The effect of charge transfer state on the open-circuit voltage of small-molecular organic photovoltaic devices: A comparison between the planar and bulk heterojunctions using electroluminescence characterization', *Organic*

Electronics: physics, materials, applications, 16, pp. 1–8.

Lee, M. *et al.* (2012) 'Efficient hybrid solar cells based on meso-superstructured organometal halide perovskites', *Science*, 338, pp. 643–647.

Li, X. *et al.* (2014) '*High performance solar cells based on graphene / GaAs heterostructures*', *arXiv:1409.3500, pp.1-23*.

Lin, B.C. *et al.* (2014) 'Hole injection and electron overflow improvement in InGaN/GaN light-emitting diodes by a tapered AlGaN electron blocking layer.', *Optics express*, 22, pp. 463–9.

Liu, H. *et al.* (2016) 'Cost-effective hollow honeycomb textured back reflector for flexible thin film solar cells', *Solar Energy Materials and Solar Cells*, 155, pp. 128–133.

Liu, Y., Stradins, P. and Wei, S.-H. (2016) 'Van der Waals metal-semiconductor junction: Weak Fermi-level pinning enables effective tuning of Schottky barrier.', *Science advances*, 2, pp. 1600069.

Lunt, R. R., Benziger, J. B. and Forrest, S. R. (2010) 'Relationship between crystalline order and exciton diffusion length in molecular organic semiconductors', *Advanced Materials*, 22, pp. 1233–1236.

Lv, Y. *et al.* (2018) 'Enhanced efficiency and stability of fully air-processed TiO2 nanorods array based perovskite solar cell using commercial available CuSCN and carbon', *Solar Energy*, 173, pp. 7–16.

Manjceevan, A. and Bandara, J. (2018) 'Systematic stacking of PbS/CdS/CdSe multi-layered quantum dots for the enhancement of solar cell efficiency by harvesting wide solar spectrum', *Electrochimica Acta*, 271, pp. 567–575.

Marnadu, R. *et al.* (2019) 'Ultra-high photoresponse with superiorly sensitive metal-insulator-semiconductor (MIS) structured diodes for UV photodetector application',

Applied Surface Science, 480, pp. 308–322.

Mishra, J., Kaur, N. and Ganguli, A. K. (2019) 'Selective and sensitive fluorescence recognition of Pb(II) in aqueous medium by organic nanoparticles of a urea linker based tetrapodal receptor: Effect of linker molecules in a sensor on chemosensing', *Inorganica Chimica Acta*, 487, pp. 214–220.

Missoum, I. *et al.* (2016) 'Microelectronic properties of organic Schottky diodes based on MgPc for solar cell applications', *Synthetic Metals*, 214, pp. 76–81.

Namvar, A. *et al.* (2016) 'Thermal residual stresses in silicon thin film solar cells under operational cyclic thermal loading: A finite element analysis', *Solar Energy*, 135, pp. 366–373.

Nematpour, A. and Nikoufard, M. (2018) 'Plasmonic thin film InP/graphene-based Schottky-junction solar cell using nanorods', *Journal of Advanced Research*, 10, pp. 15–20.

Ono, L. K., Qi, Y. and Liu, S. (Frank) (2018) 'Progress toward Stable Lead Halide Perovskite Solar Cells', *Joule*, 2, pp. 1961–1990.

Pylypova, O. V. *et al.* (2019) 'Electrical and optical properties of nanowires based solar cell withradial p-n junction', *Opto-electronics Review*, 27, pp. 143–148.

Quan, C. *et al.* (2018) 'Computational analysis of a high-efficiency tunnel oxide passivated contact (TOPCon) solar cell with a low-work-function electron-selective-collection layer', *Solar Energy*, 170, pp. 780–787.

Qiu, J. *et al.* (2018) 'Enhanced efficiency of graphene-silicon Schottky junction solar cell through inverted pyramid arrays texturation', *Journal of Materials Science and Technology*, 34, pp. 2197–2204.

Roy, S., Das, S. and Sarkar, C. K. (2016) 'Investigation of nanostructured Pd–Ag/n-

ZnO thin film based Schottky junction for methane sensing', *International Nano Letters*, 6, pp. 199–210.

Scagliotti, M. *et al.* (2019) 'Femtosecond light pulse response of photodetectors based on Graphene/n-Si heterojunctions', *Carbon*, 152, pp. 643–651.

Shi, X. *et al.* (2018) 'Terthieno[3,2-b]Thiophene (6T) Based Low Bandgap Fused-Ring Electron Acceptor for Highly Efficient Solar Cells with a High Short-Circuit Current Density and Low Open-Circuit Voltage Loss', *Advanced Energy Materials*, 8, pp. 2–9.

Singh, A. N. *et al.* (2018) 'Fermi-level equilibration of Ag and Au plasmonic metal nanoparticles supported on graphene oxide', *Physical Chemistry Chemical Physics*, 20, pp. 26719–26733.

Song, L., Yu, X. and Yang, D. (2019) 'A review on graphene-silicon Schottky junction interface', *Journal of Alloys and Compounds*, 806, pp. 63–70.

Shin, D. H. *et al.* (2019) 'Graphene-nanomesh transparent conductive electrode/porous-Si Schottky-junction solar cells', *Journal of Alloys and Compounds*, 803, pp. 958–963.

Singh, P. and Ravindra, N. M. (2012) 'Temperature dependence of solar cell performance-an analysis', *Solar Energy Materials and Solar Cells*, 101, pp. 36–45.

Sinha, D. and Lee, J. U. (2014) 'Ideal Graphene / Silicon Schottky Junction Diodes', *Nano Letters*, pp. 4660–4664.

Sudhakar, Y. N. *et al.* (2018) 'Biopolymer Electrolytes for Solar Cells and Electrochemical Cells', *Biopolymer Electrolytes*, pp. 117–149.

Sun, Y., Sun, M. and Xie, D. (2018) 'Graphene Electronic Devices', in *Graphene*, pp. 103–155.

Tian, P. *et al.* (2019) 'Ti3C2 nanosheets modified Zr-MOFs with Schottky junction for boosting photocatalytic HER performance', *Solar Energy*, 188, pp. 750–759.

Tang, B. J. *et al.* (2010) 'Schottky Quantum Dot Solar Cells Stable in Air under Solar Illumination', *Advanced Materials*, 4, pp. 1398–1402.

Venkatesh, R. *et al.* (2019) 'Enhancement of open circuit voltage of CdTe solar cell', *Materials Today: Proceedings, xxxx, 10-12.*

Voroshazi, E. *et al.* (2011) 'Long-term operational lifetime and degradation analysis of P3HT:PCBM photovoltaic cells', *Solar Energy Materials and Solar Cells*, 95, pp. 1303–1307.

Wadhwa, P. *et al.* (2011) 'Electrolyte-induced inversion layer Schottky junction solar cells', *Nano Letters*, 11, pp. 2419–2423.

Willis, S. M. *et al.* (2011) 'Modified Mott-Schottky analysis of nanocrystal solar cells', *arXiv.org, e-Print Arch., Condens. Matter*, pp. 1–6.

Xie, Q. *et al.* (2019) 'Random copolymerization realized high efficient polymer solar cells with a record fill factor near 80%', *Nano Energy*. Elsevier, 61, pp. 228–235.

Xu, H. *et al.* (2018) 'Narrow bandgap non-fullerene acceptor based on a thiophene-fused benzothiadiazole unit with a high short-circuit current density of over 20 mA cm-2', *Journal of Materials Chemistry A*, 6, pp. 6393–6401.

Yang, Y. *et al.* (2019) 'One-pot synthesis and characterization of ovalbumin-conjugated gold nanoparticles: A comparative study of adjuvanticity against the physical mixture of ovalbumin and gold nanoparticles', *International Journal of Pharmaceutics*, 571, p. 118704.

Yu, H. *et al.* (2018) 'Improving photovoltaic performance of inverted planar structure perovskite solar cells via introducing photogenerated dipoles in the electron transport layer', *Organic Electronics: physics, materials, applications*, 63, pp. 137–

142.

Yu, T. *et al.* (2016) 'Graphene Coupled with Silicon Quantum Dots for Photodetectors', *Advanced Materials*, 28, pp. 4912–4919.

Zhang, Y. *et al.* (2018) 'Synthesis of Co3O4 /Ag/TiO2 nanotubes arrays via photo-deposition of Ag and modification of Co3O4 (311) for enhancement of visible-light photoelectrochemical performance', *Applied Surface Science*, 427, pp. 1009–1018.

Zhang, X. *et al.* (2019) 'Three-terminal heterojunction bipolar transistor solar cells with non-ideal effects: Efficiency limit and parametric optimum selection', *Energy Conversion and Management*, 188, pp. 112–119.

Zhang, Y. *et al.* (2019) 'Optical H2S and SO2 sensor based on chemical conversion and partition differential optical absorption spectroscopy', *Spectrochimica Acta Part A: Molecular and Biomolecular Spectroscopy*, 210, pp. 120–125.

Zhao, T. J. *et al.* (2018) 'Electrostatically mediated selectivity of Pd nanocatalyst via rectifying contact with semiconductor: Replace ligands with light', *Applied Catalysis B: Environmental*, 238, pp. 404–409.

Zheng, Y. Z. *et al.* (2018) 'Plasmonic enhancement of light-harvesting efficiency in tandem dye-sensitized solar cells using multiplexed gold core/silica shell nanorods', *Journal of Power Sources*, 376, pp. 26–32.

Zhang, M. *et al.* (2018) 'Copper doping of MoOx thin films for CdTe solar cells', *Materials Science in Semiconductor Processing*, 86, pp. 49–57.

Zhao, B. *et al.* (2018) 'Performance analysis of enhanced radiative cooling of solar cells based on a commercial silicon photovoltaic module', *Solar Energy*, 176, pp. 248–255.

CHAPTER 3

Summary

South Africa is the sixth largest holder of coal in the world, with 31 billion tons of recoverable coal reserves equivalent to 11% of the world's total coal reserves. Coal is a perfect candidate to replace graphite as the raw material for production of graphene and its derivatives due to its carbon content (i.e., about 60 to 80 %). Nanometre-sized graphene quantum dots from coal are possible due to the fact the crystalline carbon in the coal structure is easier to oxidatively displace than when pure sp^2-carbon structures are used. Therefore, in this chapter, graphene quantum dots of different sizes to match the visible region of the solar spectrum are prepared by oxidising coal under different synthesis temperatures, as shown in Figure 3.1. The resulting structure and properties of the obtained materials is then evaluated and discussed in this chapter.

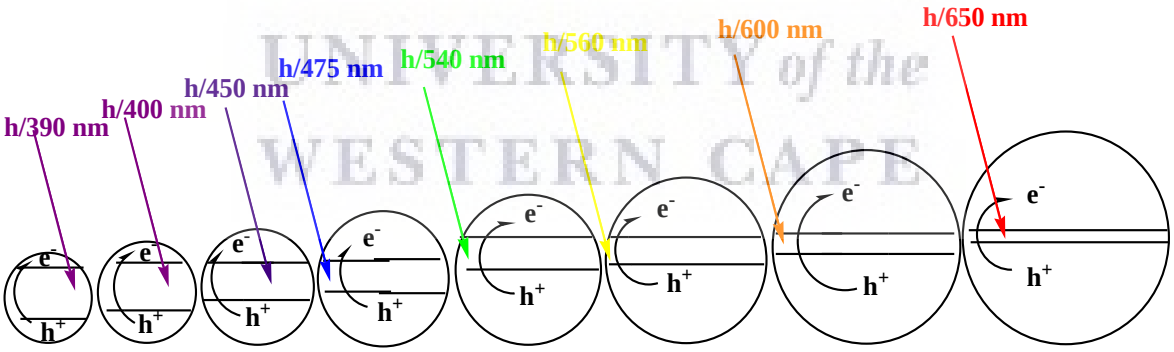

Figure 3.1: A diagram showing graphene quantum dot atoms of different sizes with their electrons being excited by different energies (E = hv = h/λ) from the visible region of the solar spectrum of matching band energies from quantum dots.

Preparation of graphene quantum dots with different band gaps to match the visible region of the solar spectrum, potential for application as donor materials for solar cells

Abstract

Graphene quantum dots (GQDs) have attracted researcher's attention due to their controllable photoluminescence performance, high stability and low cost. Since GQDs are carbon-based, the lack of heavy metals on the GQD structure renders them environmentally friendly and biocompatible materials. Therefore, the aim of the work conducted in this study was to prepare graphene quantum dots of different size regimes, i.e, different band gaps to match the visible region of the solar spectrum as potential donor materials for photovoltaic applications. The GQDs prepared in this study were harvested from coal through oxidation under reflux at different temperatures. Structural characterisation by solid state carbon 13 nuclear magnetic resonance (SS-^{13}C-NMR) characterisation proved the existence of sp^2-hybridised carbons from the benzene rings and carboxylic acid carbons in the GQDs structure. Fourier-transform infrared (FTIR) spectroscopy revealed characteristic fingerprint band energies corresponding to C=C, C=O, O-H and C-H functional groups from the benzene rings and oxidised carbon atoms in accordance to NMR results. This was supported by the π-π* and n-π* transitions due to the sp^2-hybridised and oxidized carbons in GQD benzene ring backbones observed on UV-Vis spectroscopy, respectively. The observed blue-shift on the photoluminescence spectra with respect to increasing synthesis temperature (i.e., decreasing particle size) evidenced the quantum confinement effect and edge effects, which confirmed the existence of quantum dot structures. HR-TEM showed a decrease in the particle

size with synthesis time and temperature, in agreement with the fluorescence results obtained. The electrochemical characterisation of the quantum dots shows fast electron kinetics with decreasing band gap energies of the nanomaterials, a property desirable for application in rainbow solar cells.

3.1 Introduction

Quantum dots (QDs) are the leading donor materials in photovoltaics due to their size-tuned optical response, efficient multiple carrier generation, and low cost (Mirnajafizadeh *et al.*, 2016; Nideep, Ramya and Kailasnath, 2019; Liu *et al.*, 2020). However, their toxicity and hazardous nature remain a serious concern for large-scale device applications (Wehrenberg, Wang and Guyot-Sionnest, 2002; Frasco and Chaniotakis, 2010; Sharma *et al.*, 2017; Reshma and Mohanan, 2019). Therefore, environmentally friendly nanomaterials with similar properties are needed. Graphene materials offer attractive electronic, optical, magnetic and thermal properties (Duan *et al.*, 2018; Omidvar, RashidianVaziri and Jaleh, 2018; Zhang *et al.*, 2018). Theoretical reports have also predicted graphene to be a good material for fabrication of flexible next generation solar-energy conversion and optoelectronic devices that are low-cost, highly efficient, thermally stable, environmentally friendly and light-weight (Dong *et al.*, 2014; Iqbal and Rehman, 2018; Mahmoudi, Wang and Hahn, 2018). However, devices fabricated using graphene have shown inferior properties due to the zero band gap nature of graphene (Sbrockey *et al.*, 2018). Graphene is a zero-band-gap material due to the convergence of the conduction band minimum and valence band maximum at the Dirac point. As a result, adding a band gap to graphene has become a need to

extend graphene's potential. As such; the synthesis of graphene quantum structures such as GQDs has become of interest lately, making the use of graphene more versatile. A band gap in graphene quantum dots exists due to quantum confinement and edge effects (Zhu *et al.*, 2015; He *et al.*, 2018; Pourmahmoud and Rezaei, 2019).

Graphene quantum dots are nanometre-sized fragments of graphene whose electrons are confined in all three spatial dimensions. They are typically derived from three dimensional carbon materials by top-down synthetic approaches (Santiago *et al.*, 2017; Far'ain Md Noor *et al.*, 2018; Kalluri *et al.*, 2018). Ye *at al.* discovered that graphene quantum dots can be harvested from coal. The fact that the unique coal structure has an advantage over sp^2-carbon allotropes for producing GQDs was also established. The crystalline carbon within the coal structure is easier to oxidatively displace than when pure sp^2-carbon structures are used during synthesis (Ye *et al.*, 2013). GQDs normally exist in few-layer structures, with lateral dimensions up to 40 nm. Besides, GQDs properties are like that of graphene and they also show excellent photoluminescence (PL) performances including high photo-stability, tenable PL property, electrical conductivity and excellent thermal. This presents GQDs as a promising new platform materials in biological labelling and imaging, photochemical catalysis, photovoltaic devices and sensors (Sk *et al.*, 2014; Kelarakis, 2015; Pourmahmoud and Rezaei, 2019). Therefore, in this study, GQDs structures of different band gaps are harvested from coal by heating at different temperatures under reflux, using a modified method reported by Ruquan et al. (2013).

3.2 Methodology

3.2.1 Materials

Anthracite coal was purchased from Creatorlink Marketing cc., T/A Glamour fuels (Cape Town, SA) and ground to fine powder prior use. The oxidants (i.e., 98% nitric acid and 95% sulphuric acid) were all purchased from SIGMA-ALDRICH and used as received.

3.2.2 Synthetic method for the preparation of graphene quantum dots

The preparation of GQDs from different coal precursors (i.e, anthracite and bituminous coal) followed an adaptation method reported by Ruquan *et al* (2013) with a few modifications. In a typical reaction, 150 mg coal was oxidised in sulphuric acid and nitric acid. The resulting solutions were sonicated for 2 h and subsequently reduced by heating at a temperature of (60, 120, 180, 250) °C for 24 h. The resulting solutions were then filtered through a 0.25 µm microfiltration membrane, purified using a dialysis bag (1000 kDa) and preconcentrated on a freeze-dryer. Labelling of the samples is as follows; (ab) the prefix represents the coal starting material (i.e., anthracite or bituminous coal) and the suffix represents the synthesis temperature used (Ye *et al.*, 2013).

3.2.3 Characterisation techniques

Graphene quantum dot structural analysis was carried out by solid state direct ^{13}C NMR (Bruker, UK) with a 500 Avance III HD NMR at a frequency of 100.0 MHz. The spectrometer instrument is equipped with a zirconium rotor of 4 mm of external diameter. The ^{13}C spectrum was evaluated at a spin rate of 4 kHz, and 5400 scans were collected. The measurement was carried out at ambient temperature. Fourier Transform Infrared (FTIR) spectroscopy was used to confirm the synthesis of graphene quantum dots in the range of 4000 to 400 cm^{-1} through appearance of functional groups. These experiments were conducted on a Perkin Elmer FTIR model 100 spectro-photometer. Transmission Electron Microscopy (TEM JEOL, JEM-2010, Japan) were obtained at an accelerating voltage of 200 kV and used to examine the particle size and distribution of the prepared GQDs. The TEM specimens were prepared by placing a few drops of GQDs (dispersed in ethanol) solutions on a copper grid. The UV-vis absorption data and PL emission data was obtained by thermally evaporating a thin layer of the GQDs (30 µL) onto a clean ITO glass substrate. The absorption spectra were acquired at room temperature using UV-vis spectrometer Nicolet evolution 100 (ThermoFisher, America, Waltham, Massachusetts) and emission spectra was obtained using IGA-521 X 1–50–1700–1LS, HORIBA JOBIN YVON photoluminescence spectroscopy (PL) (Horiba, France). Electrochemical experiments were conducted using different scan rates at normal room temperature under nitrogen. The setup is a computer controlled consisting of a potentiostat CH (PalmSens, Netherlands, Houten). A solution of 0.1 M of tetrabutylammonium hexafluorophosphate was used as the electrolyte. Glassy carbon electrode was used as the working electrode, (silver/silver-chloride) Ag/AgCl

couple and platinum wire as the reference electrode and auxiliary electrode, respectively (PalmSens, Netherlands, Houten).

3.3 Results and discussion

3.3.1 Structural characterisation

3.3.1.1 Nuclear magnetic resonance spectroscopy (NMR)

^{13}C-NMR is an important tool for chemical structure elucidation in organic chemistry and was employed to evaluate the structures of the prepared GQDs. The ^{13}C-NMR spectrum of the GQDs presented in **Figure 3.2** offers proof for the formation of a sp^2 graphitic carbon network in the GQDs.

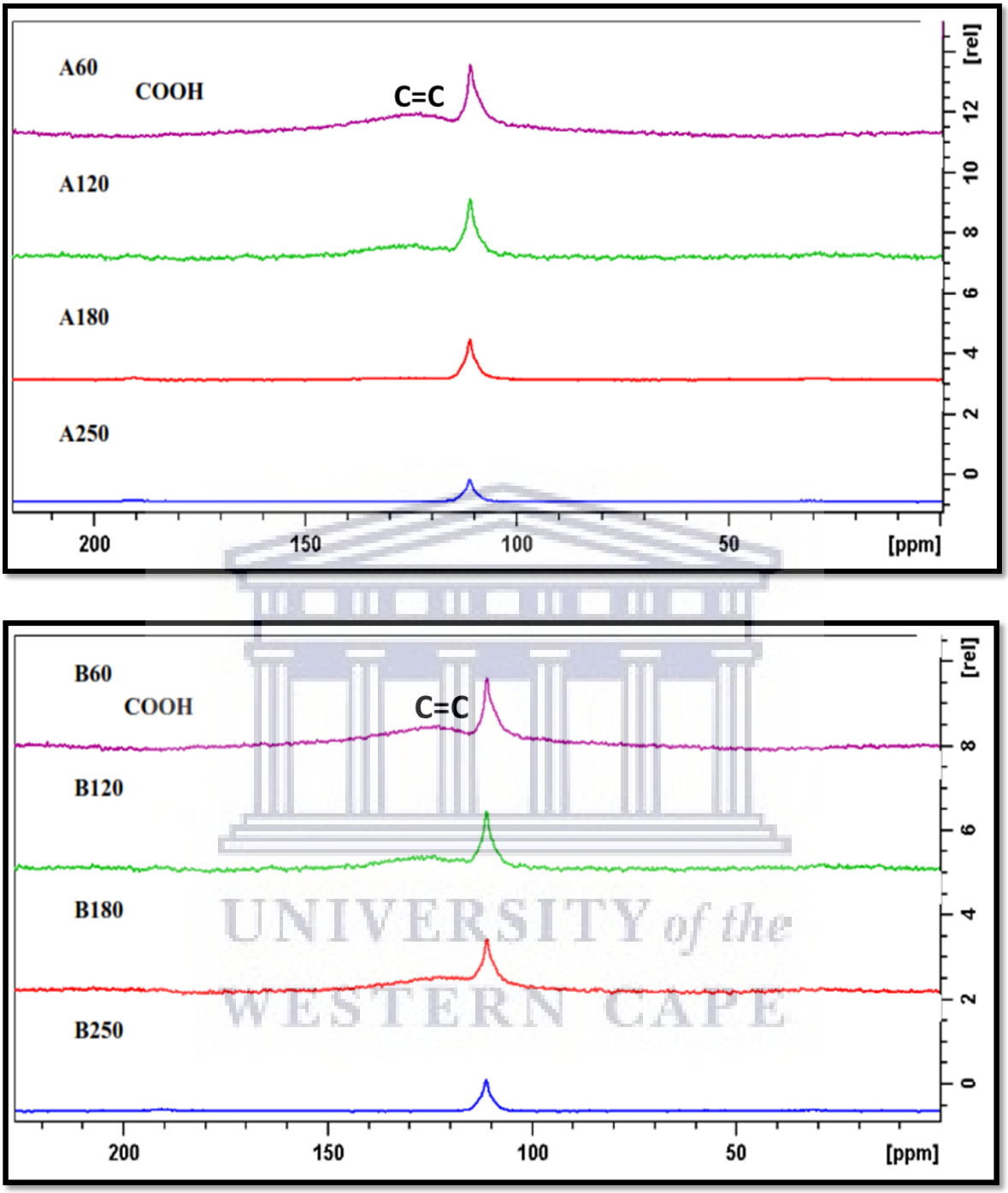

Figure 3.2: Solid-state ^{13}C-NMR spectra of the synthesised A and B-graphene quantum dots.

As shown in **Figure 3.2**, the peaks from 20 ppm to 40 ppm suggest that the sp^3 carbons are maintained while the peaks from 100 ppm to 180 ppm are attributed to the sp^2 carbons (Fürst, Pretsch and Robien, 1990). The prominent peaks between

120 ppm to 130 ppm are possibly due to sp^2 carbons derived from (polycyclic) aromatic carbons, those at 138 ppm correspond to C=C carbons and the peaks between 160 and 180 ppm are ascribed to the carboxylic carbons (Latil *et al.*, 2001; Hayashi *et al.*, 2003). The increase in the intensities of the peaks on the spectra signify the increase in carbon atoms in the structures of the prepared graphene quantum dots. Nevertheless, it is apparent from just these spectra that as the GQD size increases, the ^{13}C spectra indicate that a much wider variety of carbonyl environments is generated, including ketones as well as carboxyl functional groups.

3.3.1.2 Fourier Transform Infrared Spectroscopy

The structure of the prepared GQD materials was further confirmed by FTIR spectroscopy. As can be seen in the below spectra, the -OH, C=O, C=C, C-H, C-O fingerprint functional groups of graphene quantum dots can be observed on the spectra (Luo *et al.*, 2017; Alves, Frantz and Berutti, 2018; Khataee, Hassanzadeh and Kohan, 2018). In detail, a-GQDs prepared at different temperatures for 24 h show IR stretches at 3426 cm^{-1}, 1740 cm^{-1}, 1611 cm^{-1}, 1140 cm^{-1} and 849 cm^{-1} for -OH, C=O, C=C, C-O and C-C, respectively. The IR stretches of b-QDs prepared at different temperatures for 24 h can be observed at regions of 3407 cm^{-1}, 1730 cm^{-1}, 1621 cm^{-1}, 1129 cm^{-1}, 849 cm^{-1}, corresponding to -OH, C=O, C-O and C-C functional groups, respectively.

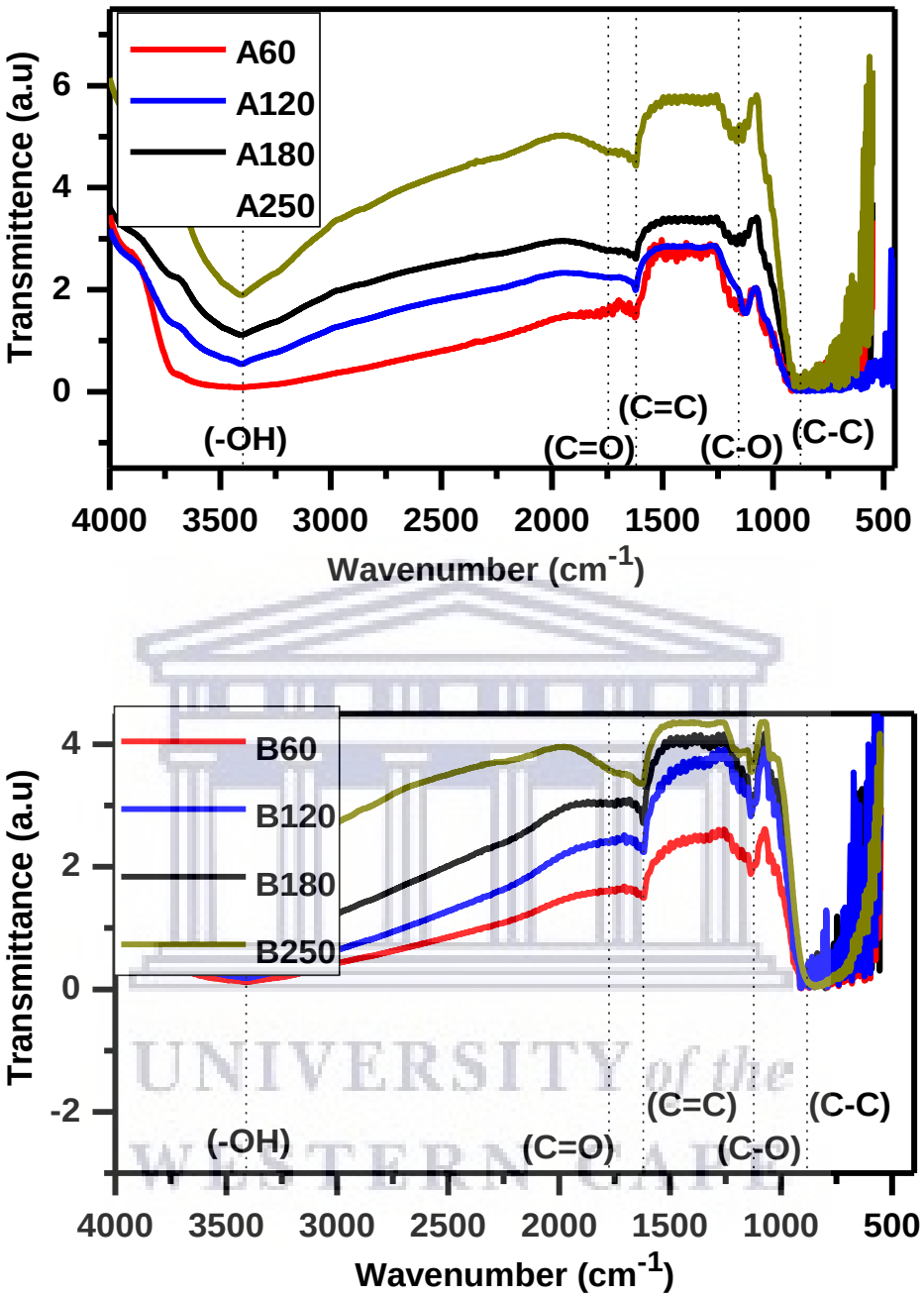

Figure 3.3: FTIR spectra of A- and B-GQDs prepared under reflux at different temperatures.

The appearance of these functional groups signifies the presence of graphene quantum dot structures. These results imply that GQDs were successfully synthesised, concurrent with other studies reported in literature.

3.3.1.3 High Resolution-Transmission Electron Microscopy (HR-TEM)

The particle size distribution of the prepared graphene quantum dots was studied using high resolution transmission electron microscopy. **Figure 3.4** shows micrographs of the prepared graphene quantum dots from coal at different temperatures (i.e., 60 °C, 120 °C, 180 °C and 250 °C), using two different precursors (i.e., anthracite and bituminous coal). The samples consist of homogenous spherical nanoparticles, which increases in dispersion as the particle size decreases. This implies that at high synthesis temperatures, the particle size of the quantum dots decreases, and this improves the dispersion of the nanoparticles, subsequently decreasing the band gap (Jang, Shin and Choi, 2018; Kholikov *et al.*, 2018). The (002) interlayer spacing of graphene quantum dots was also found to be 0.17 nm, larger than that of bulk coal 0.21 nm.

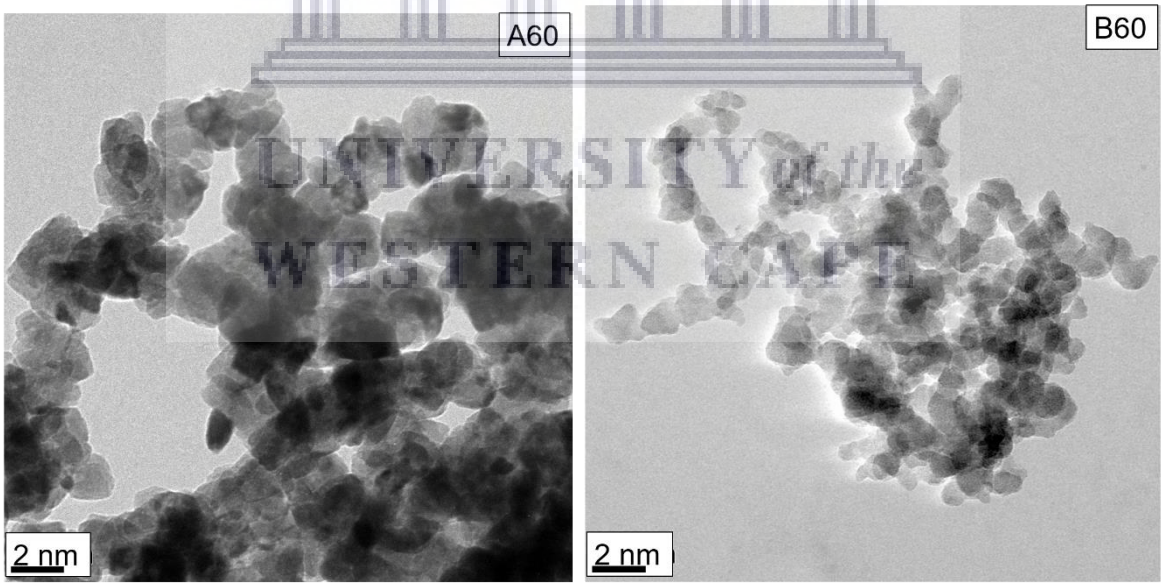

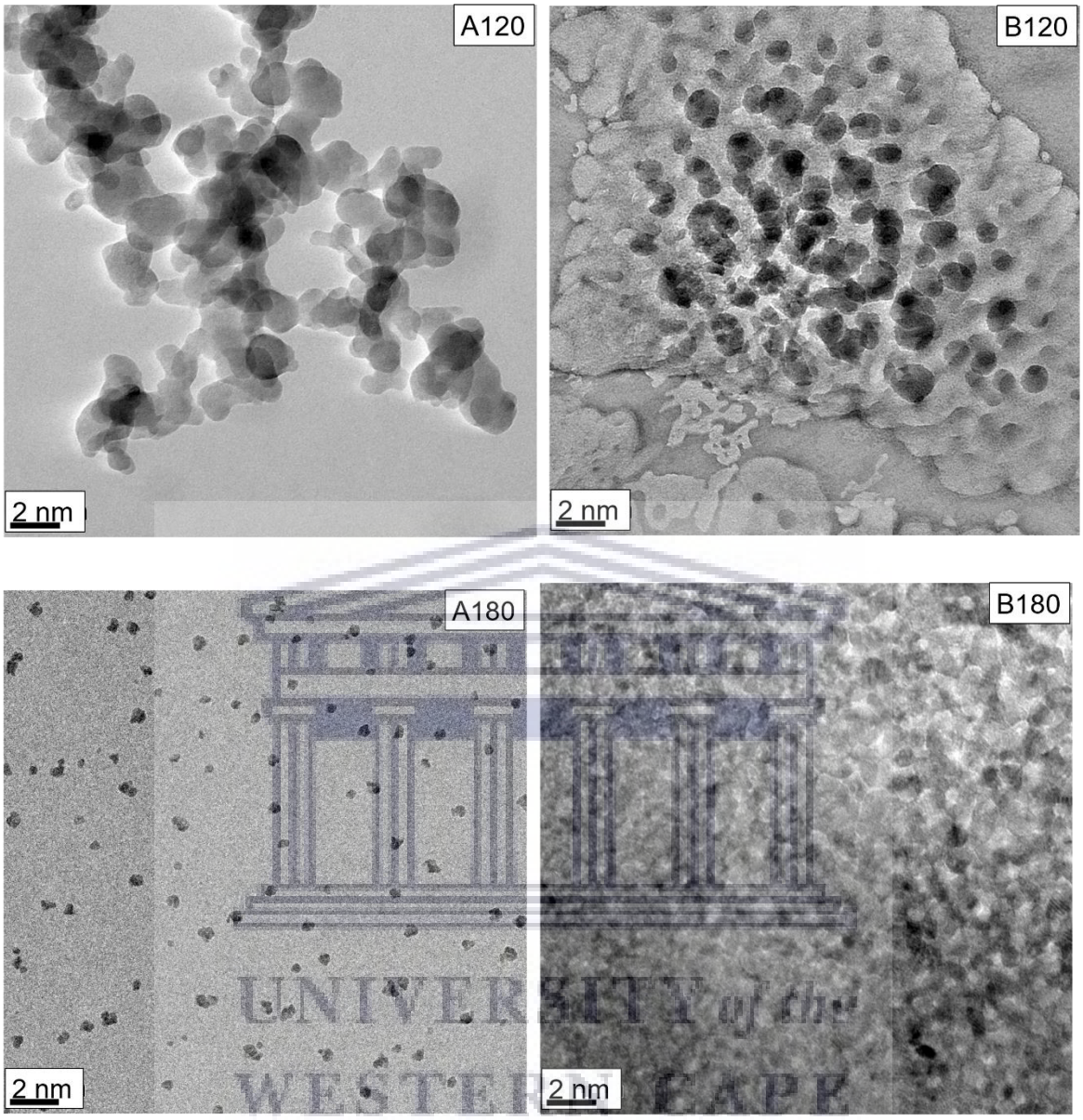

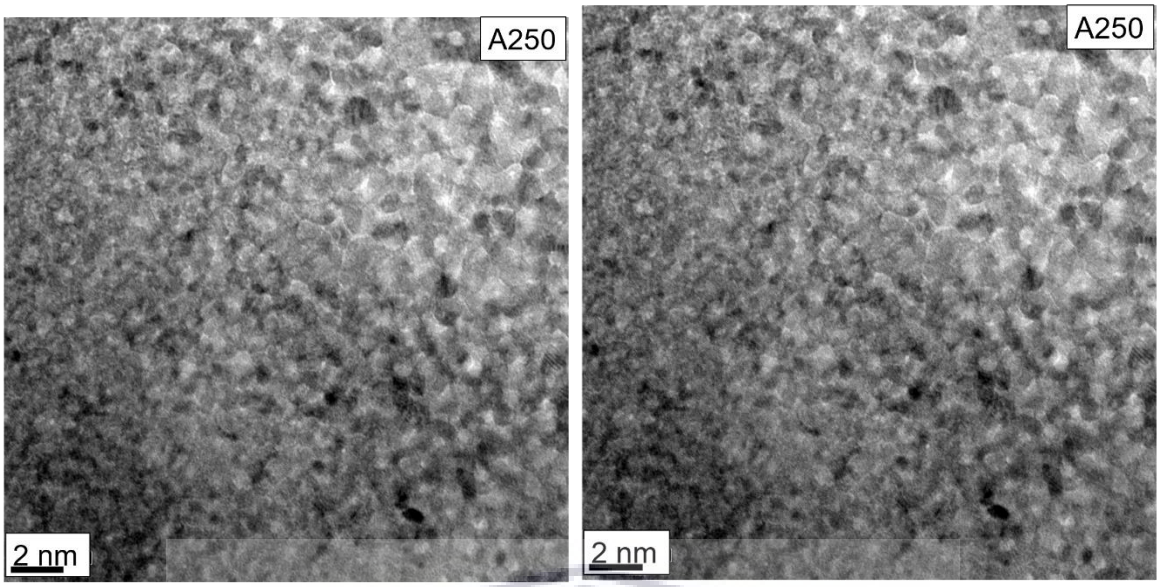

Figure 3.4: Transmission Electron Microscopy (TEM) of GQDs prepared using A-anthracite coal and B-bituminous coal prepared at different synthetic temperatures.

From the TEM micrographs presented on **Fig. 3.4**, it may be observed that the particle size of the prepared graphene quantum dots decreases, with increasing synthesis temperature. TEM histograms and SAXs spectroscopy particle sizes are presented below for further analysis of the quantum dot structures.

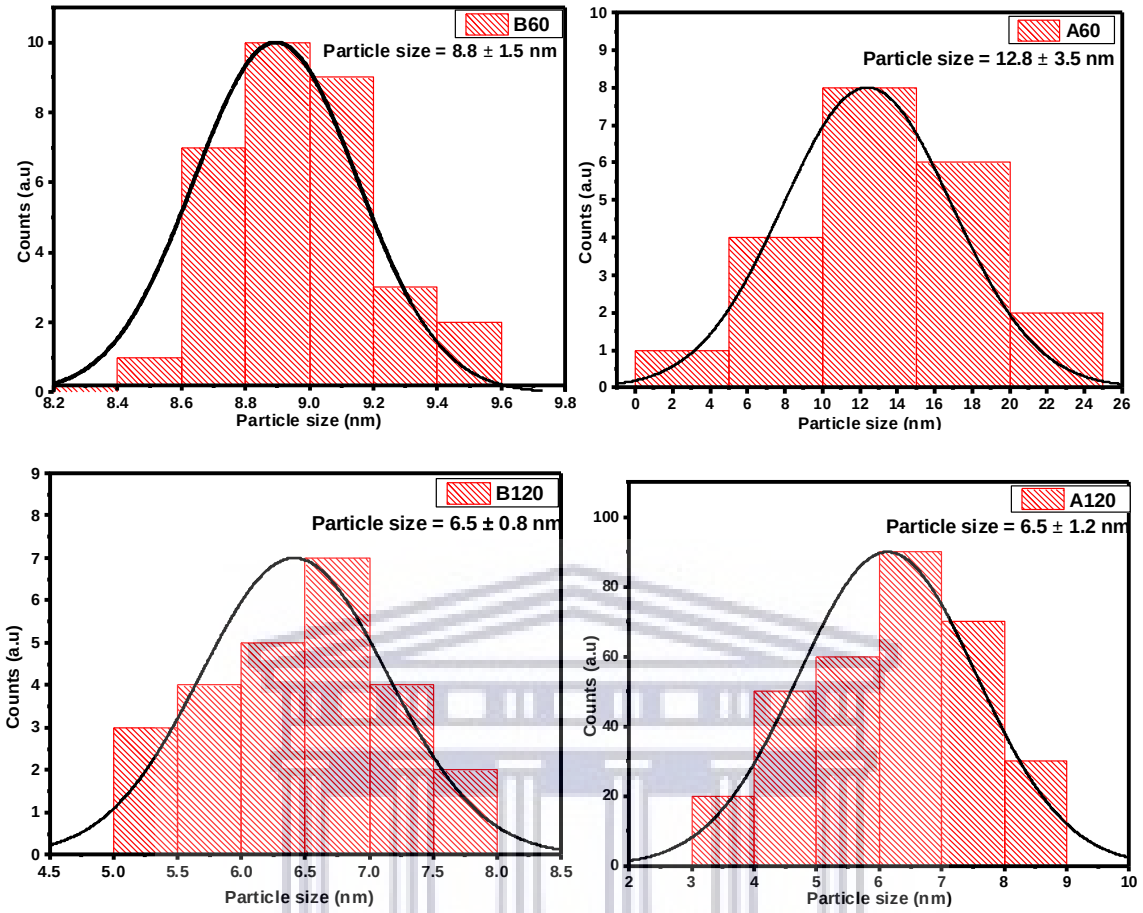

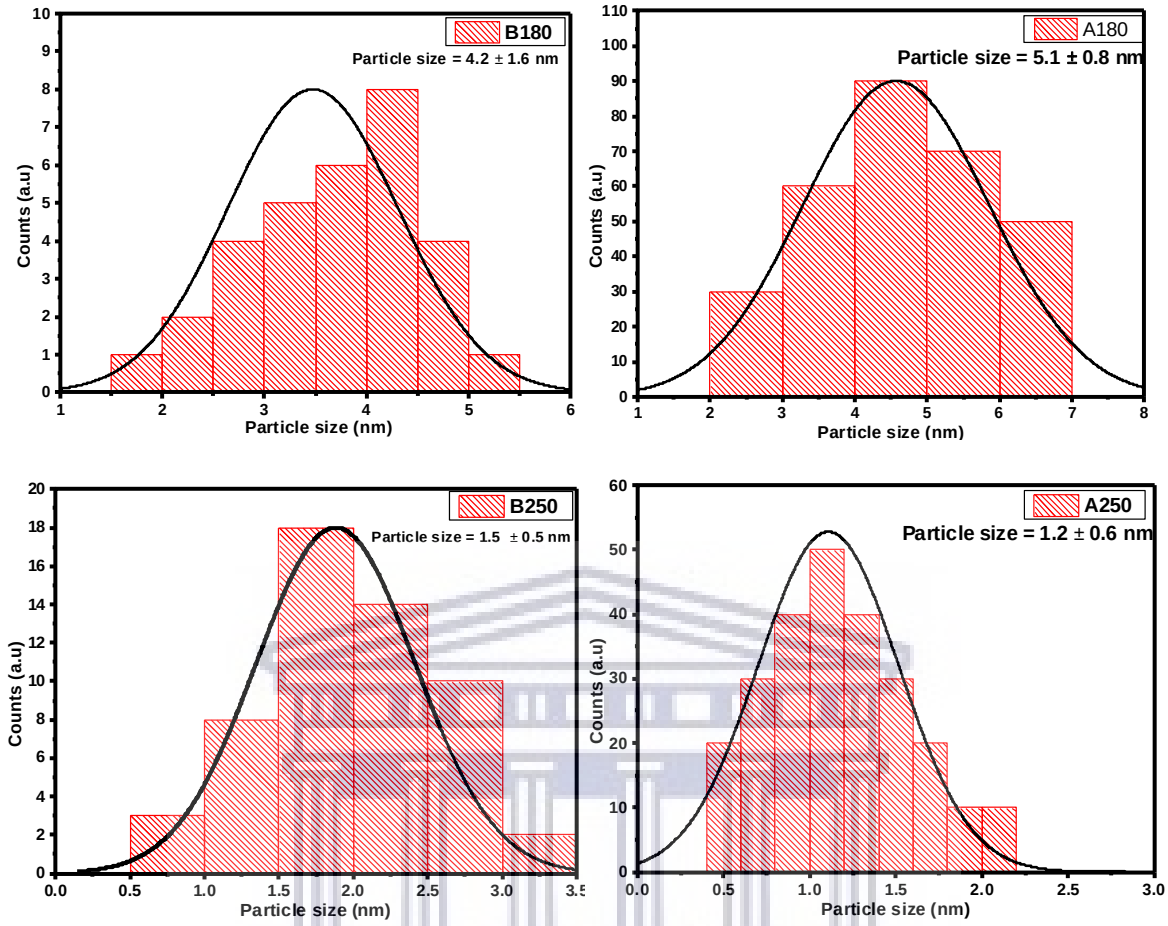

Figure 3.5: TEM histograms and SAXS spectroscopy particle sizes of the prepared graphene quantum dots at different temperatures using different precursors

The particle sizes of the prepared graphene quantum dots, from anthracite were calculated to be (12.8 ± 3.5, 6.5 ± 1.2, 5.1 ± 0.8 and 1.8 ± 0.4) nm for A60, A120, A180 and A250, respectively. Those prepared from bituminous coal were calculated to be (9.1 ± 0.7, 6.5 ± 0.8, 4.2 ± 1.6 and 1.7 ± 0.5) nm for B60, B120, B180 and B250, respectively. The variation in particle sizes of the graphene quantum dots is highly favoured in this research study, since it is envisaged from literature that the different band gaps will improve the solar absorption coefficient efficiency of the device.

3.3.2 Optical properties of graphene quantum dots

3.3.2.1 Photoluminescence Spectroscopy

One of the most attractive properties of quantum dots is that they can be optically excited. When they are optically excited, the electrons in QDs gain energy, creating excitons. An exciton is a bound state of an electron and a hole. After relaxation from the excitonic excited state to its lower energy state, the electron and hole recombine, emitting a photon in the process (Suresh, 2014; Moos *et al.*, 2019). The overall process of optical excitation, relaxation of excited state, recombination of electron-hole pairs and fluorescent emission is called photoluminescence (PL). The PL spectrum is obtained when the number of photons emitted are measured as a function of energy. QDs can be excited by many light sources within a large wavelength range, since QDs have continuous and broad absorption spectra, as compared to organic dyes (Alemu, Albuquerque and Herman, 2018; Xu *et al.*, 2018). A typical example of this phenomenon is presented in the work done in this study (**Figure 3.6**), all the obtained graphene quantum dots were excited at different excitation wavelengths to study how the excitation wavelength affects the emission wavelength. When the prepared graphene quantum dot materials were excited at different excitation wavelength, no shift in the emission wavelengths was observed. This due to the difference in the morphology and particle size of the quantum dots (Kong *et al.*, 2018). However, those prepared at 250 °C experienced a shift in the emission wavelength with respect to the excitation wavelengths (up-conversion property). Quantum dots which exhibit this phenomenon are mostly preferred for LED TV, computer and cell phone screens.

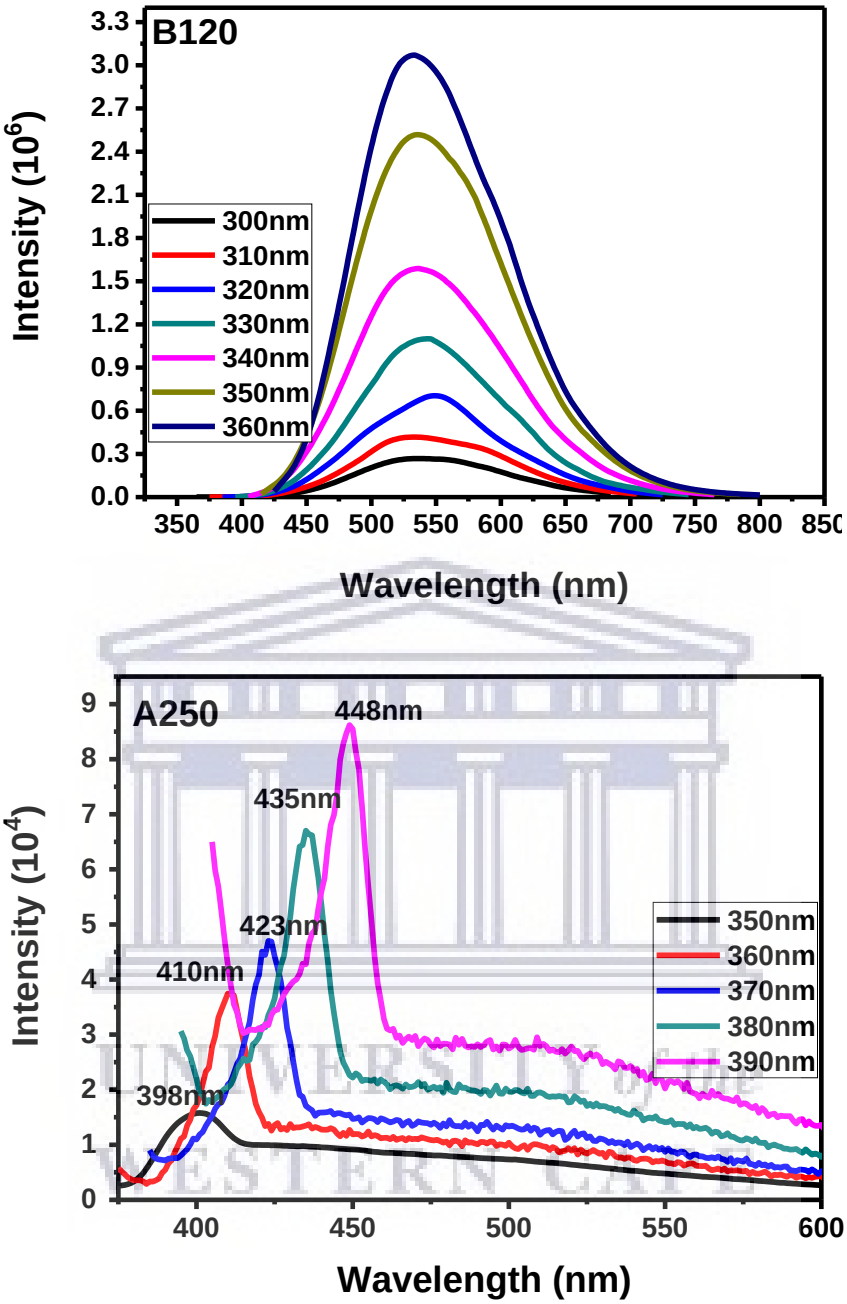

Figure 3.6: A typical fluorescence spectrum of graphene quantum dots prepared from coal at different temperatures; A 120 °C, B 250 °C and excited at different excitation wavelengths

Combination of the fluorescence spectra of the prepared GQDs (**Figure 3.7**) revealed the Red Orange Yellow Green Blue Indigo Violet (ROYGBIV) emission wavelengths. Which implies that the materials undergo up-conversion, also that the

emission wavelengths from the visible region of the solar spectrum for photovoltaic application have been covered.

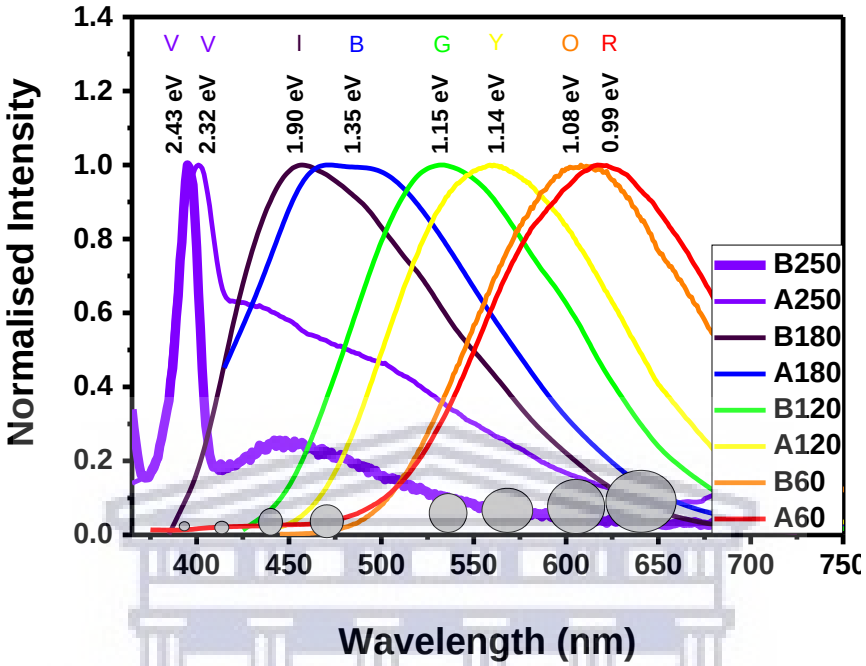

Figure 3.7: Fluorescence spectra of a-GQDs and b-GQDs prepared at different temperatures.

3.3.2.2 Ultraviolet-visible (UV-vis) spectroscopy

When electrons in a molecule are excited from one energy level to a higher energy level, molecular transitions occur. The change in energy associated with the transition determines many molecular properties such as colour and provides information on the structure of a molecule. These transitions that occur in a molecule can be studied using techniques such as UV-vis spectroscopy (Ahmad *et al.*, 2018; Allahbakhsh and Bahramian, 2018; Argudo *et al.*, 2019). The prepared graphene quantum dots dissolved in chlorobenzene exhibited different colours with respect to their different sizes (i.e., red, orange, yellow, green, blue, indigo and violet), these solutions were spin coated onto glass substrate to obtain thin films. **Figure 3.8 A&B** show the absorbance spectra and Tauc plots of a- and b-GQDs prepared at different

synthesis temperatures for 24 h, respectively. On the absorbance spectra, a characteristic absorption peak at 230 nm was observed, assigned to the π-π* transitions of aromatic sp^2 domains. Besides the strong π-π* absorption peaks, a new absorption band at higher wavelengths was also observed due to n-π* transitions and these absorbances cover wavelengths of the visible region in the solar spectrum (Kong *et al.*, 2018; Tian *et al.*, 2018; Wang *et al.*, 2018). The decrease in absorption wavelength with increasing synthesis temperature evidences the reduction in particle size and existence of the quantum confinement effect.

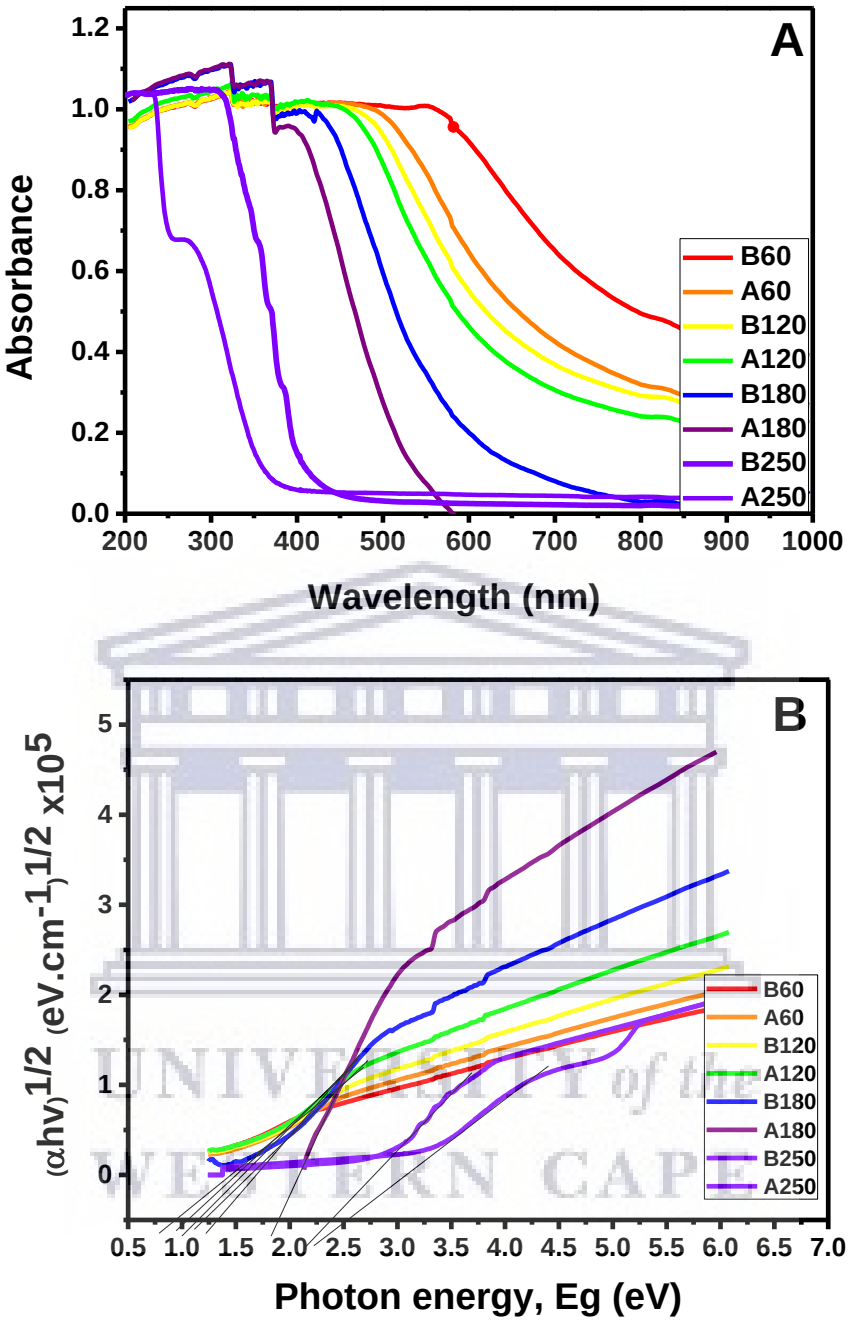

Figure 3.8: A. Absorbance spectra and B. Tauc plots of a- and b-GQDs prepared at different synthesis temperatures for 24 h

In detail, the band gaps including π-π* and n-π* transitions which occur in the system are presented on **Table 3.1** below.

Table 3.1: Detailed analysis of the absorbance results for the graphene quantum dots shown in Figure 3.8

Sample	π-π* transitions (nm)	n-π* transitions (nm)	Band gap (eV)
A60	366	556	0.99
B60	366	495	1.08
A120	366	478	1.14
B120	366	451	1.16
A180	366	423	1.36
B180	366	394	1.90
A250	309	355	2.32
B250	232	272	2.43

Quantum confinement is observed when the particle size of a material is too small to be comparable to the wavelength of the electron. When graphene is chemically cut to sizes less than 40 nm, electron motion in the molecule is restricted to specific energy levels; characteristic of an atomic particle (Alidad *et al.*, 2018; Li *et al.*, 2018). It can be observed from **Table 3.1** that the decrease in the particle size induces a blue shift in the spectra. A decrease in size of graphene to the nanoscale, causes electron confinement of the energy levels to be discrete, and this increase or widens up the band gap energy. Since the band gap and the wavelength are inversely proportional to each other, the wavelength decreases with decreasing particle size, evidenced by emission of blue radiation.

3.3.3 Electrochemistry

3.3.3.1 Cyclic voltammetry

A successful use of CV measurements for the determination of the band structure parameters (i.e., band gap (ε_{gap}^{qp}), the conduction band edge (e_1 LUMO) and valence band edge (h_1 HOMO)) are described in detail. The electron transfer with the GQDs is mediated through e_1 and h_1, which are manifested as respective cathodic and anodic peaks in the CVs. The decrease in particle size of GQD causes the anodic and cathodic peaks to shift toward more positive and negative potentials, respectively. Thus, the size quantisation effect (SQE) can readily be confirmed by simple voltammetric experiments. In the present investigation, the CV measurements were carried out on GQDs dispersions. Thus, the charge transfer can be viewed as a formation of the noninteracting electron−hole pair. The potential difference between cathodic and anodic peaks is correlated to the single particle or quasi-particle gap (ε_{gap}^{qp}). **Figure 3.9** shows the cyclic voltammetric measurements of the graphene quantum dot materials run in the presence of tetrabutylammonium perchlorate electrolyte, using glassy carbon working electrode. The band gaps of these materials were thereafter calculated using equation [3.1]:

$$E_g = \mathrm{E(LUMO)} - E(HOMO) \qquad [3.1]$$

$$E(\mathrm{HOMO}) = -e[E_{ox}^{onset} - 4.4] \qquad [3.1.1]$$

$$E(\mathrm{LUMO}) = -e[E_{ox}^{onset} - 4.4] \qquad [3.1.2]$$

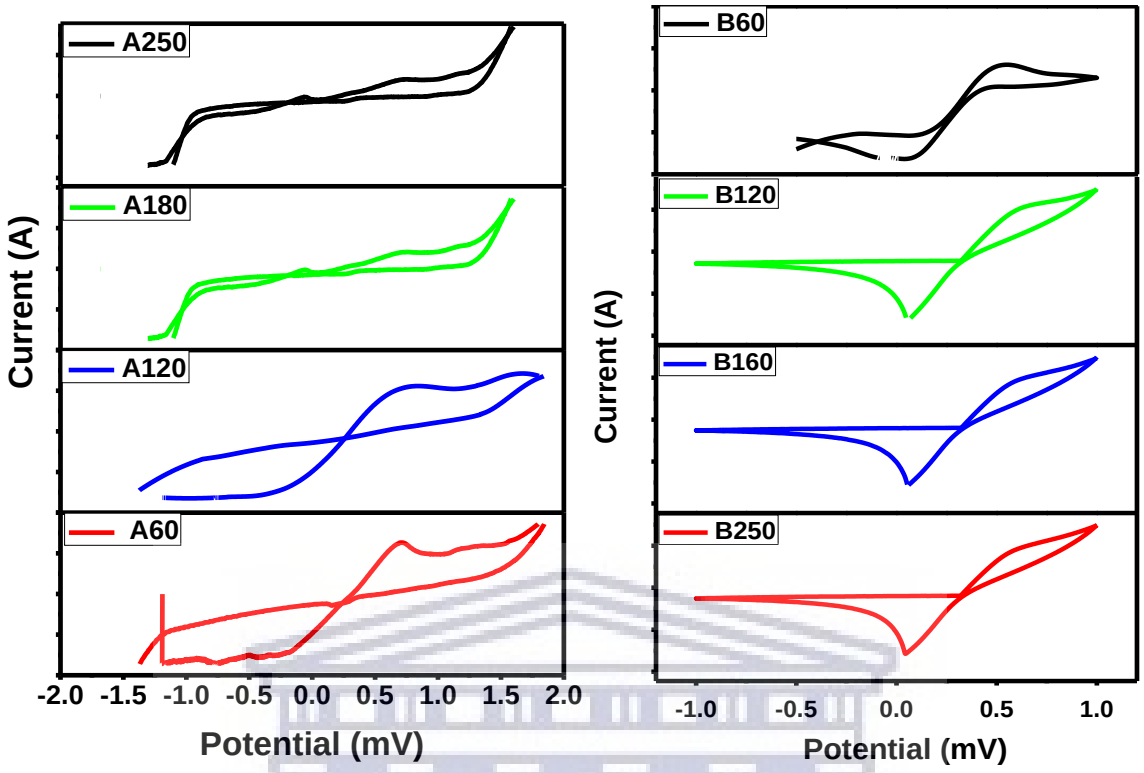

Figure 3.9: Cyclic voltammetry (CV) of a-GQDs and b-GQDs prepared at different temperatures

The cyclic voltammetry of the graphene quantum dots shows similar behaviour to other graphene quantum dots prepared from the same coal precursor (anthracite or bituminous coal). However, introduction of the band gap to graphene increases the CV currents showing a better electroactivity (Bayat and Saievar-Iranizad, 2017; Masteri-Farahani and Askari, 2019). Graphene quantum dots prepared from these coal precursors show a 1 electron reversible reaction with a widening in the peak position as the quantum dot size decreases. The calculated electrochemical band gaps correspond to the obtained results from UV-vis spectroscopy. In summary, the electrochemical band gaps were found to be (1.01, 1.14, 1.40 and 2.30) eV for B60, B120, B180 and B250, respectively. Those of A60, A120, A180 and A250 were found to be (1.10, 1.15, 2.00 and 2.40) eV respectively. These results are closely related or complaisant to/with the band gaps obtained on UV-vis results.

3.3.3.2 Electrochemical Impendence spectroscopy

Figure 3.10 shows the Nyquist diagrams for the a- and b-GQDs materials prepared at different synthetic temperatures. Except for A250 and B250 quantum dot materials, all the Nyquist plots for the other graphene quantum dots show straight lines, implying a high electron transfer between the quantum dots and the electrolyte. This property is desirable for materials to be applied as donor materials in solar cells. The semicircles, on the Nyquist plots of GQDs with high band gaps (A250 and B250) correspond to the charge transfer resistance-limiting process that is associated with the GQD/electrolyte interface (R_{CT}) and are similar for the b-GQD (Hong *et al.*, 2018; Zhang *et al.*, 2019). Although, the R_{CT} values increase in the following order: R_{CT} B250 > B180 > B120 > B60. Those prepared from anthracite precursor show R_{CT} values that increase in the following order: A250 > A180 > A120 > A60.

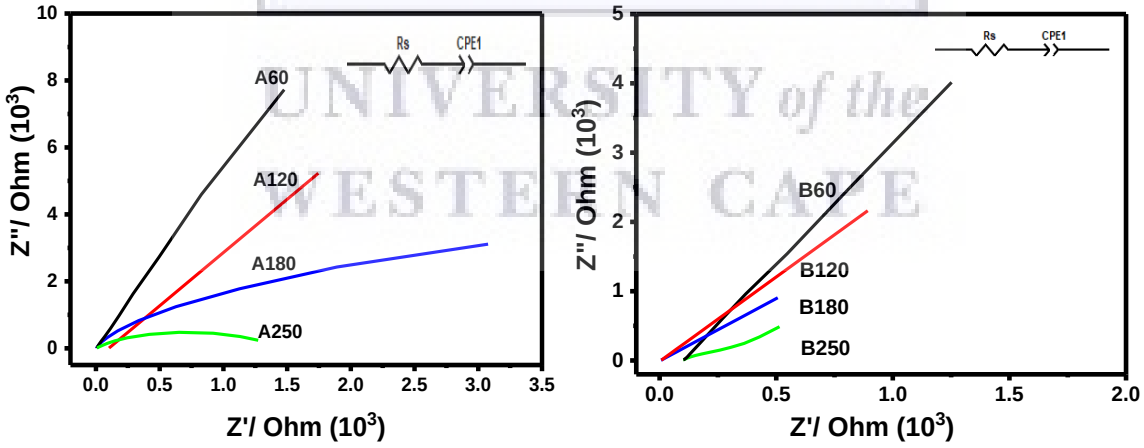

Figure 3.10: Electrochemical impendence spectroscopy of the prepared a and b-graphene quantum dots, respectively.

Constant-phase elements (CPE) are largely used in corresponding electrical circuits for fitting of experimental impedance data. The CPE behaviour is usually linked to distributed surface reactivity, roughness or fractal geometry, surface inhomogeneity,

electrode porosity, and to current and potential distributions associated with electrode geometry. Different electrochemical systems showing the CPE dependence in the high-frequency range for the overall impedance were considered in this study. And the local electrochemical impedance spectroscopy was found to provide a good means for assessing the influence of local variations on the CPE behaviour seen in global impedance measurements.

3.4 Conclusion

Graphene quantum dots of different size regimes were successfully harvested from the abundant mineral, coal. Structural characterisation by ^{13}C-NMR prove existence of sp^2-hybridised carbons from the π-electron conjugated carbon lattice on the GQDs and sp^3-hybridised carbons from the primary carbons on GQDs. FTIR spectroscopy shows characteristic fingerprint vibrational bands of the prepared GQDs, in conjunction with NMR to prove existence of the sp^2-carbons from graphene. Morphological studies show a decrease in particle size with increasing synthesis temperature due to quantum confinement in the system. This is further confirmed by optical studies performed on the materials. Both the electrochemical and optical band gaps cover the visible and UV region of the solar spectrum, properties desirable in this study for application in rainbow solar cells.

References

Ahmad, U. *et al.* (2018) 'Synthesis and characterization of InN quantum dots for optoelectronic applications', *Optik*, 173, pp. 97–100.

Alemu, Y. A., Albuquerque, G. H. and Herman, G. S. (2018) 'Enhanced photoluminescence from CuInS2/ZnS quantum dots: Organic superacid passivation', *Materials Letters*, 219, pp. 178–181.

Alidad, F. *et al.* (2018) 'Production of pristine graphene quantum dots from graphite by a shear-mixer in supercritical CO2', *Chemical Physics Letters*, 710, pp. 64–69.

Allahbakhsh, A. and Bahramian, A. R. (2018) 'Self-assembly of graphene quantum dots into hydrogels and cryogels: Dynamic light scattering, UV–Vis spectroscopy and structural investigations', *Journal of Molecular Liquids*, 265, pp. 172–180.

Alves, A. K., Frantz, A. C. S. and Berutti, F. A. (2018) 'Microwave-assisted oleothermal synthesis of graphene-TiO2 quantum dots for photoelectrochemical oxygen evolution reaction', *FlatChem*, pp. 1–24.

Argudo, P. G. *et al.* (2019) 'Fluorinated CdSe/ZnS quantum dots: Interactions with cell membrane', *Colloids and Surfaces B: Biointerfaces*, 173, pp. 148–154.

Bayat, A. and Saievar-Iranizad, E. (2017) 'Synthesis of green-photoluminescent single layer graphene quantum dots: Determination of HOMO and LUMO energy states', *Journal of Luminescence*, 192, pp. 180–183.

Dong, P. *et al.* (2014) 'Graphene on Metal Grids as the Transparent Conductive Material for Dye Sensitized Solar Cell', *The Journal of Physical Chemistry C*, 118(45), pp. 25863–25868.

Duan, W. *et al.* (2018) 'Thermoelectric and thermal transport properties of graphene under strong magnetic field', *Physica E: Low-dimensional Systems and*

Nanostructures, 104, pp. 173–176.

Far'ain Md Noor, N. *et al.* (2018) 'Synthesis of white fluorescent pyrrolic nitrogen-doped graphene quantum dots', *Optical Materials*. North-Holland, 83, pp. 306–314.

Frasco, M. F. and Chaniotakis, N. (2010) 'Bioconjugated quantum dots as fluorescent probes for bioanalytical applications', *Analytical and Bioanalytical Chemistry*, 396, pp. 229–240.

Fürst, A., Pretsch, E. and Robien, W. (1990) 'Comprehensive parameter set for the prediction of the 13C-NMR chemical shifts of sp3-hybridized carbon atoms in organic compounds', *Analytica Chimica Acta*, 233, pp. 213–222.

Hayashi, S. *et al.* (2003) '13C NMR study of 13C-enriched single-wall carbon nanotubes synthesized by catalytic decomposition of methane', *Carbon*, 41(15), pp. 3047–3056.

He, S. *et al.* (2018) 'Band structures of blue luminescent nitrogen-doped graphene quantum dots by synchrotron-based XPS', *Surface Science*, 676, pp. 51–55.

Hong, S. *et al.* (2018) 'Slurry erosion-corrosion resistance and microbial corrosion electrochemical characteristics of HVOF sprayed WC-10Co-4Cr coating for offshore hydraulic machinery', *International Journal of Refractory Metals and Hard Materials*, 74, pp. 7–13.

Iqbal, M. Z. and Rehman, A.-U. (2018) 'Recent progress in graphene incorporated solar cell devices', *Solar Energy*, 169, pp. 634–647.

Jang, C. W., Shin, D. H. and Choi, S.-H. (2018) 'Highly-flexible and -stable deep-ultraviolet photodiodes made of graphene quantum dots sandwiched between graphene layers', *Dyes and Pigments*, 168, pp. 238-242.

Kalluri, A. *et al.* (2018) 'Graphene Quantum Dots: Synthesis and Applications', *Methods in Enzymology*, 1 , pp. 335–354.

Kelarakis, A. (2015) 'Graphene quantum dots: In the crossroad of graphene, quantum dots and carbogenic nanoparticles', *Current Opinion in Colloid and Interface Science*, 20, pp. 354–361.

Khataee, A., Hassanzadeh, J. and Kohan, E. (2018) 'Specific quantification of atropine using molecularly imprinted polymer on graphene quantum dots', *Spectrochimica Acta - Part A: Molecular and Biomolecular Spectroscopy*, 205, pp. 614–621.

Kholikov, K. *et al.* (2018) 'Improved singlet oxygen generation and antimicrobial activity of sulphur-doped graphene quantum dots coupled with methylene blue for photodynamic therapy applications', *Photodiagnosis and Photodynamic Therapy*, 24, pp. 7–14.

Kong, W. *et al.* (2018) 'Investigation of photoluminescence behavior of reduced graphene quantum dots', *Inorganic Chemistry Communications*, 99, pp. 199-205

Liu, D. *et al.* (2020) 'The photovoltaic performance of CdS/CdSe quantum dots co-sensitized solar cells based on zinc titanium mixed metal oxides', *Physica E: Low-dimensional Systems and Nanostructures*, 115, pp. 113669.

Latil, S. *et al.* (2001) 'C 13 NMR Chemical Shift of Single-Wall Carbon Nanotubes', *Physical Review Letters*, 86, pp. 3160–3163.

Li, C. *et al.* (2018) 'Asymmetric quantum confinement-induced energetically and spatially splitting Dirac rings in graphene/phosphorene/graphene heterostructure', *Carbon*, 140, pp. 164–170.

Luo, P. *et al.* (2017) 'New insight into electrooxidation of graphene into graphene quantum dots', *Chemical Physics Letters*, 690, pp. 129–132.

Mahmoudi, T., Wang, Y. and Hahn, Y.-B. (2018) 'Graphene and its derivatives for solar cells application', *Nano Energy*, 47, pp. 51–65.

Masteri-Farahani, M. and Askari, F. (2019) 'Design and photophysical insights on graphene quantum dots for use as nanosensor in differentiating methamphetamine and morphine in solution', *Spectrochimica Acta Part A: Molecular and Biomolecular Spectroscopy*, 206, pp. 448–453.

Mirnajafizadeh, F. *et al.* (2016) 'Hydrothermal synthesis of highly luminescent blue-emitting ZnSe(S) quantum dots exhibiting low toxicity', *Materials Science and Engineering: C*, 64, pp. 167–172.

Moos, R. *et al.* (2019) 'Assessing electronic states of InAsP/GaAs self-assembled quantum dots by photoluminescence and modulation spectroscopy', *Journal of Luminescence*, 206, pp. 639–644.

Nideep, T. K., Ramya, M. and Kailasnath, M. (2019) 'The influence of ZnS buffer layer on the size dependent efficiency of CdTe quantum dot sensitized solar cell', *Superlattices and Microstructures*, 130, pp. 175–181.

Omidvar, A., RashidianVaziri, M. R. and Jaleh, B. (2018) 'Enhancing the nonlinear optical properties of graphene oxide by repairing with palladium nanoparticles', *Physica E: Low-dimensional Systems and Nanostructures*, 103, pp. 239–245.

Pourmahmoud, V. and Rezaei, B. (2019) 'Manipulation of Bragg and graphene photonic band gaps in one-dimensional photonic crystal containing graphene', *Optik*, 185, pp. 875–880.

Reshma, V. G. and Mohanan, P. V. (2019) 'Quantum dots: Applications and safety consequences', *Journal of Luminescence*, 205, pp. 287–298.

Santiago, S. R. M. *et al.* (2017) 'Synthesis of N-doped graphene quantum dots by pulsed laser ablation with diethylenetriamine (DETA) and their photoluminescence', *Physical Chemistry Chemical Physics*, 19(33), pp. 22395–22400.

Sbrockey, N. M. *et al.* (2018) 'Synthesis and characterization of graphene based

thermoacoustic devices', *Journal of Crystal Growth*, 493, pp. 41–44.

Sharma, V. K. *et al.* (2017) 'Assessment of toxicity of selenium and cadmium selenium quantum dots: A review', *Chemosphere*, 188, pp. 403–413.

Sk, M. A. *et al.* (2014) 'Revealing the tunable photoluminescence properties of graphene quantum dots', *J. Mater. Chem. C*, 2(34), pp. 6954–6960.

Suresh, A. K. (2014) 'Extracellular bio-production and characterization of small monodispersed CdSe quantum dot nanocrystallites', *Spectrochimica Acta Part A: Molecular and Biomolecular Spectroscopy*, 130, pp. 344–349.

Tian, P. *et al.* (2018) 'Graphene quantum dots from chemistry to applications', *Materials Today Chemistry*, 10, pp. 221–258.

Wang, Y. *et al.* (2018) 'Post-epoxidation of graphene quantum dots', *Chemical Physics Letters*, 706, pp. 140–144.

Wehrenberg, B. L., Wang, C. and Guyot-Sionnest, P. (2002) 'Interband and Intraband Optical Studies of PbSe Colloidal Quantum Dots', *The Journal of Physical Chemistry B*, 106, pp. 10634–10640.

Xu, A. *et al.* (2018) 'Selective supramolecular interaction of ethylenediamine functionalized graphene quantum dots: Ultra-sensitive photoluminescence detection for nickel ion in vitro', *Synthetic Metals*, 244, pp. 106–112.

Ye, R. *et al.* (2013) 'Coal as an abundant source of graphene quantum dots.', *Nature Communications*, 4, p. 2943.

Zhang, J. *et al.* (2018) 'Mechanical and electronic properties of graphene nanomesh heterojunctions', *Computational Materials Science*, 153, pp. 64–72.

Zhang, M. *et al.* (2019) 'Synthesis of BixMoyOz/BiaWbOc nanocomposite by pH tuning with high electrochemical performance', *Journal of Electroanalytical Chemistry*, 832, pp. 303–310.

Zhao, N. *et al.* (2009) 'Close-Packed Superlattices of Side-by-Side Assembled Au-CdSe Nanorods', *Nano Letters*, 9, pp. 3077–3081.

Zhu, S. *et al.* (2015) 'The photoluminescence mechanism in carbon dots (graphene quantum dots, carbon nanodots, and polymer dots): current state and future perspective', *Nano Research*, 8, pp. 355–381.

CHAPTER 4

Summary

Industrial development and population growth have led to a surge in global demand for energy in the recent years. For this reason, and other challenges facing traditional energy sources; consumers, governments and businesses are increasingly supporting the development of substitute energy sources and new technologies for electricity generation. Solar cells have gained popularity and superiority over other renewable energy sources due to the geographical location of this study. Electron acceptor and electron donor materials with supreme properties are necessary for reaching high PCEs in solar cells. Therefore, in this chapter, the charge-transfer complex formed at the active layer of the solar cell is prepared and evaluated for the suitability of its application.

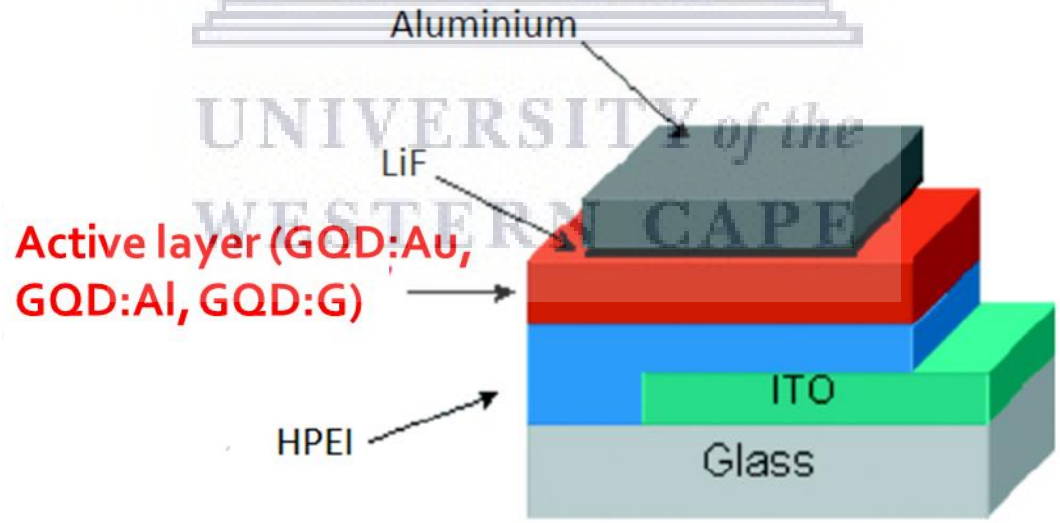

Figure 4.1: Representation of the solar cell active layer that will be of focus in this study

Preparation of metal/graphene quantum dot active layer for Schottky junction solar cells

Abstract

The enigmatic energy harvesting capabilities of SJSCs makes them attractive to researcher's investigative eyes. However, their efficiency is limited due to surface recombination at the interface. Moreover, the wet transfer process of the active layer may give rise to impurities, surface defects and wrinkles. This study uses the graphene quantum dots of different sizes (i.e., different band gaps) which were prepared in Chapter 3 as the donor material for Schottky junction solar cells with 3 different metals (Aluminium, gold, graphene) as acceptors. Optical studies proved the existence of quantum confinement in the GQD molecules and therefore successful synthesis of the quantum dots. The Schottky junction is produced by creating a contact between the prepared graphene quantum dots and three different kinds of metals, comparatively, namely; Aluminium (Al), gold (Au) and graphene (Gr), respectively. Structural characterisation of the nanocomposites prove interaction of the metals with graphene quantum dots through the Al-C and Au-O-Au band stretches evident on FTIR. The 111 and 200 XRD planes of Al metal and 111 XRD plane of Au metal prove interaction of the metals with GQDs (002). The interaction of the metal with semiconductor is further substantiated by electrochemical studies, cyclic voltammetry where the redox couple (active layer) shows a 2-electron ambipolar reversible reaction.

4.1 Introduction

Schottky junction plays an important role in improving electrical and optical properties of photovoltaic (PV) devices (Chen *et al.*, 2018). The Schottky junction formed between a metal and a semiconductor is often modified to arrive at a required barrier height to suit a particular application (Neetika *et al.*, 2019). The contact between the semiconductor and a metal surface induces Fermi-level equilibration (Subramanian, Wolf and Kamat, 2004). For a bulk semiconductor the conduction and valence bands bend to form a space charge region (Hagfeldt and Graetzel, 1995; Büchele *et al.*, 2015). The space charge layer, which is dependent on the carrier density, can extend up to a few micro-meters. When such semiconductor-metal junction is subjected to bandgap excitation in photovoltaic cell, the band bending rectifies the flow of photogenerated charge carriers to produce photocurrent in a solar cell. For semiconductor nanocrystals, the electrons are confined and the individual nanocrystals remain iso-energetic (Anjana, Bindhu and Rakhi, 2019). As a result of this size limitation, the bands remain flat and the charge separation is essentially dictated by the Fermi-level equilibration (Zhang *et al.*, 2018). The different degrees of electron accumulation dictate the Fermi-levels of the nanocrystals and thus creating an energy gradient that drives the electrons toward the collecting electrode.

If the metal in contact with the semiconductor quantum dot is also in the particulate form, electron storage within the particles may occur (Katz E and Wang, 2004; Derkacs *et al.*, 2006). For example, Au nanoparticles possess the property of storing electrons in a quantized way (Teo, Akub and Buraidah, 2019). Electron storage within the gold nanoparticles is facilitated by the double-layer charging around the

metal nanoparticles. When the semiconductor and metal nanoparticles are in contact, the photo-generated electrons are distributed between the semiconductor and metal nanoparticles. Since the electron accumulation increases the Fermi-level of the metal to more negative potentials (Drab and Kralj-Iglič, 2019), the resultant Fermi-level of the composite shifts closer to the conduction band of the semiconductor as may be seen in **Figure 4.2**.

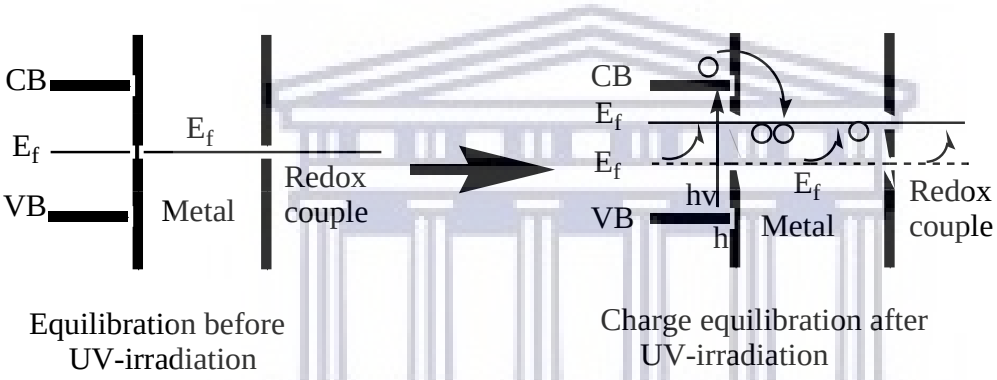

Figure 4.2: Equilibration of the metal-semiconductor nanoparticles with the redox couple, before and after irradiation with UV light.

Improved charge separation and high reductive power of the composite system is evidenced by the negative shift in the Fermi-level (Debehets *et al.*, 2018). This study focuses on the fabrication of Schottky junction solar cells which offer routes to efficiencies exceeding the Shockley-Queisser limit for solar cells via their ability to exploit multiple excitons, their promise in hot carrier extraction, and their enablement of size-tuned tandem and multijunction cells through the use of graphene quantum dots (Kim *et al.*, 2014).

4.2 Methodology

The graphene quantum dots (GQDs) of different band gaps, prepared in Chapter 3 (1.5 mg each, amounting to 12 mg) were dissolved in 0.5 mL of H_2O and heated at 200 °C for 2 min. Consequently, 2.4 mg of metal (Aluminium, Al and Gold, Au) was dissolved in 0.1 mL water. This solution was stirred for 5min while heating at 200 °C to form a homogenous mixture. Different ratios of the GQD:Al, GQD:Au and GQD:G were prepared as (1:1, 1:3, 1:6 and 3:1) for optimisation (presented in the Appendix section), and the optimal ratio was found to be 1:3 from electrochemical efficiencies. Therefore, this chapter focusses on the comparative study of GQD:Al, GQD:Au and GQD:G of the same ratio (1:3) for the active layer of the photovoltaic devices.

4.3 Results and discussion

4.3.1 Structural characterisation

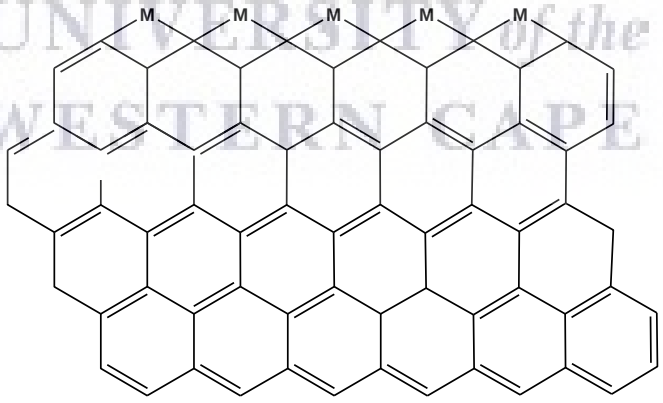

M = Al/Au

Figure 4.3: proposed structure showing the interaction between the metals and graphene quantum dot semi-conductors

The structure shows atomic bonds formed between the metal nanocrystals and graphene quantum dots. This assumption is because the carbons in graphene quantum dots interact with the metals through a type of bonding called π back-bonding (Ni *et al.*, 2019). One way this bonding can occur is by donation of the lone pairs of electrons from carbon to the σ antibonding metallic electrons, resulting in the formation of a σ bond. The other way in-which bonding can occur is by donation of an electron from the filled d-orbital of the metal form the π orbital to the π* antibonding orbital of carbon (Wasson, 2009). The proposed structure of the graphene-graphene quantum dot nanocomposite is presented in **Figure 4.4**.

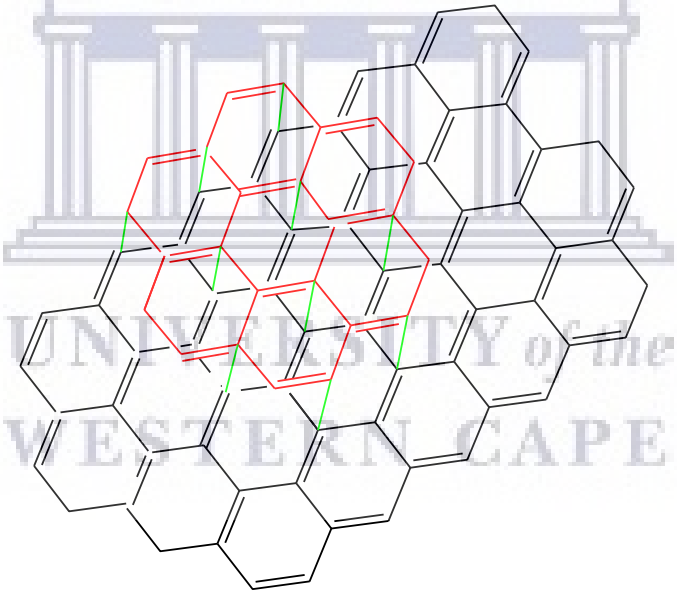

Black = graphene, Red = graphene quantum dots,
Green = van der Waals radius

Figure 4.4: Proposed structure of the bonding between graphene metal and graphene quantum dots semi-conductors

The black sheet represents graphene and the red sheet on top represents graphene quantum dots. The green lines represent the bonds that link graphene and graphene quantum dot sheets. The proposed boning that exists between the two sheets is van

der Waals interaction (Liu, Stradins and Wei, 2016; Laguna and Amador-Bedolla, 2019; Ranea, Dammig Quiña and Moreno Yalet, 2019). The following sections below represents characterisation of the proposed structures above.

4.3.1.1 Fourier-transform infrared spectroscopy

Figure 4.5 shows the functional groups on FTIR spectra of the active layer; GQD:Al, GQD:Au and GQD:G. The influence of the metals on the GQD semiconductors results in broader and intense peaks at 3288.7-3664.5 cm^{-1} for Al-OH and Au-OH respectively, as compared to that of GQD;G at 3232.5 cm^{-1} (-OH).(Baruah *et al.*, 2018; Kumar *et al.*, 2018; Zeng, Jelliss and Buckner, 2018). The weakness of this -OH peak on GQD:G is an indication of the low amount of adsorbed water molecules in the structure. The peaks at 2081.9 cm^{-1} (GQD:Al) and 2100.4 cm^{-1} (GQD:Au) are attributed to C=N stretching vibration of the carboxyl/carbonyl groups attached to the edges of GQD sheets (Jin *et al.*, 2018; Khan *et al.*, 2018). On the GQD:G sample, the C=N peak appears at a region of 3104.7-1724.6 cm^{-1} fused with other functional groups such as; C=O, C=C and C-O. The peaks which appear at 1637.5 cm^{-1}, 1637.7 cm^{-1} and 1520.9 cm^{-1} (for GQD:Al, GQD:Au and GQD:G, respectively) originate from the stretching vibration of aromatic C=C bonds, which represent carbons that remain intact after introduction of the metals, to preserve the graphene structure. The GQD:Al sample shows a sharp peak at 1250.8 cm^{-1} for Al-C functional group, suggesting that Al metal interacts with GQDs not only by formation of a contact but also covalent bond formation. The peak that appears at 661.5 cm^{-1} and 738.9 cm^{-1} can be assigned to the vibrations of Au-O-Au (GQD:Au)

and Al-O-Al (GQD:Al), respectively, substantiating the formation of the GQD-metal redox couple.

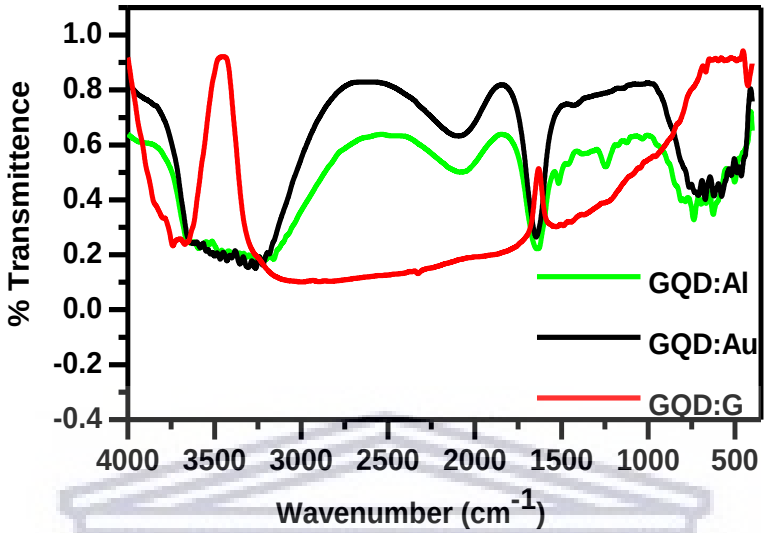

Figure 4.5: Bands assignment observed on FTIR for semiconductor-metal redox couples (GQD:metal)

4.3.1.2 X-ray diffraction (XRD)

X-Ray diffraction analysis is a common means to determine structure and relative configuration of solid compounds in an indisputable way. The prepared materials were also evaluated for their crystallographic structures using XRD. **Figure 4.6** shows the XRD patterns of the solar cell active layer, which is composed of the GQG:Al, GQD:Au and GQD:G nanocomposites. All XRD spectra show the appearance of broad peaks due to the presence of oxygen functionalities on the surface of graphene quantum dots. However, in all the XRD patterns; the miller indices at 2Θ = 20° corresponding to the (002) XRD plane are apparent due to the graphene quantum dot graphitic structure (Mesallam *et al.*, 2018; Bandi *et al.*, 2019). Graphene and graphene quantum dots both possess the same functionalities, same structure but different sizes, and therefore have a fused (002) XRD crystal plane on

the XRD spectrum of GQD:G. Aluminium metal and Gold metal have the same XRD crystallographic structure, hence exhibit the same XRD peaks. It may be seen from the XRD spectra of GQD:Al and GQD:Au that introduction of metals on the GQD structure shows appearance of peaks at 2Θ = 39°, 45°, 65°, 78° and 82° which can be indexed to the (111), (200), (220), (311) and (222) Face-centred-cubic XRD planes of Aluminium and gold, respectively (Kazantsev *et al.*, 2018; Sunderam *et al.*, 2018; Vedhanayagam, Nair and Sreeram, 2019).

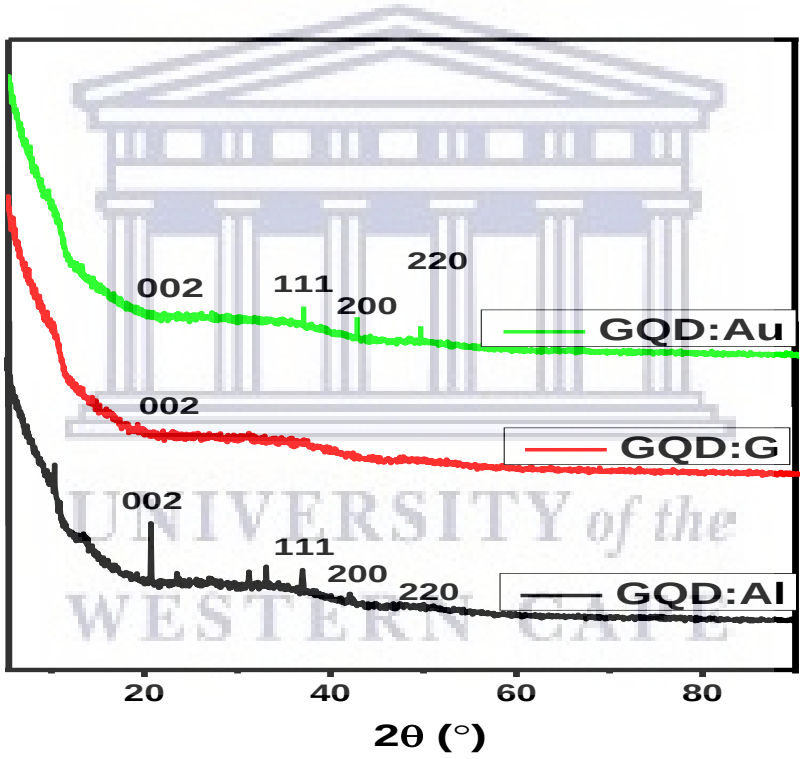

Figure 4.6: X-ray diffraction spectroscopy of GQD:Al, GQD:Au and GQD:G nanocomposites

The appearance of (002) XRD planes of GQDs which can be attributed to the hexagonal graphite structure (of a primitive cubic) that is consisted with 0.34 nm (distance between the graphitic plane), suggest that metal introduction preserved the graphite structures. These XRD results agree with the FTIR results which show

interaction of the metal with the semiconductor functional groups. The XRD modelled crystallographic structures of the prepared nanocomposites are presented on **Figure 4.7** below.

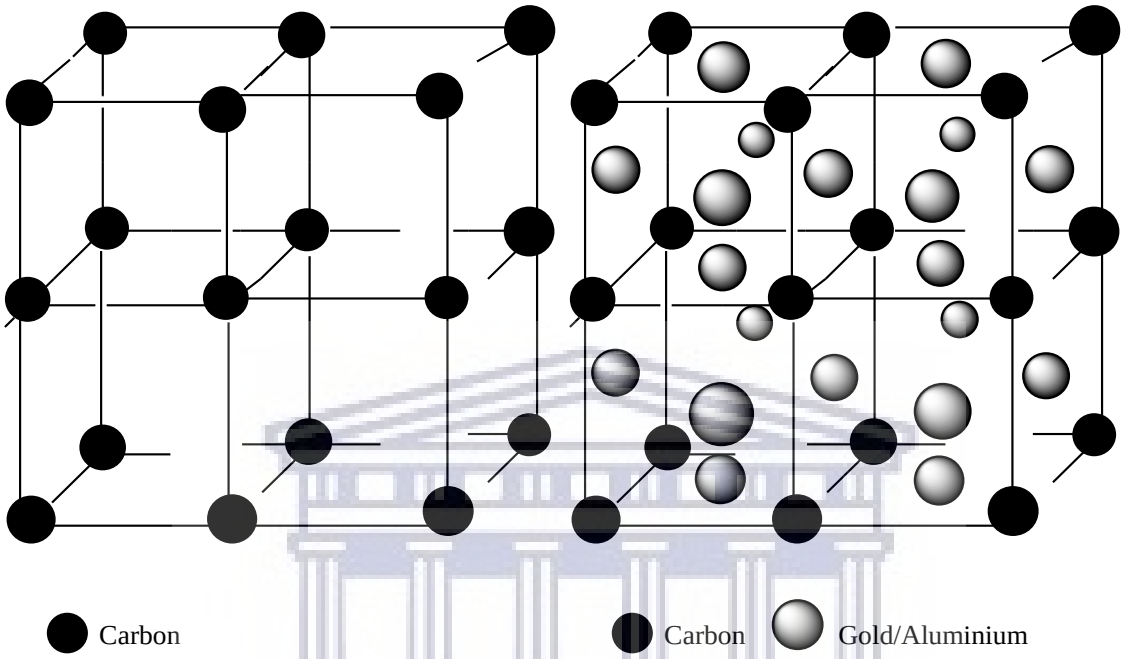

Figure 4.7: Presentation of the modelled XRD crystallographic structure of the prepared materials

4.3.2 Surface and morphological analysis

4.3.2.1 Scanning Electron Microscopy

The interaction of the metal nanoparticles with the semiconducting graphene quantum dots was investigated using Scanning Electron Microscopy. **Figure 4.8** shows the glass spin-coated nanocomposites for comparison, A. shows interaction of GQD with graphene, B. shows interaction of GQD with Aluminium and C. shows interaction of GQD with gold. As can be seen in **Fig. 4.8 A.**, the GQD with graphene nanocomposite forms porous structures with elongated protrusions in between. However, when the GQD are mixed with gold metal nanoparticles, flowerlike structures can be seen on the images, signifying a proximity between the metal and

semiconductor nanoparticles. The same is observed for GQD mixed with Aluminium metal.

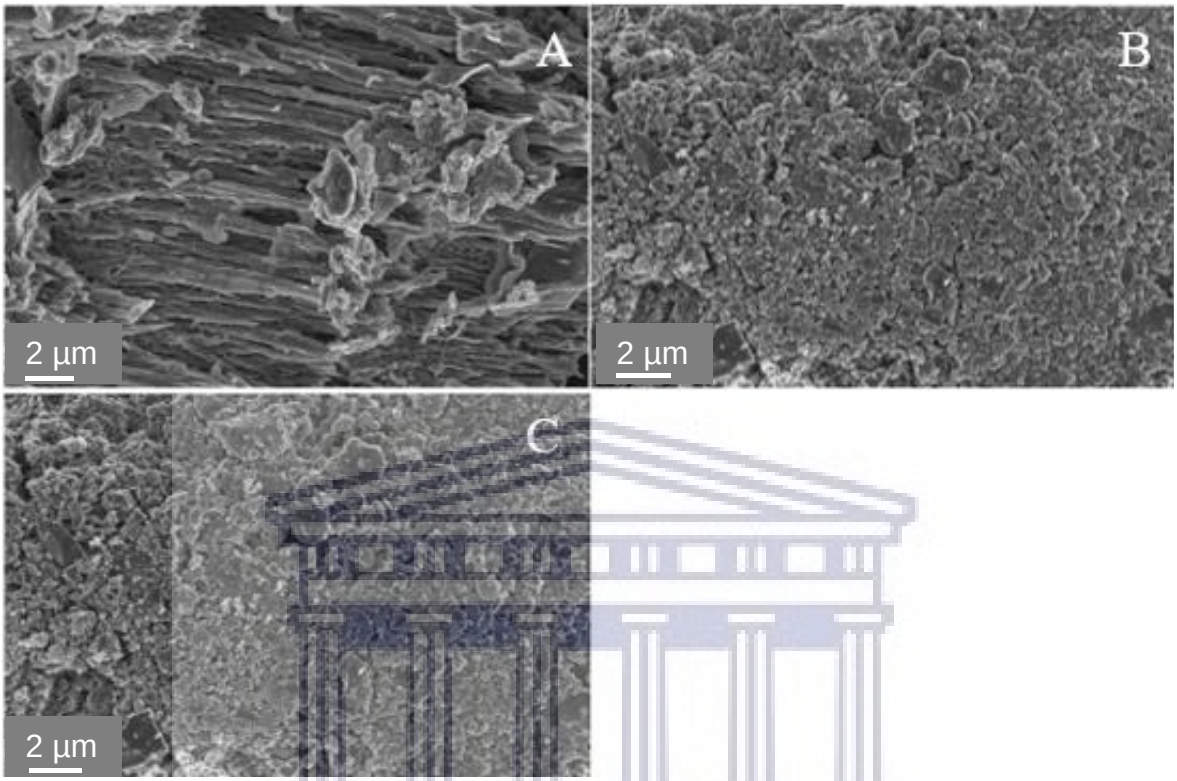

Figure 4.8: Scanning electron microscopy images of the prepared A. GQD:G, B. GQD:Al, and GQD:Au nanocomposites.

4.3.2.2 Transmission Electron Microscopy

When the morphologies of the nanocomposites (active layer; GQD:Al, GQD:Au and GQD:G) were viewed under a higher resolution microscopy, transmission electron microscopy, clearer images resulting in interaction of the metal with semiconductor were obtained and presented in **Figure 4.9**. Graphene quantum dots possess a transparent, wrinkled paper-like structure (**Fig. 4.9 A-C**) (Jadhav *et al.*, 2018; Koopi and Buazar, 2018; Shahedi Asl, Nayebi and Shokouhimehr, 2018). The incorporation of metals shows dark spots on the transparent GQD structures, **Figure**

4.9 A&B. **Figure 4.9C** shows stacks of graphene layers as was already anticipated in **Figure 4.4** above.

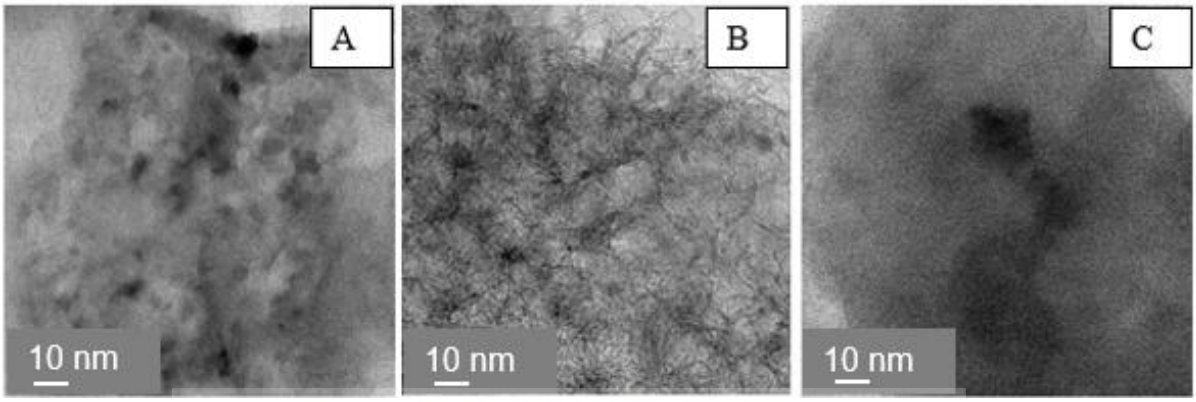

Figure 4.9: TEM micrographs of A. GQD:Au, B. GQD:Al and C. GQD:G nanocomposites

The calculated particle sizes of the nanocomposites from image j are 3 ± 0.5 nm and 2 ± 0.3 nm for GQD:Au and GQD:Al, respectively. The TEM micrographs in **Fig. 4.9** show a uniform surface, which might be an indication of well-dispersed and homogeneously mixed nanocomposites. A homogenously mixed solution is mostly preferred in this study for improved contact between the metals and GQDs for the Schottky junction.

4.3.3 Optical properties of the active layer

4.3.3.1 UV-vis spectroscopy

The optical properties of the metal-semiconductor redox couples were investigated using UV-vis spectroscopy and the results are presented in **Figure 4.10**. **Figure 4.10 A** shows the UV-vis spectra of the prepared donor (graphene quantum dots) and acceptor (Al, Au & graphene) materials. The UV-vis spectrum of the mixed GQD donor materials shows a broad absorption band from 300 nm to around 800 nm, signifying its high absorption potential in the visible region. In detail, the UV-vis

spectrum of GQD shows π-π* transitions around 350 nm that occur due to the aromatic conjugated benzene rings in the structure. Those observed at 490 nm are due to the n-π* transitions from the excited oxygenated carbon atoms in the quantum dots structures. However, the UV-vis spectra of the acceptor materials show absorption at lower wavelength regions. In detail, the UV-vis spectrum of graphene shows a wide absorption from 300 nm to 790 nm, probably due to the π-π* transitions from the aromatic benzene rings. The spectrum of Aluminium shows a sharp absorption peak from 300 nm to 350 nm, concurrent with literature reports, concurrent with the results obtained by Piriyawong *et al.* (2012) (Piriyawong *et al.*, 2012). That of gold nanoparticles shows a broad absorption peak at a region of 300 nm to 500 nm. Literature reports strongly show that the position of the UV-vis absorption peak for gold nanoparticles is strongly dependent on the particle size (Li *et al.*, 2018; Tang *et al.*, 2018).

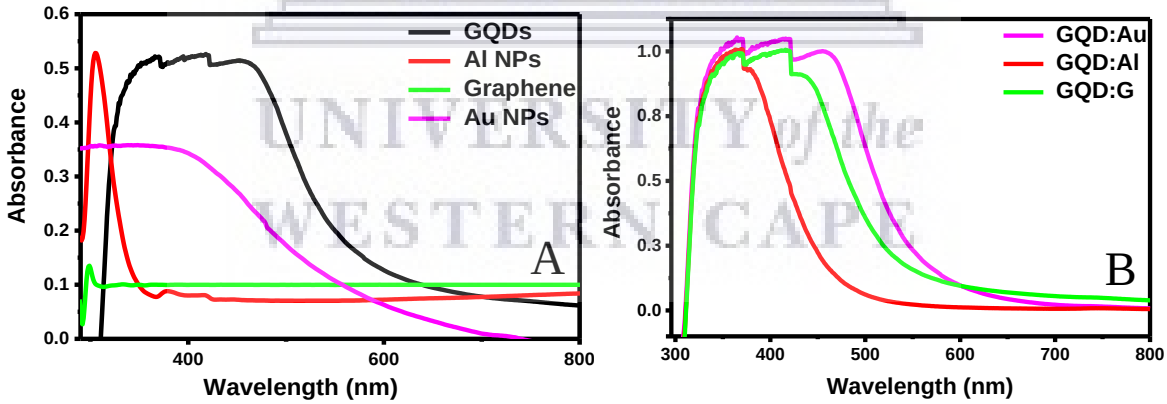

Figure 4.10: UV-vis spectra of the A. donor and acceptor materials together with the B. active layer.

Introduction of the acceptor nanomaterials on GQD shows preservation of absorption in the visible region, **Figure 4.10B**. GQD:Al shows the lowest absorbance at 300 nm to 500 nm, that of GQD:G shows absorbance at 300 nm to 600 nm and lastly that of GQD:Au shows absorption at 300 nm to 700 nm. From the

absorbance spectra presented in **Figure 4.10B**., it may be seen that both the π-π* and n-π* are preserved. This implies that the GQD structure was preserved during preparation of the nanocomposites. To evaluate the donor and acceptor properties, quenching studies were also conducted on the nanocomposites by varying the concentration of the donor.

4.3.3.2 Photoluminescence spectroscopy

To further explore the structural change in graphene quantum dot by adding acceptor materials, quenching studies were investigated using fluorescence spectroscopy in the presence of different concentrations of respective metal acceptor materials following a process presented in **Figure 4.11**.

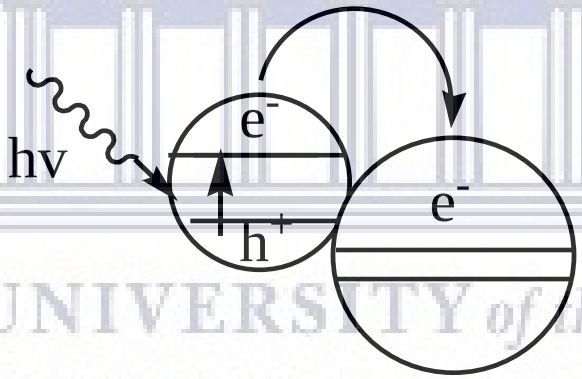

Figure 4.11: Representation of fluorescence quenching by metallic nanoparticles

The electrons in the conduction band are excited to the valence band upon illumination with light, and thereafter transferred into the valence band of the acceptor material depending on the proximity of the charge-transfer complex. This has been theoretically predicted to result in a decrease in the wavelength of fluorescence (Bozkurt and Gul, 2019). It can be seen in **Figure 4.12**, the increase in the concentration of the acceptor results in a decrease in the fluorescence

wavelength. A blue-shift is observed upon addition of the graphene and aluminium accepting molecules as opposed to when gold is added to graphene quantum dots.

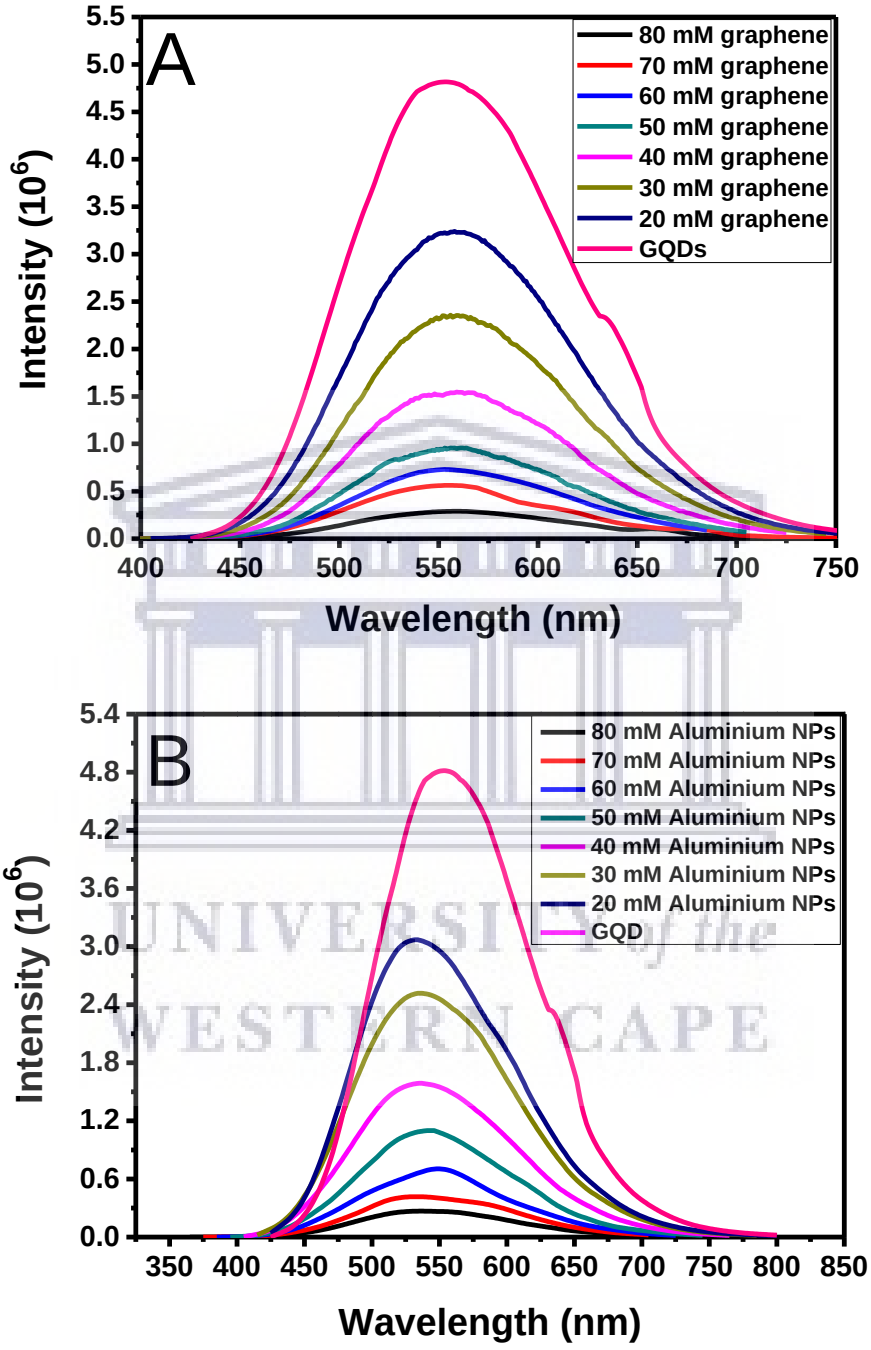

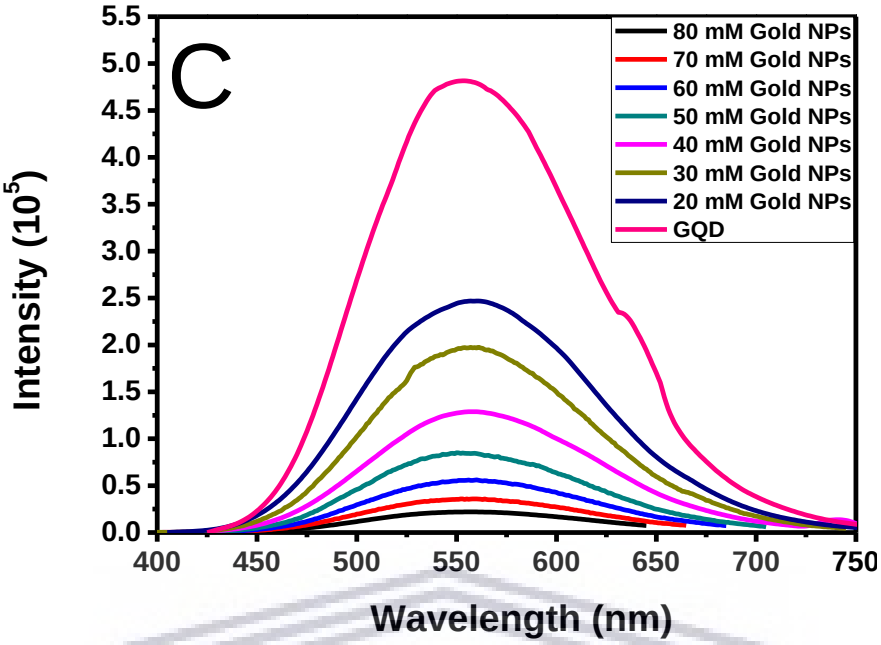

Figure 4.12: Photoluminescence quenching of graphene quantum dots by respective metals.

The interaction between donor and acceptor is of utmost interest in solar cell devices, therefore, fluorescence spectroscopy was used to evaluate the florescence of quenching of the graphene quantum dots in the presence of acceptor metal nanoparticles. **Figure 4.12** illustrates the difference in quenching behaviour of graphene, Aluminium and gold metal nanoparticles on graphene quantum dots. With increasing amounts of metal nanoparticles to a solution of graphene quantum dots, strong attenuation of the fluorescence intensity is observed. Concurrently, emission maxima and shape of the emission spectra of GQD remained the same. The Stern-Volmer (SV) plots, shown in **Figs 4.13**, were created by attenuating the fluorescence emission spectra at different metal nanoparticles concentrations to quantify the quenching.

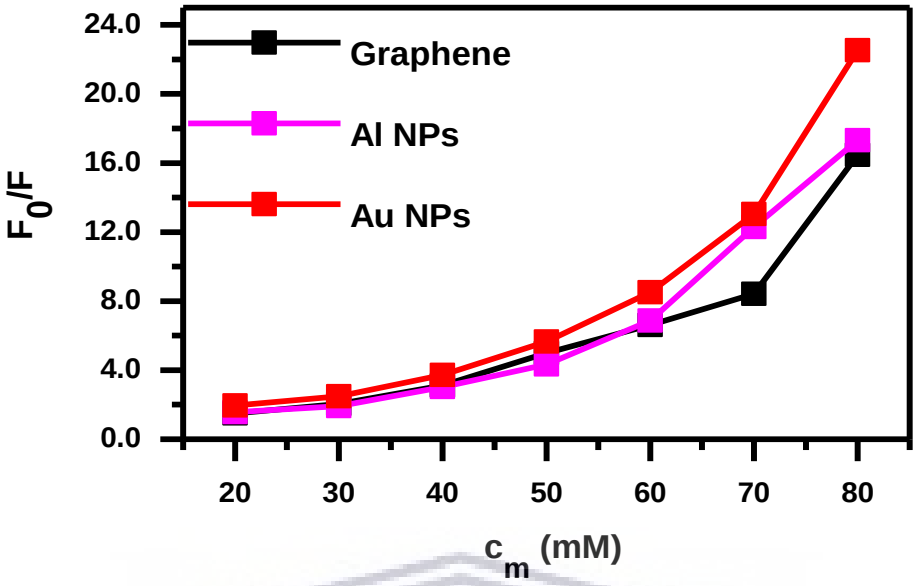

Figure 4.13: Stern-Volmer plot for exploring the quenching mechanism of graphene quantum dots by respective metals.

Any process that decreases the fluorescence intensity of a given substance is referred to as fluorescence quenching. Fluorescence quenching may be induced by a variety of processes such as complex formation, collisional quenching, excited state reactions and energy transfer reactions. Collisional quenching results from collisional encounters that result in binding between the fluorophore and quencher in the excited state. Static quenching may also occur due to complex formation between the quencher and the fluorophore, however, the formed complex is non-fluorescent. In either event, the fluorophore and the quencher must be in contact. The quenching data were analysed using Stern-Volmer equation:

$$\frac{F_0}{F} = 1 + Kc_m \qquad [4.1]$$

…where, F_0 and F denote the fluorescence intensity of the graphene quantum dots without and with metal nanoparticles, respectively, and c_m is the concentration of the added metal ion quencher in milli Molar, K is the Stern-Volmer constant (Ciotta,

Prosposito and Pizzoferrato, 2019). When the Stern-Volmer plot results in a linear graph, it indicates that only one type of quenching (i.e., dynamic) occurs. When the fluorophore is quenched by both mechanisms, collisions and complex formation, an upward curvature is observed as seen in **Figure 4.13.** The plot deviated significantly from linearity, which is indicative of interactions occurring between the graphene quantum dots and metal ions when the quantum dot is in its first excited single state (dynamic quenching) and in its ground electronic state (static quenching). In a situation whereby both mechanisms occur concurrently, it is more convenient to use the modified Stern-Volmer equation:

$$\frac{F_0}{F} = (1 + K_s\, c_m)\,(1 + K_d\, c_m) \qquad [4.2]$$

where K_s and K_d represents the static and dynamic Stern-Volmer constants. The equation is second order in quencher concentration, which accounts for the upward curvature observed when both static and dynamic quenching occur for the same fluorophore. Expansion/multiplication of the terms in parenthesis yields:

$$\frac{F_0}{F} = 1 + (K_d + K_s)c_m + K_d K_s c_m^2 = 1 + K_{app} c_m \qquad [4.3]$$

where $K_{app} = (K_d + K_s) + K_d K_s c_m = (F_0/F - 1)/c_m$ is the apparent quenching constant. The plot of K_{app} with c_m yields a straight line with a slope of 2.5e-3 M^{-1}, 3.5e-3 M^{-1} and 3.0e-3 M^{-1} for graphene, gold and aluminium quenchers. If the graphene quantum dots experienced only one type of quenching, the plot would yield a straight line parallel to the x-axis (Ren *et al.*, 2018; Xu *et al.*, 2018).

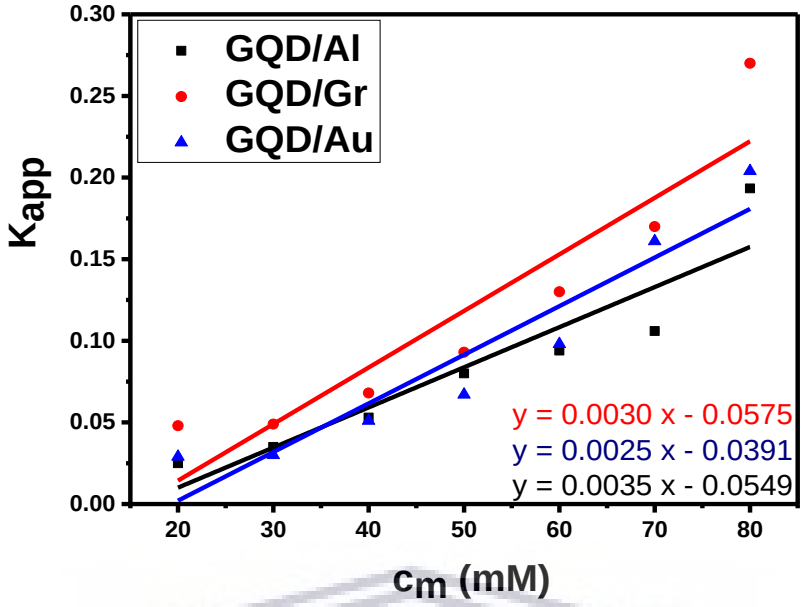

Figure 4.14: Variation of the apparent quenching constant, K_{app} with the quencher concentration.

From the relative fluorescence values, the fraction of the fluorescence that has been quenched, Q, is obtained as;

$$Q = \frac{(F_0 - F)}{100} \quad [4.4]$$

With this parameter, a new representation can be made by plotting Q versus [m]/[GQD], where [GQD] is the concentration of the graphene quantum dot fluorophore. **Figure 4.15** shows this plot, and from that, the limit of quenching concentration can be determined.

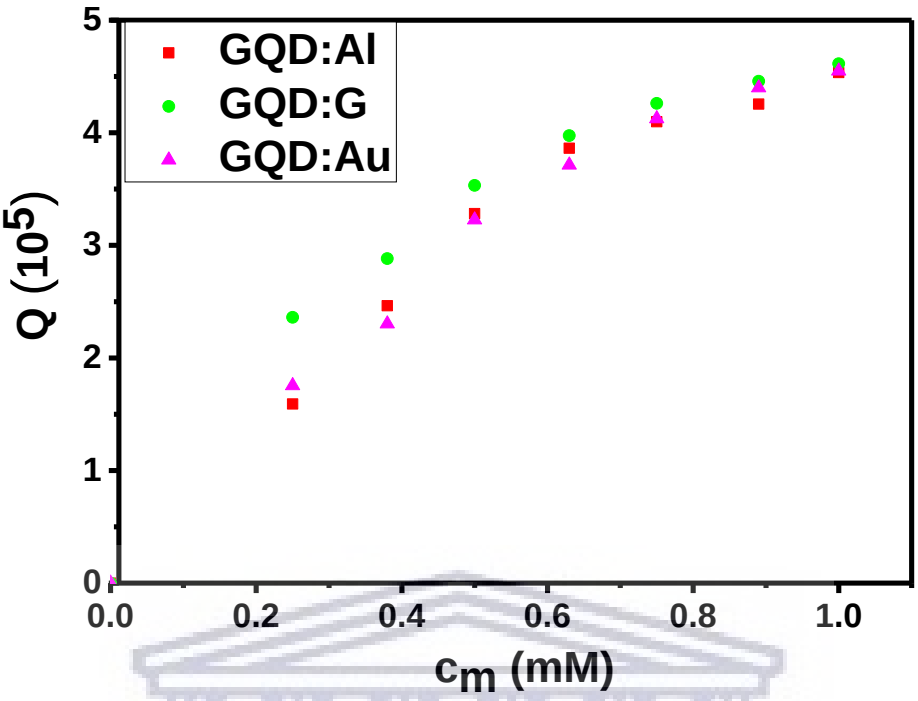

Figure 4.15: Plot of fractional quenching, Q, in front of the relationship between the concentration of metal ions and graphene quantum dots.

A c_m/[GQD] value of 0.89 was the largest relationship between donor and acceptor that produced the maximal quenching and is equivalent to metal ion concentration of 70 Mm for all samples. Thereafter, the concentration of free metal ions ($[m]_f$) not bound to graphene quantum dots was calculated as:

$$c_m f = c_m - Q[GQD] \qquad [4.5]$$

Where [m] is the concentration of the metal ions in the samples and [GQD] is the concentration of the graphene quantum dots (and its value always 80 Mm), Q can be obtained from [4.4]. **Figure 4.16** shows a plot of reciprocal of the fractional quenching versus the reciprocal of the free ligand concentration. In the plot, the x-intercept is -1/Kd. Kd being the dissociation constant of the GQD-quencher complex. The obtained dissociation constant was found to be; 382.4 M, 11465.3 M and 988.1 M for Al, Gr and Au quenchers, respectively.

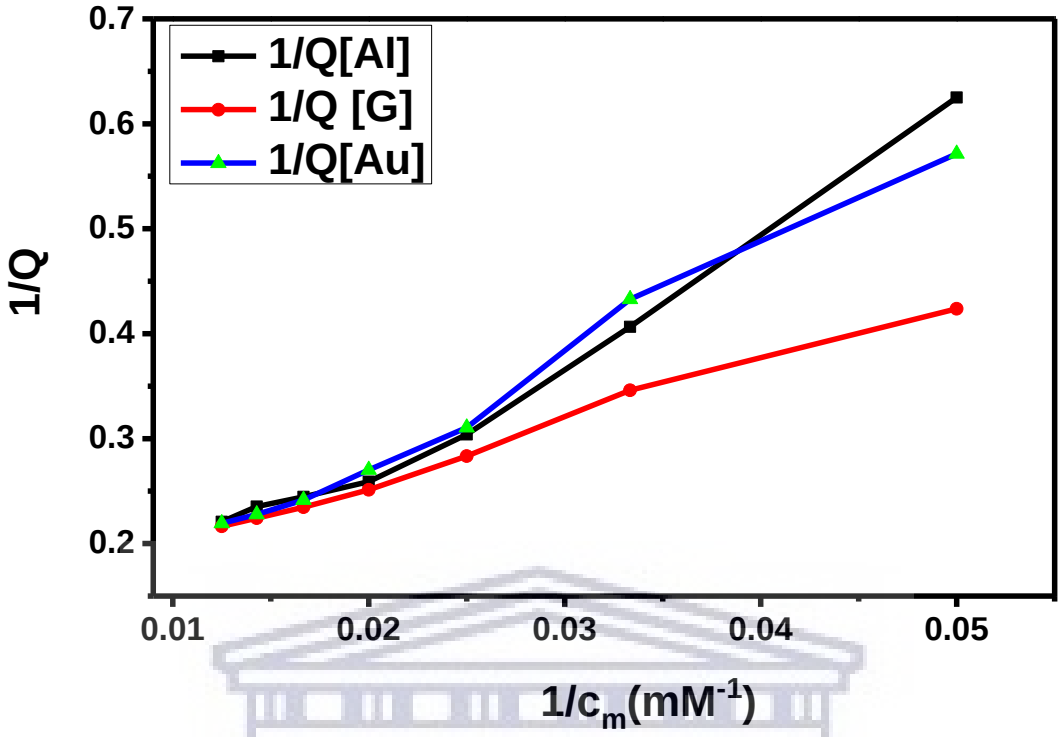

Figure 4.16: Reciprocal of fractional quenching, Q, against the reciprocal of the concentration of non-bound metal ions (quenchers).

To get a deeper understanding of the binding sites, the expression below was derived:

$$\frac{\mathrm{Q}}{\mathrm{c_{mf}}} = \frac{\mathrm{n}}{\mathrm{K_d}} - \frac{Q}{\mathrm{K_d}} \qquad [4.6]$$

A plot of Q/c_{mf} against Q is known as a Scatchard plot (**Figure 4.17**).

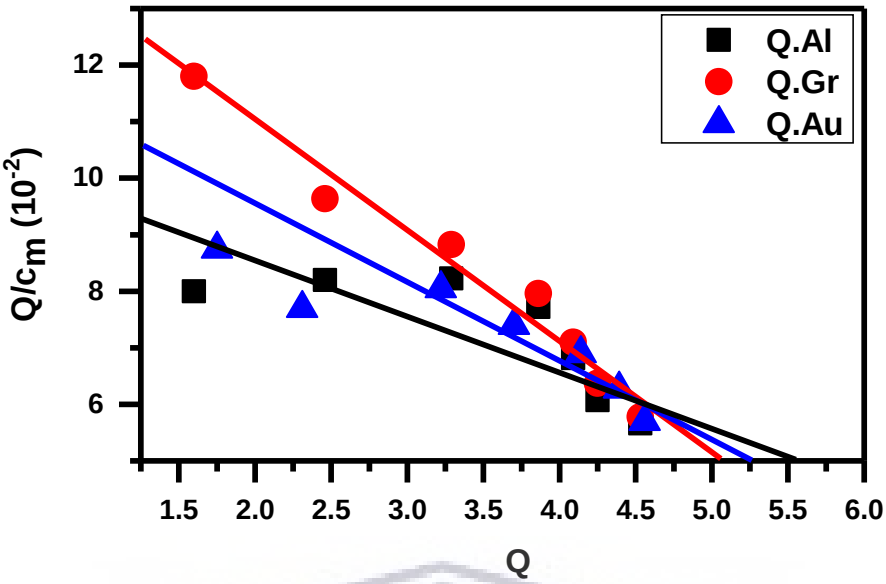

Figure 4.17: Scatchard plot for identical, independent binding sites of metal ions to GQDs.

The data gives a linear plot with an ordinate intercept of n/Kd, abscissa intercept of n and a slope of -1/Kd. From this plot, the two parameters that characterize the binding equilibria can be obtained. From these results, the estimated value of n is 5.06, 5.54 and 5.24 for GQD:G, GQD:Al and GQD:Au, respectively; and thus GQDs have 5 binding sites to metal ions.

4.4 Electrochemical studies

4.4.1 Cyclic voltammetry

The electrochemical behaviour of the electrodes modified with the redox couple (i.e., active layer; GQD:Al, GQD:Au and GQD:G) was evaluated using cyclic voltammetry in 0.1 M Butylammonium perchlorate as a supporting electrolyte at pH 7, scanning a potential window of -0.9 V to 0.7 V. It is observed from **Figure 4.18** that the redox couples show enhanced and roughly symmetric redox peaks from the GQD molecules on the electrode surface as compared to the pristine materials.(Guin *et al.*, 2018; Dehgan-Reyhan and Najafi, 2019) The enhancement of current peaks on GQD:G signifies the high electron flow on the redox couple as compared to GQD:Al and GQD:Au. However, all redox couples show 2-electron oxidation and reduction peaks indicating that the electron communication between the couples is reversible and suggesting an ambipolar electron diffusion.

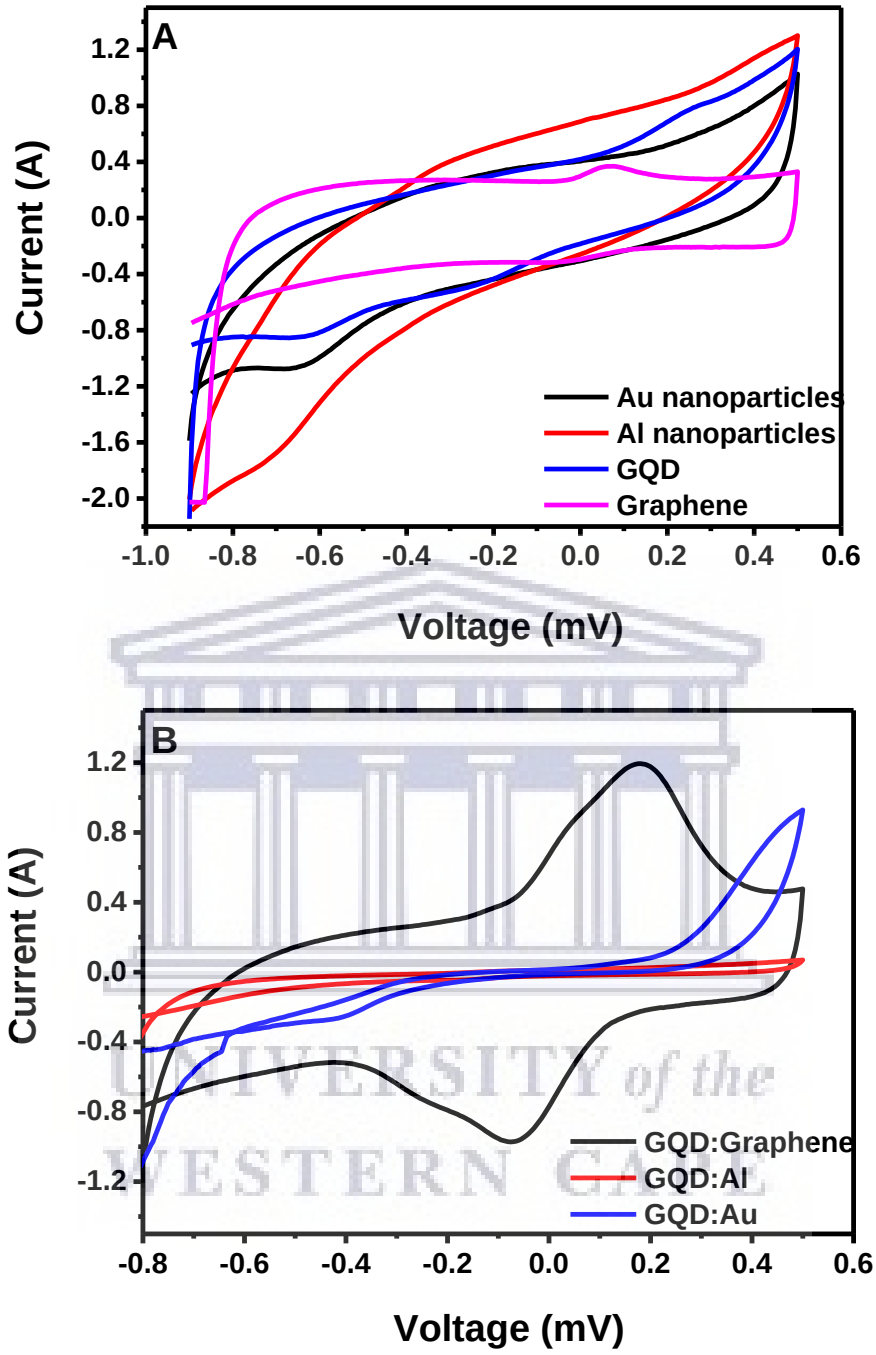

Figure 4.18: Cyclic voltammograms of GQD:Au, GQD:Al and GQD:G nanocomposites.

The highest occupied molecular orbital (HOMO) and the lowest unoccupied molecular orbital (LUMO) of the redox couples were evaluated using the electrochemical results from the CV, thus the band gap was acquired as well. **Figure**

4.19 shows the band energies of the redox couples and the structure of the Schottky junction formed during fabrication of the photovoltaic device.

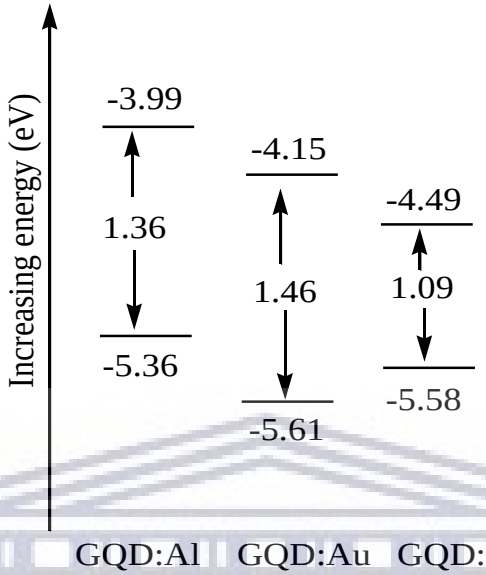

Figure 4.19: Energy band diagram of the prepared semiconducting donor and accepting metal nanoparticles.

Table 4.1: The electrochemical parameters of the redox couples used to prepare the Schottky junction.

Sample	Electron affinity	Work function	Conduction band (eV)	Valence band (eV)	Electrochemical band gap (eV)	Optical band gap (eV)
GQD:Al	0.43	4.08	-3.99	-5.36	1.36	1.43
GQD:Au	2.31	5.10	-4.15	-5.61	1.46	1.50
GQD:G			-4.99	-5.58	1.09	1.30

4.4.2 Electrochemical Impendence spectroscopy (EIS)

Electrochemical impedance spectroscopy (EIS) is a useful method for examining the properties of electrode surfaces while providing useful information on the impedance of the conductive interface. The semi-circular part represents the electron-transfer-limited process with a diameter equivalent to the electron transfer resistance (Ret) (Li *et al.*, 2018; Senthilkumar *et al.*, 2018). The smaller semi-circle shows high electron resistance, while the larger ones signify a reduced electron flow resistance. This is substantiated by the quenching that was observed between the GQD semiconducting nanoparticles and the respective metal nanocrystals. There is a resistance in the electron flow due to the quenching that occurs between the GQDs and the metal nanoparticles.

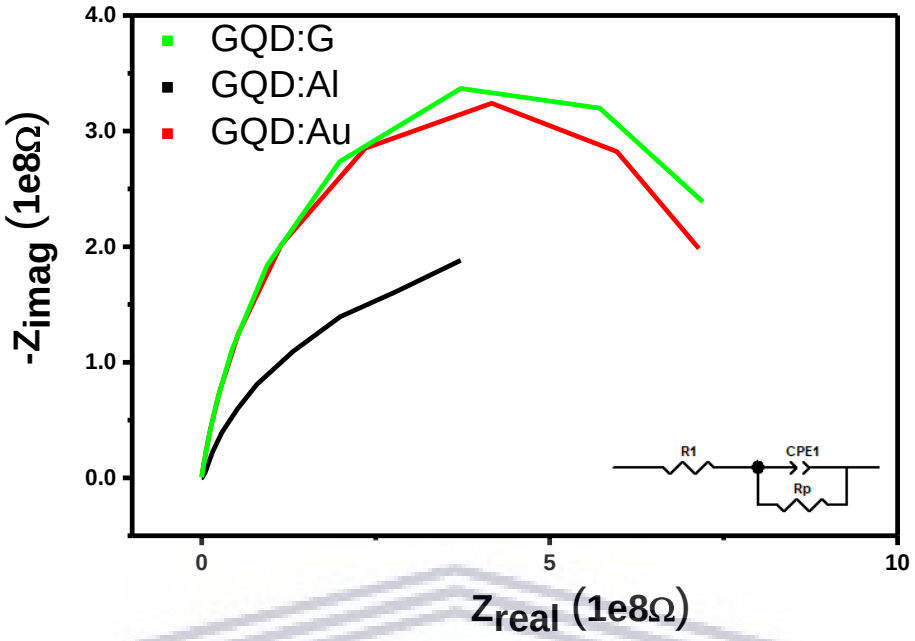

Figure 4.20: Impendence spectroscopy results of GQD:Au, GQD:Al and GQD:G nanocomposites.

4.5 Conclusive summary

The GQD:Al, GQD:G and GQD:Au nanocomposites/charge-transfer complexes were successfully prepared using physical mixing techniques. The interaction of the metal with semiconductors was supported by the appearance of Al-C, Au-OH and C=C functional groups on FTIR. The XRD crystallographic analysis of the nanocomposites showed a retained 002 RXD plane from the graphitic structure of graphene quantum dots (GQDs). Introduction of the metal nanoparticles to the GQD structure shows a shift in the cubic structure from a primitive cubic to a face-centred cubic signifying interaction of the materials. Morphological studies of the materials showed appearance of metal nanoparticles embedded on GQD structures. When the charge-transfer properties of the materials were studies through quenching of the GQD at different metal ion concentrations, it was found that the complexes followed both the static and dynamic quenching. However, there is good electron flow between the donor (GQD) and the acceptor (metal ions). This is confirmed by the low resistance observed on the Nyquist plots.

References

Anjana, P. M., Bindhu, M. R. and Rakhi, R. B. (2019) 'Green synthesized gold nanoparticle dispersed porous carbon composites for electrochemical energy storage', *Materials Science for Energy Technologies*, 2, pp. 389–395.

Bozkurt, E. and Gul, H. I. (2019) 'Fluorescence quenching of novel pyrazoline derivative with aniline in different solvents', *Journal of Photochemistry and Photobiology A: Chemistry*, 383, p. 111996.

Büchele, P. *et al.* (2015) 'Space charge region effects in bidirectional illuminated P3HT:PCBM bulk heterojunction photodetectors', *Organic Electronics: physics, materials, applications*, 22, pp. 29–34.

Bandi, S. *et al.* (2019) 'Graphene from discharged dry cell battery electrodes', *Journal of Hazardous Materials*, 366, pp. 358–369.

Baruah, D. *et al.* (2018) 'Biogenic synthesis of gold nanoparticles and their application in photocatalytic degradation of toxic dyes', *Journal of Photochemistry and Photobiology B: Biology*, 186, pp. 51–58.

Chen, L. *et al.* (2018) 'Numerical simulation of planar BaSi2 based Schottky junction solar cells toward high efficiency', *Solid-State Electronics*, 149, pp. 46–51.

Ciotta, E., Prosposito, P. and Pizzoferrato, R. (2019) 'Positive curvature in Stern-Volmer plot described by a generalized model for static quenching', *Journal of Luminescence*, 206, pp. 518–522.

Debehets, J. *et al.* (2018) 'Detecting Fermi-level shifts by Auger electron spectroscopy in Si and GaAs', *Applied Surface Science*, 440, pp. 386–395.

Drab, M. and Kralj-Iglič, V. (2019) 'Electric double layer of electrons: Attraction between two like-charged surfaces induced by Fermi–Dirac statistics', *Physics*

Letters, Section A: General, Atomic and Solid State Physics, 383, pp. 358–365.

Dehgan-Reyhan, S. and Najafi, M. (2019) 'Defective mesoporous carbon ceramic electrode modified graphene quantum dots as a novel surface-renewable electrode: The application to determination of zolpidem', *Journal of Electroanalytical Chemistry*, 832, pp. 241–246.

Derkacs, D. *et al.* (2006) 'Improved performance of amorphous silicon solar cells via scattering from surface plasmon polaritons in nearby metallic nanoparticles', *Applied Physics Letters*, 89, pp. 1–4.

Garca-Santamara, F. *et al.* (2009) 'Suppressed auger recombination in "Giant" nanocrystals boosts optical gain performance', *Nano Letters*, 9, pp. 3482–3488.

Guin, S. K. *et al.* (2018) 'Exploring the excellent photophysical and electrochemical properties of graphene quantum dots for complementary sensing of uranium', *Sensors and Actuators B: Chemical*, 272, pp. 559–573.

Hagfeldt, A. and Graetzel, M. (1995) 'Light-Induced Redox Reactions in Nanocrystalline Systems', *Chemical Reviews*, 95, pp. 49–68.

Jadhav, K. *et al.* (2018) 'Phytosynthesis of gold nanoparticles: Characterization, biocompatibility, and evaluation of its osteoinductive potential for application in implant dentistry', *Materials Science and Engineering: C*, 93, pp. 664–670.

Jakob, M., Levanon, H. and Kamat, P. V. (2003) 'Charge distribution between UV-irradiated TiO2 and gold nanoparticles: Determination of shift in the Fermi-level', *Nano Letters*, 3, pp. 353–358.

Jin, J. *et al.* (2018) 'Stable GQD@PANi nanocomposites based on benzenoid structure for enhanced specific capacitance', *International Journal of Hydrogen Energy*, 43, pp. 8426–8439.

Katz E, W. I. and Wang, J. (2004) 'Electroanalytical and bioelectroanalytical systems

based on metal and semiconductor nanoparticles', *Electroanalysis*, 16, pp. 19–44.

Kazantsev, S. O. *et al.* (2018) 'Preparation of aluminum hydroxide and oxide nanostructures with controllable morphology by wet oxidation of AlN/Al nanoparticles', *Materials Research Bulletin*, 104, pp. 97–103.

Khan, W. *et al.* (2018) 'Synthesis and magnetic dispersibility of magnetite decorated reduced graphene oxide', *Nano-Structures & Nano-Objects*, 16, pp. 180–184.

Kim, G. H. *et al.* (2014) 'Inverted Colloidal Quantum Dot Solar Cells', *Advanced Materials*, 26, p. 3321.

Koopi, H. and Buazar, F. (2018) 'A novel one-pot biosynthesis of pure alpha aluminum oxide nanoparticles using the macroalgae Sargassum ilicifolium: A green marine approach', *Ceramics International*, 44(8), pp. 8940–8945.

Kumar, B. *et al.* (2018) 'Utilization of Persea americana (Avocado) oil for the synthesis of gold nanoparticles in sunlight and evaluation of antioxidant and photocatalytic activities', *Environmental Nanotechnology, Monitoring & Management*, 10, pp. 231–237.

Laguna, H. G. and Amador-Bedolla, C. (2019) 'Density (de)localization and statistical correlation in the Van der Waals interactions and the chemical bond between two hydrogens', *Physica A: Statistical Mechanics and its Applications*, 527, pp. 121324.

Li, Y. *et al.* (2018) 'A sensitive and rapid UV–vis spectrophotometry for organophosphorus pesticides detection based on Ytterbium (Yb3+) functionalized gold nanoparticle', *Chinese Chemical Letters*, 29, pp. 1845–1848.

Li, Z. *et al.* (2018) 'Exceptional supercapacitor performance from optimized oxidation of graphene-oxide', *Energy Storage Materials, 17*, pp. 12-21.

Liu, Y., Stradins, P. and Wei, S.-H. (2016) 'Van der Waals metal-semiconductor

junction: Weak Fermi-level pinning enables effective tuning of Schottky barrier.', *Science advances*, 2, pp. 1600069.

Mesallam, M. *et al.* (2018) 'Graphene and magnesiated graphene as electrodes for magnesium ion batteries', *Materials Letters*, 232, pp. 103–106.

Neetika *et al.* (2019) 'Influence of barrier inhomogeneities on transport properties of Pt/MoS2 Schottky barrier junction', *Journal of Alloys and Compounds*, 797, pp. 582–588.

Ni, Y. P. *et al.* (2019) 'Semi-aromatic copolyesters with high strength and fire safety via hydrogen bonds and π-π stacking', *Chemical Engineering Journal*, 374, pp. 694–705.

Piriyawong, V. *et al.* (2012) 'Preparation and characterization of alumina nanoparticles in deionized water using laser ablation technique', *Journal of Nanomaterials*, 2012, pp. 1–6.

Ranea, V. A., Dammig Quiña, P. L. and Moreno Yalet, N. (2019) 'A DFT+u study, including the van der waals interaction, on the adsorption of XO2 molecules on the v2o5(001) surface (x= S, N, O, C)', *Surface Science*, 679, pp. 110–116.

Ren, X. *et al.* (2018) 'Enhanced heterogeneous activation of peroxydisulfate by S, N co-doped graphene via controlling S, N functionalization for the catalytic decolorization of dyes in water', *Chemosphere*, 210, pp. 120–128.

Senthilkumar, E. *et al.* (2018) 'Synthesis of nanoporous graphene and their electrochemical performance in a symmetric supercapacitor', *Applied Surface Science*, 460, pp. 17–24.

Shahedi Asl, M., Nayebi, B. and Shokouhimehr, M. (2018) 'TEM characterization of spark plasma sintered ZrB2–SiC–graphene nanocomposite', *Ceramics International*, 44, pp. 15269–15273.

Subramanian, V., Wolf, E. E. and Kamat, P. V. (2004) 'Catalysis with TiO2/Gold Nanocomposites. Effect of Metal Particle Size on the Fermi-level Equilibration', *Journal of the American Chemical Society*, 126, pp. 4943–4950.

Sunderam, V. *et al.* (2018) 'In-vitro antimicrobial and anticancer properties of green synthesized gold nanoparticles using Anacardium occidentale leaves extract', *Saudi Journal of Biological Sciences*, 26, pp. 455-459.

Tang, J. *et al.* (2018) 'Calculation extinction cross sections and molar attenuation coefficient of small gold nanoparticles and experimental observation of their UV–vis spectral properties', *Spectrochimica Acta - Part A: Molecular and Biomolecular Spectroscopy*, 191, pp. 513–520.

Teo, L. P., Akub, M. K. and Buraidah, M. H. (2019) 'Boosting the efficiency of dye-sensitized TiO2 solar cells using plasmonic gold nanoparticles', *Materials Today: Proceedings*, 17, pp. 465–471.

Vedhanayagam, M., Nair, B. U. and Sreeram, K. J. (2019) 'Effect of functionalized gold nanoparticle on collagen stabilization for tissue engineering application', *International Journal of Biological Macromolecules*, 123, pp. 1211–1220.

Wasson, J. R. (2009) 'Introduction to molecular orbital theory (Liberles, Arno)', *Journal of Chemical Education*, 44, p. 117.

Xu, A. *et al.* (2018) 'Selective supramolecular interaction of ethylenediamine functionalized graphene quantum dots: Ultra-sensitive photoluminescence detection for nickel ion in vitro', *Synthetic Metals*, 244, pp. 106–112.

Zeng, W., Jelliss, P. A. and Buckner, S. W. (2018) 'Synthesis and hydrogen production kinetics of temperature-responsive aluminum-poly(N-isopropylacrylamide) core-shell nanoparticles', *Materials Chemistry and Physics*, 220, pp. 233–239.

Zhang, J. *et al.* (2018) 'Mechanical and electronic properties of graphene nanomesh heterojunctions', *Computational Materials Science*, 153, pp. 64–72.

CHAPTER 5

Summary

Compared to their traditional counterparts (p-n junction solar cells), Schottky junction solar cells (SJSC) have been attracting researcher's attention since the 1970's due to their easy fabrication processes. Their fabrication processes are simple since they do not require high temperature-diffusion processes. They are therefore considered cheap as compared to their traditional counterparts. SJCS cells offer improved electrical and optical properties which promise to drive them to commercialization (PCE ≥ 15%). This chapter advances the field of Schottky junction solar cells by studying the photophysics and electrochemistry of the devices to understand the charge current, which is related to efficiency. The splendid acceptor material in the presence of three different metal nanoparticles towards Schottky junction solar cell application are applied and studied. The equivalent circuit Bio Logic VMP300 model developed for Schottky junction photovoltaic cells has shown to work well to describe the behaviour of organic devices and parameterize their current-voltage characteristics with five parameters. The solar cell properties are studied using electrochemical cells of different electrodes and an electrolyte. The fabricated devices are also evaluated for their solar to energy conversion efficiencies.

Fabrication and testing of the rainbow inverted Schottky junction solar cells

Abstract

The depletion of fossil fuels, global warming, population growth and industrial developments demands the world to migrate to renewable energy sources. Solar energy stands superior compared to other renewable energy sources due to the geographical location of this study. The materials prepared in Chapter 4 were used in the active layer for fabrication of the device in this study. Electrochemistry is predominantly applied in conversion aspects, synthesis, chemical analysis and energy storage. Different donor (GQDs) to acceptor (metals) ratios of 1:3, 1:1, 1:6 and 3:1 were evaluated for their electrochemical efficiencies and the 1:3 was found to be optimal for the preparation of the active layer during fabrication. Solar cell device fabrication and testing attracts extensive attention from scientists worldwide with the hopes of improving the materials already in the market and decreasing the cost of solar cells. This chapter will focus on the development of photovoltaic cells and evaluate their efficiencies. The GQD-Aluminium (GQD:Al), GQD-Gold (GQD:Au) and GQD-graphene (GQD:G) nanocomposites were used in the active layer to generate the Schottky junction solar cells. This chapter seeks to study the effect of metallic nanoparticles on the performance of Schottky junction solar cells. When these different types of metals (Aluminium, gold, and graphene) were used in the active layer, significant improvement in the solar to energy conversion of efficiency of the solar cells was observed when gold metal was used. According to the experimental results, the introduction of gold metal nanoparticles into the

nanocomposite layer could prove beneficial for improvement of the charge transport processes in the preparation of photovoltaic cell.

5.1 Introduction

Since discovery, researchers have been working on improving the efficiency of Schottky junction solar cells from 0 to 40% power conversion efficiency as promised by theoretical studies (Chen *et al.*, 2018; Suhail *et al.*, 2018). A lot of focus has been recently shifted on graphene/silicon based Schottky junction solar cells due to the attractive properties offered by graphene and the fact that silicon has already made it to commercialisation (Liu and Kortshagen, 2010; Larsen *et al.*, 2015; Shin *et al.*, 2017). Silicon is currently the principal material used for fabrication of commercial solar cells due to its compatibility with conventional semiconductor device processes and its low cost. However, the high refractive index (~3.5) of silicon prevents electron-hole pairs from being efficiently generated, and this limits the PCE of Si solar cells (Wu *et al.*, 2018; Jaglarz, Jurzecka-Szymacha and Kluska, 2019).

Graphene is a very fascinating two-dimensional material that is promising for applications in novel optoelectronic devices and post-CMOS (Lin *et al.*, 2017; Xie *et al.*, 2018). Graphene-semiconductor Schottky junctions have been intensively studied for their possible applications in barristers, photodetectors, solar cells and chemical/biological sensors. Nanostructured Si stands superior for the graphene-based Schottky junctions due to its compatibility with the existing Si CMOS processes as compared to other semiconducting materials.

Graphene is a two-dimensional honeycomb carbon structure with very good electrical and thermal conductivities, strong chemical stability and high mechanical strength (Tu *et al.*, 2019; Rezaei, Kamali and Kamali, 2020). It can be prepared in

different forms, such as sheets, nanoribbons, and graphene quantum dots (GQDs) using various methods (Tiwari *et al.*, 2016; Nair *et al.*, 2018; Potsi *et al.*, 2019; Wang *et al.*, 2019). The size and shape determine the properties and applications of graphene. For example, graphene sheets do not have photoluminescence properties due to their metallic character, whereas graphene nanoribbons and GQDs have photoluminescence properties (Liu *et al.*, 2011; Bayat and Saievar-Iranizad, 2017). While GQDs are finding applications in biology as biomarkers, graphene sheets are being used in optoelectronic device fabrication. Graphene sheets are obtained by exfoliating graphite using various methods, which include the Hummer's and Bordie's methods (Arshad *et al.*, 2019; Zhai *et al.*, 2019). The chemical vapor deposition method is also used to prepare pristine graphene sheets. On the other hand, GQDs may obtained by top-down and bottom-up methods.

The convergence of the valence band maximum and conduction band minimum at the Dirac point makes graphene to be a zero-band-gap material due to (Javaid *et al.*, 2019). Its photo-generated electron-hole pairs undergo non-radiative relaxation processes through the continuum band states towards the band edge states, and therefore, photoluminescence is not possible. If a graphene sheet has to be used as an active layer in solar cells, just like semiconducting materials, bandgap must be introduced (Cao *et al.*, 2016; Li *et al.*, 2018). The energy levels (molecular-like energy levels) of graphene sheets can be discretized by producing isolated domains of sp^2 islands on the surface of graphene sheets. This will allow photo-excited electron–hole pairs to undergo radiative recombination through those discrete energy levels and result in an essential emission. This essential emission is an indication that the band gap has been opened in the graphene sheet sample. GQDs can be used to fabricate solar cells directly or employed as photosensitizers

interfaced with metal oxides and giving rise to visible-light photocatalytic and photovoltaic devices (Zhang *et al.*, 2017; Kusuma *et al.*, 2018). Several factors make GQDs preferable to graphene and nanotubes. GQDs have discrete electronic levels, allowing for hot electron injection and efficient charge separation as compared to metallic graphene. Using pump-probe optical measurements, Zhu and co-workers reported sub-15 fs electron injection from GQDs to TiO_2 (Williams *et al.*, 2013). The electron transfer from GQDs was found to be faster than from graphene. The electron transfer studies were conducted in Chapter 4, and this chapter focusses on the fabrication of Schottky junction solar cells using GQD/metal in the active layer.

5.2 Methodology

The prepared graphene quantum dots (GQDs) of different band gaps (1.5 mg each, amounting to 12 mg) were dissolved in 0.5 mL of dichlorobenzene and heated at 200 °C for 2 min. Consequently, 2.4 mg of metal (Aluminium, Al and Gold, Au) was dissolved in 0.1 mL dichlorobenzene and heated at 200 °C for 2 min. This solution was stirred for 5min while heating at 200 °C to form a homogenous mixture. Different ratios of the GQD:Al, GQD:Au and GQD:G were prepared as (1:1, 1:3, 1:6 and 3:1) for optimisation, and the optimal ratio was found to be 1:3 from electrochemical efficiencies. Therefore, this chapter focusses on the comparative study of GQD:Al, GQD:Au and GQD:G of the same ratio (1:3) for the active layer and the overall performances of the photovoltaic devices.

Cleaning of the substrate was conducted by first identifying the ITO coated (anode coated) side by evaluating the conducting side on the glass, using an ohm-meter. The indium tin-oxide (ITO, from Ossila with sheet resistance ~ 10 Ohm/sq)

substrates were successively cleaned by sonication in alumina solution for 10 min, followed by rinsing twice in boiling water. This step is followed by sonication in propanol for 10 min and rinsed twice in boiling water again, and dried using argon gas.

Device fabrication is conducted by spin-coating PDOT:PSS (electron transporting layer) at a speed of 5000 rpm for 30s to form a thin layer on an ITO coated glass slide. Thereafter, the substrate sides (patterned) were cleaned using cotton and the water solvent, followed by annealing at 150 °C for 5min. This step is followed by spin-coating the active layer (GQD:Al, GQD:Au and GQD:G) at a speed of 1500 rpm for 20s. The spin-coated substrate is then cleaned on the sides using cotton and chlorobenzene solvent, then annealed at 120 °C for 5 min. Cathode deposition (Al metal) is the final step of device fabrication, using sputtering method and then covered with a glass on top. The fabricated device was then tested for its performance at 0 voltage and 0 current and the current-voltage curve was obtained.

5.3 Results and discussion

5.3.1 Material application (Electrochemical efficiency)

The active layers of the solar cells were evaluated for their electrochemical efficiencies and the results are presented in **Table 5.1-5.8**. **Table 5.9** gives a summary of the obtained results on the electrochemical efficiencies of the prepared active layers, and the optimal ratio achieved. Amongst all the prepared ratios (1:1, 1:3, 1:6 and 3:1), 1:3 was found to possess the optimal electrochemical efficiency. And when all the metals were used comparably against each other in the active layer (i.e, GQD:G, GQD:Al and GQD:Au), GQD:Al was found to exhibit the highest electrochemical efficiency compared to when the other metal nanoparticles were

used. According to the results obtained in Chapter 4, graphene has a very low energy gap between the HOMO and the LUMO, and this may justify the low band gap of GQD:G redox potential observed as compared to the other nanocomposites (Bayat and Saievar-Iranizad, 2017; Mombrú *et al.*, 2018; Pattarapongdilok and Parasuk, 2018). In theory, materials with low band gaps usually exhibit high solar efficiencies. As was envisaged, the low work-function of Aluminium improved electron injection and improved the open circuit voltage and hence the highest electrochemical efficiency as compared to the other redox couples. The respective electrochemical efficiencies of the other prepared ratios are presented in Appendix, however, the successful ratios (1:3) are presented in the preceding tables.

Table 5.1: Electrochemical efficiencies of graphene quantum dots

Parameters					
Scan rate	J_{sc} (µA)	V_{oc} (mV)	P_{max} (nW)	FF (%)	Ef (%)
10	0.058	8.787	0.238	46.7	0.049
20	0.090	8.171	0.356	48.5	0.073
30	0.116	0.008	0.478	51.4	0.099
40	0.151	7.883	0.591	49.6	0.122
50	0.155	8.408	0.742	56.8	0.153
60	0.190	9.320	0.979	55.3	0.202
70	0.219	8.616	1.052	55.7	0.217
80	0.248	0.009	1.291	58.1	0.267
90	0.267	9.563	1.576	61.7	0.325
100	0.277	9.761	1.591	58.8	0.328

Table 5.2: Electrochemical efficiencies of graphene

Parameters					
Scan rate	J_{sc} (mA)	V_{oc} (mV)	P_{max} (µW)	FF (%)	Ef (%)*e-3
10	0.067	0.025	1.162	68.5	0.240
20	0.121	0.031	2.462	64.6	0.508
30	0.175	0.041	4.574	63.4	0.944
40	0.224	0.040	5.363	59.8	1.110
50	0.276	0.045	7.225	58.2	1.490
60	0.329	0.053	0.010	57.4	2.050
70	0.377	0.051	10.45	54.7	2.160
80	0.433	0.063	0.015	55.3	3.110
90	0.497	0.086	24.291	57	5.010
100	0.569	0.117	38.549	57.8	7.960

Table 5.3: Electrochemical efficiencies of GQD:graphene

Parameters					
Scan rate	J_{sc} (µA)	V_{oc} (V)	P_{max} (nW)	FF (%)	Ef (%)*e-6
10	1.262	0.025	32.561	104	6.72
20	2.333	0.027	0.074	118	15.3
30	3.411	0.030	0.119	117	24.5
40	4.323	0.020	0.092	106	19.0
50	5.277	22.248	0.113	95.9	23.2
60	6.338	0.020	0.116	91.0	24.0
70	7.459	0.024	0.149	84.1	30.8
80	8.248	20.448	0.133	78.6	27.4
90	9.417	0.026	0.193	78.4	39.9
100	0.025	0.088	0.601	27.3	0.124

Table 5.4: Electrochemical efficiencies of Aluminium

Parameters					
Scan rate	J_{sc} (µA)	V_{oc} (V)	P_{max} (µmW)	FF (%)	Ef (%)*e-6
10	45.494	0.097	2.116	48	0.437
20	0.068	0.047	1.599	50.7	0.330
30	0.084	33.379	1.440	51.2	0.297
40	0.106	0.037	0.002	50.5	0.413
50	0.123	0.032	1.930	49.3	0.398
60	0.137	0.027	1.805	48.7	0.373
70	0.148	25.595	1.836	48.5	0.379
80	0.157	25.580	0.002	50.1	0.414
90	0.182	24.284	2.038	46.2	0.421
100	0.192	0.023	2.073	47.4	0.428

Table 5.5: Electrochemical efficiencies of GQD/Aluminium

Parameters					
Scan rate	J_{sc} (µA)	V_{oc} (mV)	P_{max} (nW)	FF (%)	Ef (%)*e-6
10	0.047	14.719	0.273	39.2	0.056
20	0.067	13.278	0.353	39.6	0.073
30	0.080	0.013	0.423	40.5	0.087
40	0.092	12.535	0.538	46.6	0.111
50	0.101	12.428	0.557	44.2	0.115
60	0.113	12.184	0.617	44.8	0.127
70	0.127	11.823	0.673	44.7	0.139
80	0.134	11.701	0.720	45.9	0.149
90	0.146	11.420	0.775	46.6	0.160
100	0.160	11.613	0.867	46.5	0.179

Table 5.6: Electrochemical efficiencies of the prepared gold nanoparticles

Parameters					
Scan rate	J_{sc} (µA)	V_{oc} (V)	P_{max} (nW)	FF (%)	E_f (%)*e-6
10	0.059	0.039	1.055	45.5	0.218
20	0.095	0.045	0.002	46.7	0.414
30	0.124	0. 051	3.068	48.6	0.633
40	0.161	0.063	4.859	47.4	1.00
50	0.184	0.057	5.175	49.4	1.07
60	0.233	0.077	8.200	45.7	1.69
70	0.245	0.067	7.786	47.6	1.61
80	0.280	0.075	9.832	47	2.03
90	0.318	0.090	0.013	45.7	2.70
100	0.366	0.109	17.49	43.8	3.61

Table 5.8: Electrochemical efficiencies of GQD/gold

Parameters					
Scan rate	J_{sc} (µA)	V_{oc} (V)	P_{max} (nW)	FF (%)	Ef (%)*e-6
10	0.056	11.35	0.368	57.4	0.076
20	0.093	9.727	0.498	54.9	0.103
30	0.135	0.011	0.767	51.9	0.158
40	0.165	11.17	0.949	51.4	0.196
50	0.199	12.63	1.315	52.4	0.271
60	0.234	14.73	1.784	51.7	0.368
70	0.276	17.36	2.481	51.7	0.512
80	0.317	21.43	3.533	52.0	0.729
90	0.376	0.029	5.591	51.7	1.150
100	0.448	0.045	10.24	51.2	2.110

According to the results presented above, the solar-to-electricity conversion efficiency of the active layer increases with increasing scan rate. The results above were summarized and presented in **Table 5.9**.

Table 5.9: Electrochemical efficiencies of GQD:Al, GQD:Au and GQD:G

Obtained Results	Sample		
	GQD:G	GQD:Al	GQD:Au
J_{sc} (µA)	0.448	25.0	0.160
V_{oc} (mV)	45.0	88.0	11.6
P_{max} (µmW)	10.2	601	0.867
FF (%)	51.2	27.3	46.5
Ef (%)	2.11e-6	0.124	0.179e-6

5.3.2 Material testing (Photovoltaic efficiency)

The I-V characteristics (**Figure 5.1-5.3**) of the fabricated solar cells (Area = 0.0256 cm^2) using the prepared GQD donor materials with different accepting metal nanoparticles were measured in the dark and under simulated AM 1.5 illumination (Pi = 100 mW/cm^2). The corresponding photovoltaic parameters are summarised in **Table 5.10-5.13**. Optimisation of the solar cell efficiency started with optimising the concentration, finding the optimal thickness and fabricating the inverted Schottky junction solar cell. When the concentration of the active layer in the solar cells was low, the solar cells gave low solar-to-electricity conversions as can be observed in **Figure 5.1**. An increment in the material concentration gave better efficiencies as may be observed in **Figure 5.2**. However, the highest efficiencies were obtained when all the parameters were optimised in the inverted version.

The baseline efficiency of 0.57 % was calculated for the least concentration of 10 mg/ml GQD:Al. By increasing the concentration of the active layer to 20 mg/ml GQD:Al, the V_{oc} and the J_{sc} increased, subsequently resulting in an increase in efficiency to 1.02 %. The enhancement of V_{oc} and the J_{sc} can be attributed to a high absorption coefficient and morphology of the solar cell, and hence an enhanced electron flow. Improved absorption of light introduces more photo-generated carriers and leads to improved J_{sc}.

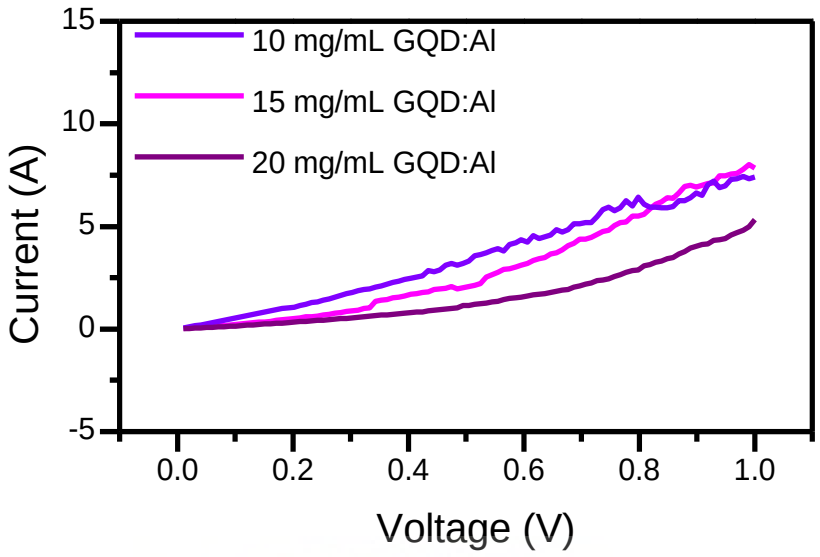

Figure 5.1: Solar-to-electricity conversion capabilities of 10 mg/mL, 15 mg/mL and 20 mg/mL GQD:Al nanocomposite redox couples.

Table 5.10: Electrochemical efficiencies of 10 mg/mL, 15 mg/mL and 20 mg/mL GQD:Al (Electrochemical efficiencies of GQD:G, GQD:Al and GQD:Au Schottky junction solar cells at different concentrations)

Obtained Results	Sample		
	10 mg/mL GQD:Al	15 mg/mL GQD:Al	20 mg/mL GQD:Au
J_{sc} (mA.cm^{-2})	3.6	3.6	3.6
V_{oc} (mV)	2.7	2.7	2.7
P_{max} (kW)	1.45	2.39	2.62
FF (%)	21.6	24.7	14.4
Ef (%)	0.57	0.93	1.02

The baseline efficiency of 0.36% was calculated for GQD:Au when all the metals were used as acceptors in the active layer. By using a different acceptor in the active layer such a graphene to result in GQD:Gr, the V_{oc} and the J_{sc} increased, subsequently resulting in an increase in efficiency to 2.17%. The enhancement of V_{oc} and the J_{sc} can be attributed to a high absorption coefficient and morphology of the solar cell, and hence an enhanced electron flow. Improved absorption of light introduces more photo-generated carriers and lead to improved Jsc.

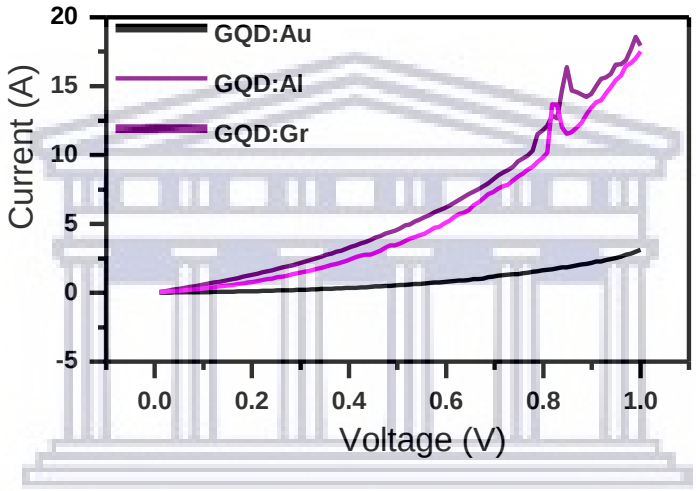

Figure 5.2: Solar-to-electricity conversion capabilities of GQD:Au, GQD:Al and GQD:G nanocomposite redox couples.

Table 5.11: Electrochemical efficiencies of GQD:Al, GQD:Au and GQD:G

Obtained Results	Sample		
	GQD:G	GQD:Al	GQD:Au
J_{sc} (mA.cm^{-2})	3.6	3.6	3.6
V_{oc} (mV)	2.7	2.7	2.7
P_{max} (kW)	5.55	4.86	0.93
FF (%)	21.6	14.4	24.7
Ef (%)	2.17	1.90	0.36

For the inverted Schottky junction solar cells, a baseline efficiency of 1.51% was calculated for GQD:Gr. By using a different acceptor in the active layer such as gold; GQD:Au, the V_{oc} and the J_{sc} increased, subsequently resulting in an increase in efficiency to 2.69%. The enhancement of V_{oc} and the J_{sc} can be attributed to a high absorption coefficient and morphology of the solar cell, and hence an enhanced electron flow. Improved absorption of light introduces more photo-generated carriers and leads to improved J_{sc}.

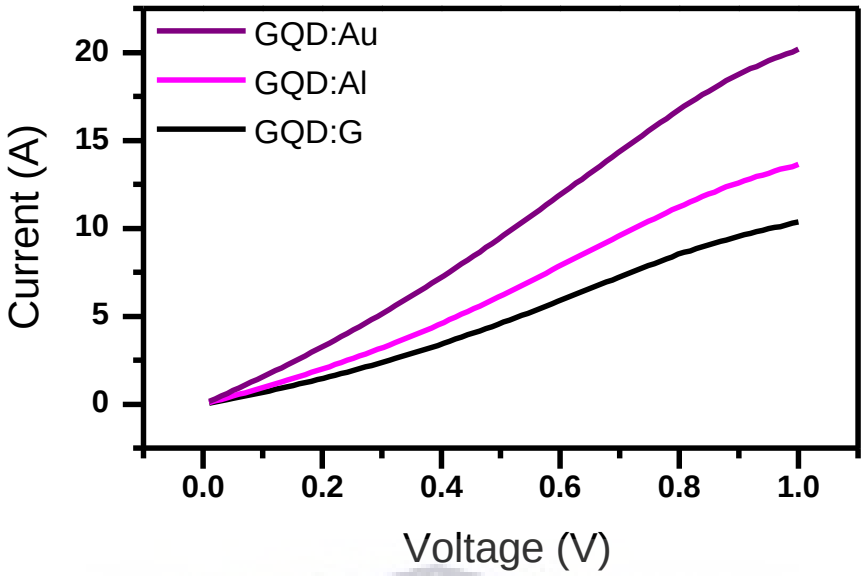

Figure 5.1: Solar-to-electricity conversion capabilities of Schottky junction solar cells made from GQD:G, GQD:Al and GQD:Au active layers.

Table 5.10: Electrochemical efficiencies of GQD:G, GQD:Al and GQD:Au Schottky junction solar cell at different concentrations

Obtained Results	Sample		
	GQD:G	GQD:Al	GQD:Au
J_{sc} (mA.cm^{-2})	3.6	3.6	3.6
V_{oc} (mV)	2.7	2.7	2.7
P_{max} (kW)	3.86	5.07	6.88
FF (%)	21.6	14.4	24.7
Ef (%)	1.51	1.98	2.69

The reason for the comparably high efficiency of GQD:Au may be attributed to the energy difference between the highest occupied molecular orbital (HOMO) and the

lowest unoccupied molecular orbital (LUMO) energy level. Moreover, other parameters may be taken into consideration, such as the inter-chain distances, charge recombination, bulkiness of side chains and morphology of active layer, which have also been demonstrated to have a noticeable effect on the fill factor (Yamaguchi and Ohdaira, 2017; Fischer *et al.*, 2018; Cui and Maruyama, 2019). In 2010, Xinming *et al.* fabricated a Schottky junction solar cell by creating a junction between graphene and semiconducting silicon with different device areas (i.e., 0.1 cm^{-2} and 0.5 cm^{-2}). The highest efficiency of 1.65% was achieved for the device with the smallest area, 0.1 cm^{-2}, while the other one (0.5 cm^{-2}) resulted in 1.34% comparably low to those obtained in this study (Li *et al.*, 2010). In 2014, Xuan-Dung *et al.* fabricated an inverted Schottky colloidal quantum dot solar cell of PbS CQD sandwiched between a low work function transparent conducting oxide and a high work function metal anode and achieved a highest power conversion efficiency of 3.8% (Kim *et al.*, 2014). This efficiency is closer to the highest obtained efficiency in this study (2.69%), although still lower. This implies that there is still room for improvement.

5.4 **Conclusion**

The Schottky junction photoactive films composed of graphene quantum dots (GQDs), Aluminium (Al), gold (Au) and graphene (Gr) metals have been prepared by spin coating to establish optimal concentration and composition of these materials of interest. Amongst all prepared donor to acceptor ratios of 1:1, 1:3. 1:6 and 3:1, the 1:3 ratio was found to possess optimal electrochemical efficiency and thus was used for fabrication of the solar cells. The metal/semiconductor Schottky junction solar cells were thereafter successfully prepared and characterized. Different concentrations (i.e., 10 mg/mL, 15 mg/mL and 20 mg/mL) of the active layer were prepared for optimisation of the solar cells. The optimal concentration was found to be 20 mg/mL and was used to fabricate all other solar cell devices. When the solar cell devices were fabricated using the three different types of metals, the solar cell with GQD:Au as the active layer possessed high solar-to-electricity conversion efficiency upon light illumination. This can be subscribed to the reduction of the hot-electrons produced upon illumination by light. The results obtained in this study (2.69%) considerably close to the optimal Schottky junction solar cell, 3.8%.

References

Arshad, A. *et al.* (2019) 'A review on graphene based nanofluids: Preparation, characterization and applications', *Journal of Molecular Liquids*, 279, pp. 444–484.

Bayat, A. and Saievar-Iranizad, E. (2017) 'Synthesis of green-photoluminescent single layer graphene quantum dots: Determination of HOMO and LUMO energy states', *Journal of Luminescence*, 192, pp. 180–183.

Cao, X. *et al.* (2016) 'Band Gap Opening of Graphene by Forming Heterojunctions with the 2D Carbonitrides Nitrogenated Holey Graphene, g-C_3N_4 , and g-CN: Electric Field Effect', *The Journal of Physical Chemistry C*, 120, pp. 11299–11305.

Chen, L. *et al.* (2018) 'Numerical simulation of planar BaSi2 based Schottky junction solar cells toward high efficiency', *Solid-State Electronics*, 149, pp. 46–51.

Cui, K. and Maruyama, S. (2019) 'Multifunctional graphene and carbon nanotube films for planar heterojunction solar cells', *Progress in Energy and Combustion Science*, 70, pp. 1–21.

Fischer, S. *et al.* (2018) 'Upconversion solar cell measurements under real sunlight', *Optical Materials*, 84, pp. 389–395.

Kusuma, J. *et al.* (2018) 'Exploration of graphene oxide nanoribbons as excellent electron conducting network for third generation solar cells', *Solar Energy Materials and Solar Cells*, 183, pp. 211–219.

Li, C. *et al.* (2018) 'Asymmetric quantum confinement-induced energetically and spatially splitting Dirac rings in graphene/phosphorene/graphene heterostructure', *Carbon*, 140, pp. 164–170.

Li, Xinming *et al.* (2010) 'Graphene-on-silicon schottky junction solar cells', *Advanced Materials*, 22, pp. 2743–2748.

Lin, S. *et al.* (2017) 'High performance graphene/semiconductor van der Waals heterostructure optoelectronic devices', *Nano Energy*, 40, pp. 122–148.

Liu, R. *et al.* (2011) 'Bottom-Up Fabrication of Photoluminescent Graphene Quantum Dots with Uniform Morphology', *Journal of the American Chemical Society*, 133, pp. 15221–15223.

Mombrú, D. *et al.* (2018) 'Curvature and vacancies in graphene quantum dots', *Applied Surface Science*, 462, pp. 540–548.

Nair, A. K. *et al.* (2018) 'Chapter 10 – Optical Characterization of Nanomaterials', in *Characterization of Nanomaterials*, pp. 269–299.

Pattarapongdilok, N. and Parasuk, V. (2018) 'Theoretical study on electronic properties of curved graphene quantum dots', *Computational and Theoretical Chemistry*, 1140, pp. 86–97.

Potsi, G. *et al.* (2019) 'Intrinsic photoluminescence of amine-functionalized graphene derivatives for bioimaging applications', *Applied Materials Today*, 17, pp. 112–122.

Rezaei, A., Kamali, B. and Kamali, A. R. (2020) 'Correlation between morphological, structural and electrical properties of graphite and exfoliated graphene nanostructures', *Measurement*, 150, p. 107087.

Shin, D. H. *et al.* (2017) 'Graphene/porous silicon Schottky-junction solar cells', *Journal of Alloys and Compounds*, 715, pp. 291–296.

Suhail, A. *et al.* (2018) 'Improved efficiency of graphene/Si Schottky junction solar cell based on back contact structure and DUV treatment', *Carbon*, 129, pp. 520–526.

Tiwari, S. K. *et al.* (2016) 'Magical Allotropes of Carbon: Prospects and Applications', *Critical Reviews in Solid State and Materials Sciences*, 41, pp. 257–

317.

Tu, W. *et al.* (2019) 'Intrinsic mechanical properties and fracture mechanism of monolayer penta-graphene investigated by nanoindentation: A molecular dynamics study', *Computational Materials Science*, 169, p. 109145.

Wang, J. *et al.* (2019) 'Graphene and graphene derivatives toughening polymers: Toward high toughness and strength', *Chemical Engineering Journal*, 370, pp. 831–854.

Wu, C. *et al.* (2018) 'High-sensitivity silicon-based photonic crystal refractive index biosensor based on defect-mode coupling', *Optics Communications*, 427, pp. 409–417.

Williams, K. J. *et al.* (2013) 'Hot electron injection from graphene quantum dots to TiO2', *ACS Nano*, 7, pp. 1388–1394.

Xie, C. *et al.* (2018) 'Graphene/Semiconductor Hybrid Heterostructures for Optoelectronic Device Applications', *Nano Today*, pp. 41–83.

Yamaguchi, S. and Ohdaira, K. (2017) 'Degradation behavior of crystalline silicon solar cells in a cell-level potential-induced degradation test', *Solar Energy*, 155, pp. 739–744.

Zhai, L.-F. *et al.* (2019) 'Facile synthesis of Co-N-rGO composites as an excellent electrocatalyst for oxygen reduction reaction', *Chemical Engineering Science*, 194, pp. 45–53.

Zhang, L. *et al.* (2017) 'Tuning the work functions of graphene quantum dot-modified electrodes for polymer solar cell applications', *Nanoscale*, 9(10), pp. 3524–3529.

CHAPTER 6

Summary

This chapter discusses the synthesis and application of metal doped graphene materials in fuel cell reactions. The study was conducted in Portugal as part of the requirement for the PhD degree in Chemistry at SensorLab research group, Department of Chemistry, University of the Western Cape. The increasing over-usage of fossil fuels causes inevitable complications due to the high demand of energy, as a result, the world needs to shift focus to renewable energy sources. This study focuses on the development of alternative electrocatalysts to replace the state-of-the-art PtC catalysts with convenient catalysts which are low in cost and highly selective to oxygen reduction reactions (ORR – in methanol).

Cobalt (Co) impregnated S,N-doped graphene versus manganese (Mn) impregnated S,N-doped graphene for fuel cell reactions

Abstract

Fuel cells devices translate fuel heat of combustion directly into electricity. The fuel cell is clean in a sense that it only emits water and/or carbon dioxide as a by-product. At the anode there is electrochemical oxidation of fuel, whereas at the cathode there is reduction of oxidant (oxygen from the air). The rate-limiting step in fuel cells is the oxygen reduction reactions (ORR) on the cathode, since it dictates the power output and lifetime of the devices. Therefore, to better combine performance and stability specific attention is given to cathode development to find the best catalyst and electrode structure. One of the most commonly used and active electrocatalyst for the ORR is Platinum (Pt) and the direct 4-electron process dictates how all the reduction of oxygen by Pt-group metals occurs. Due to high cost of Pt their large-scale commercial application has been hindered. Selectivity to ORR in the presence of other reactions is low for Pt-based electrodes and they suffer from CO deactivation. Therefore, in this study, S,N-dual doped graphene is evaluated for its activity for ORR under alkaline conditions against cobalt and manganese loaded graphene catalysts. Characterisation techniques such as FTIR, Raman, TEM and XRD confirm the structure of the catalysts. When oxygen reduction reactions were conducted under alkaline conditions, it was found that the manganese containing S,N-doped graphene exhibited the optimal activity for the production of water molecules through a $4e^-$ route. The stability and durability test of the materials were also conducted and Mn/S_3N_2-GF catalyst still had high selectivity towards ORR even

in the presence of methanol, which renders it attractive for the development of alkaline fuel cells.

6.1 Introduction

Electro-catalytic oxygen reduction/evolution reactions plays an important role in many energy storage and conversion devices including fuel cells, water splitting and rechargeable metal-air batteries (McKerracher *et al.*, 2016; Zhang *et al.*, 2017). The ORR and OER are thermodynamically climbing reactions that are rate determining steps for electron transfer at high overpotentials (Qian *et al.*, 2015; S. Jiang *et al.*, 2018). This is because they suffer from sluggish kinetics with a complicated multielectron transfer step. Therefore, preparation of highly active and stable bifunctional electrocatalysts is of utmost importance in the improvement of the overall efficiencies electrochemical devices (Zhang *et al.*, 2015, 2018; Sadhasivam *et al.*, 2018). Experimental investigations have proven that Rhu- and Ir- based electro-catalysts are highly active for OER processes, while Pt metal and Pt-based materials are mostly preferred for ORR processes (C. Li *et al.*, 2018; Ejaz and Jeon, 2018; Tafen, Kauffman and Alfonso, 2018; Velasco-Vélez *et al.*, 2018; Zaman *et al.*, 2018). Despite their high activity and desirable properties, commercialisation of these materials has been hindered by their scarcity, high cost and poor stability (Gan *et al.*, 2013; Chen *et al.*, 2018; Giarratano *et al.*, 2018). The need for innovation and simplicity requires the development of low-cost bifunctional catalysts for both OER and ORR processes. Research on these bifunctional electro-catalysts has since exploded and reports reveal many active catalysts which include; carbon materials, perovskites, transition-metal oxides, sulphides and nitrides (Gupta *et al.*, 2016;

Alegre *et al.*, 2018; J. Li *et al.*, 2018; Mamtani *et al.*, 2018; Park *et al.*, 2018; Surya, Michael and Prabaharan, 2018).

Earth-abundant first-row transition metal-nitrogen doped carbon (M-N-C), catalysts have been labelled as potential catalysts to displace the expensive Pt/C since the first observation of considerable ORR activity on the Co macrocyclic complex in 1964 (Bezerra *et al.*, 2008; Davodi *et al.*, 2018; Gebremariam *et al.*, 2018). Cobalt is considered the most electrocatalytically superior catalysts compared to all, owing to its high stability and exceptional 3d electronic configurations. However, the use of cobalt is limited due to the low activity that is caused by insufficient electrical conductivity and self-aggregation (Mani *et al.*, 2015; Wu *et al.*, 2018). Carbon materials have been proven to modulate the electrical conductivity of cobalt for an increased charge transport and exposed active sites due to the high surface area of carbon, thereby promoting the catalytic activity of cobalt (Yun, Ahmed and Jeon, 2015; Tang and Ng, 2017). However, research studies report a limit in electron transfer at the interface and restricted electro-catalytic tunability caused by the lack of bridged bonds between the carbon lattice and cobalt oxide, commanding the use of doped carbon to create effective bonds. Therefore; in this study, graphene is doped with heteroatoms nitrogen and sulphur to serve as bridging atoms to facilitate electron transport. Innovative science calls for the development and improvement of electro-catalysts which offer strongly coupled effects, exposure of numerous active sites on the surface, abundant Co-N-C active sites and better electron transfer capacity.

The work done in this study promotes development of materials that are inexpensive non-noble metal hybrid for application in bifunctional ORR electro-catalysts.

6.2 Methodology

6.2.1 Preparation of S,N-doped graphene

Commercial graphene (400 mg) was mixed with different S,N-dopants (i.e., 2,5-dimercapto-1,2,3-thiodazole - S_3N_3; trithiocyanuric acid - S_3N_2 or 4-amino-3-hydrazino-5-mercapto-1,2,4-trazole - SN_6) for a comparative study and subjected to ball milling for 5 h at a constant frequency of 15 vibrations/s. The resulting powder was then subsequently subjected to calcination at 800 ^oC under nitrogen for 1 h and S,N-doped graphene was obtained.

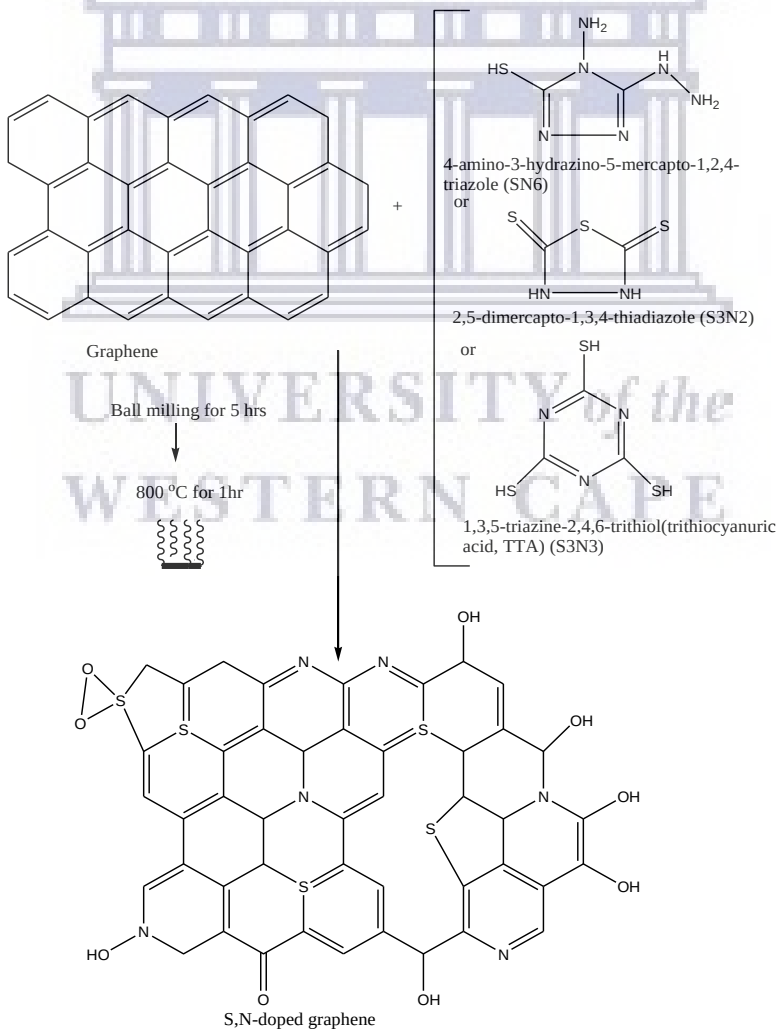

Figure 6.1: Representation of the preparation of S,N-doped graphene

6.2.2 Preparation of Co/S,N-doped graphene

N,S-doped graphene (235 mg), prepared in **6.2.1** was mixed with 4 mmol $CoCl_2.6H_2O$ in 50 mL H_2O. The resulting solution was then mixed with 3 M amino-2-propanol to reach a pH of 10 at a speed of 50 mL/h and stirred for 24 h at room temperature. The resulting slurry was then filtered and washed with ethanol and subsequently dried overnight under vacuum to obtain solid nanoparticles. The resulting powder nanoparticles were then ground to fine powder and calcined at 250 ^oC for 3 h in air.

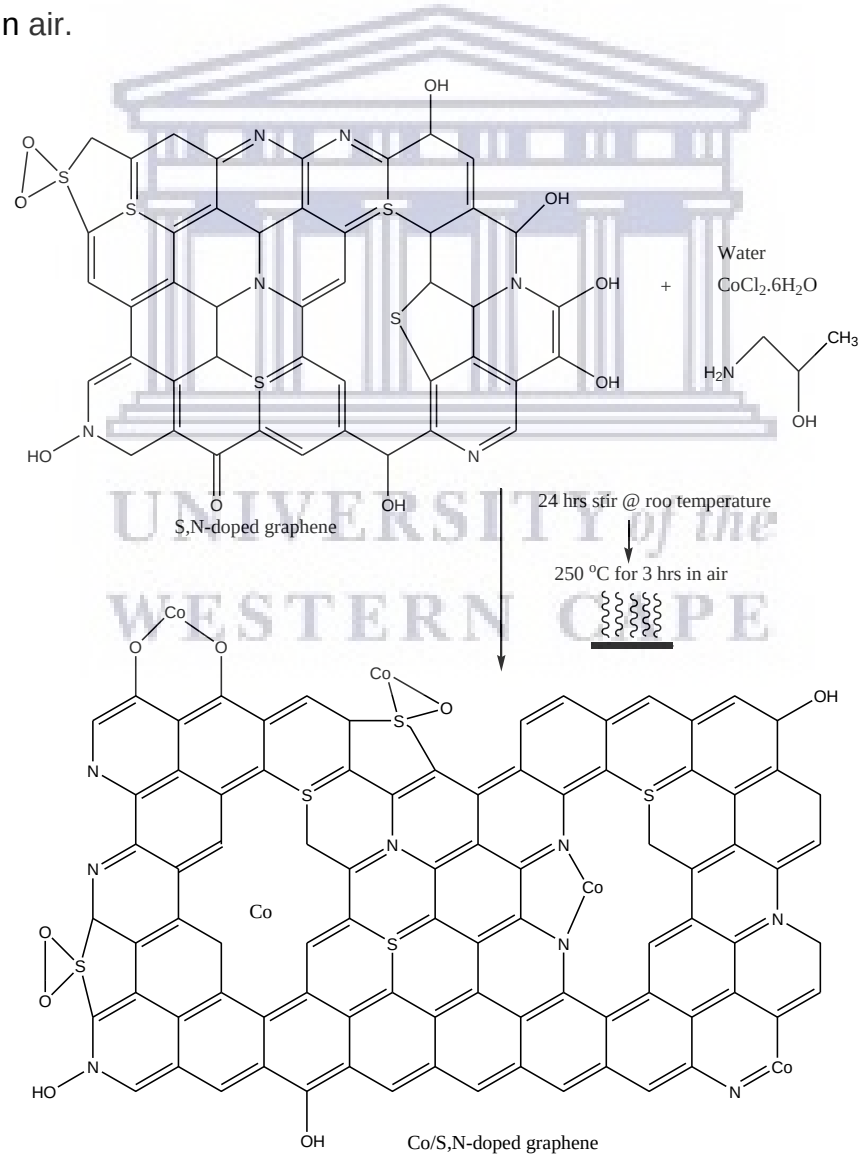

Figure 6.2: Preparation of Co/S,N-doped graphene

6.2.3 Synthesis of Mn/S,N-doped graphene

N,S-doped graphene (217 mg), prepared in **6.2.2** was mixed with 4.4 mmol $MnCl_2.4H_2O$ in 50 mL H_2O. The resulting solution was then mixed with 3M amino-2-propanol to reach a pH of 10 at a speed of 50 mL/h and stirred for 24 h at 80 ^oC. The resulting slurry was then filtered and washed with ethanol and subsequently dried overnight under vacuum to obtain solid nanoparticles. The resulting powder nanoparticles were then ground to fine powder and calcined at 300 ^oC for 5 h in air.

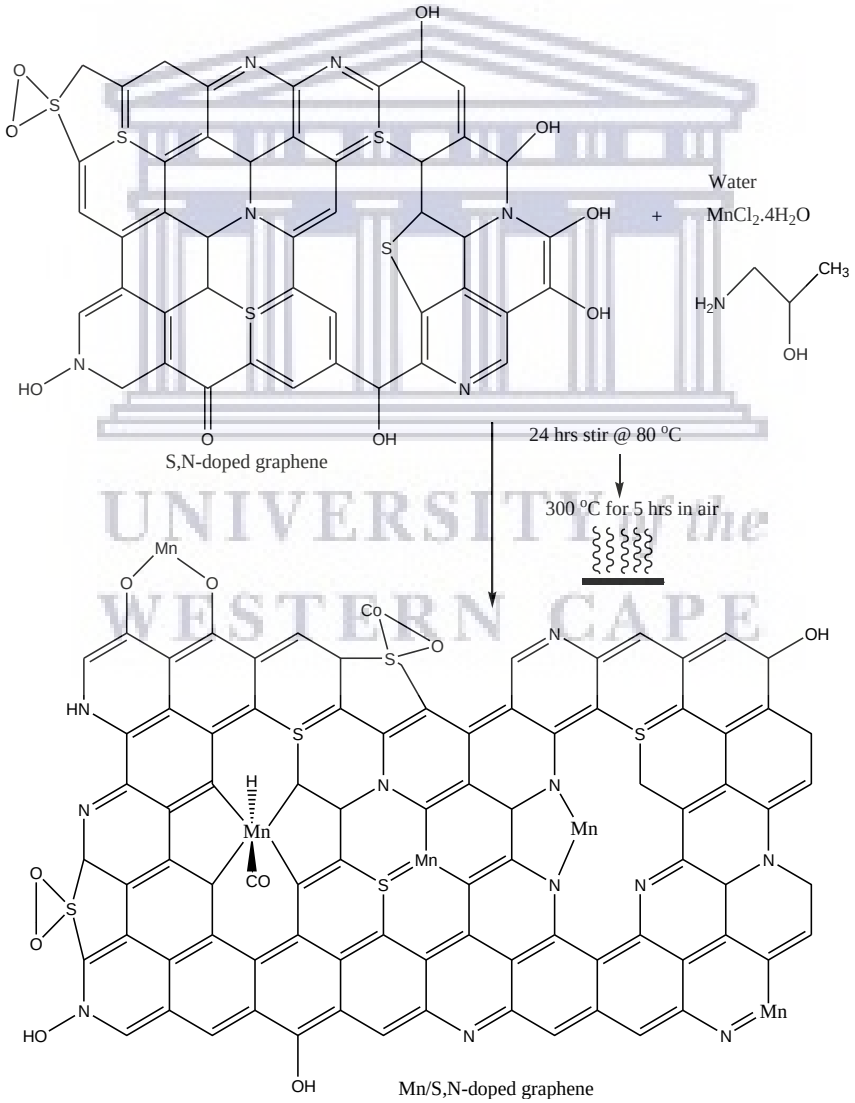

Figure 6.3: Illustration of Mn on S,N- doped graphene

6.3 Results and discussion

6.3.1 Fourier Transform Infrared Spectroscopy (FTIR)

Infrared spectroscopy is a characterization technique used at the molecular scale to elucidate the structure of matter. Infrared (IR) spectroscopy can be used to study constituents in a homopolymer, copolymer, polymer composite and polymeric materials for their chemical composition and the bonding arrangement. Thus, infrared spectroscopy allows for identification of the molecular structure, which permits determination of components or groups of atoms that absorb in the infrared at specific frequencies (Weisz *et al.*, 2002; Mauricio-Sánchez *et al.*, 2018; Petit and Puskar, 2018). Therefore, with the permission of FTIR spectroscopy, the prepared graphene materials were evaluated for their functional groups present in the structures.

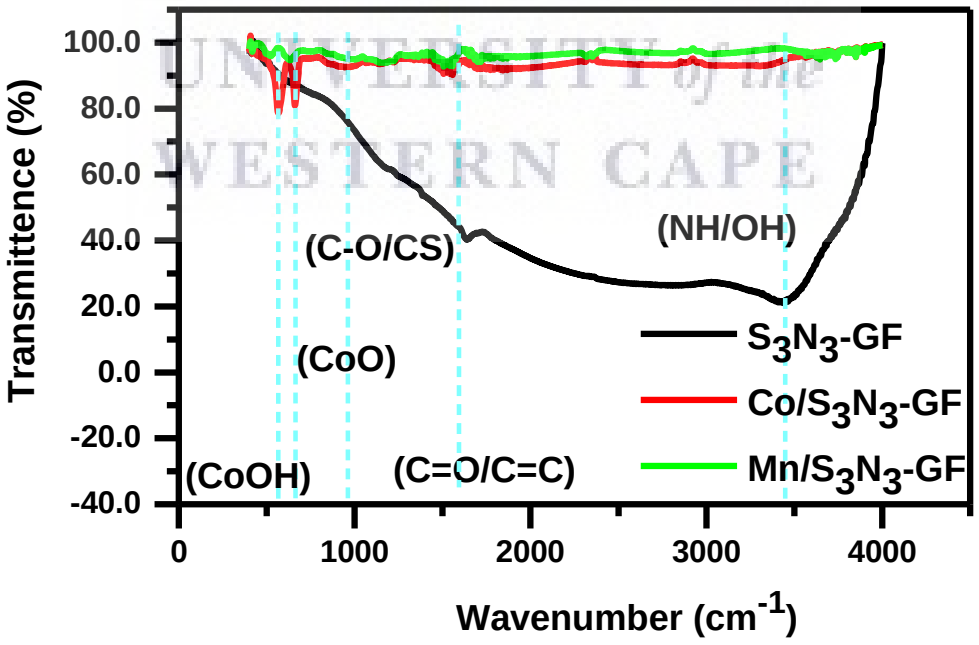

Figure 6.4: FTIR of samples prepared from S_3N_3 dopant and loaded with cobalt and manganese respectively.

The characteristic FTIR spectrum of graphene nanosheets is shown in **Figure 6.4**. It is observed with oxygen-containing groups in which the main absorption band at 3424 cm^{-1} is attributed to the N-H/O-H group stretching vibrations. The absorption band at 1537 cm^{-1} is attributed to the C=O stretching of the carboxylic and/or carbonyl functional groups, which overlaps with the N-O functional group from the nitrogen dopant. The absorption band at 1647 cm^{-1} is assigned to the C=O or C=C functional groups from the aromatic benzene rings on grapheme. Sulphur doping of the material shows an FTIR absorption band at 1188 cm^{-1} for C-O and C-S functional groups. This implies that the materials were successfully dual doped with both sulphur and nitrogen. The C-N-C and C-S functional groups found in the materials would serve as the active centres for the oxygen reduction reactions later in the study. Addition of the Co_3O_4 metal oxide in the system shows appearance of CoO and CoOH groups at 649 cm^{-1} and 569 cm^{-1}, respectively on Co/S_3N_3-GF sample. While, Mn/S_3N_3-GF shows Mn-O and Mn-O-C groups at 640 cm^{-1} and 569 cm^{-1}, respectively (Tian *et al.*, 2017; Khandelwal *et al.*, 2018). It is envisaged from literature and experimental studies that the metal oxides improve the catalytic efficiency of the materials.

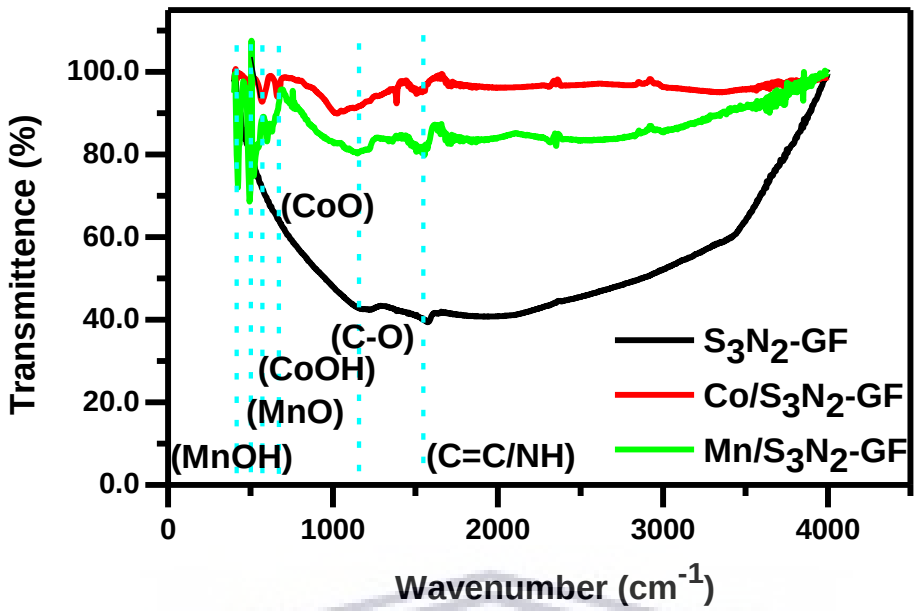

Figure 6.5: FTIR of samples prepared from S_2N_3 dopant and loaded with cobalt and manganese respectively.

Figure 6.5 shows the FTIR spectra of graphene doped with S_2N_3 and then loaded with MnO_2 and Co_3O_4 metal oxides for improved catalytic efficiency. All samples show vibrations of C=C/NH and C-O functional groups at 1552 cm^{-1} and 1156 cm^{-1}, respectively. However, introduction of Co_3O_4 the S,N-doped graphene sheets shows new band vibrations at 469 cm^{-1} and 649 cm^{-1} for CoOH and CoO, respectively on Co/S_3N_2-GF. Mn/S_3N_2-GF shows appearance of new MnO and MnOH FTIR band vibrations at 522 cm^{-1} and 410 cm^{-1}, respectively after incorporation of the MnO_2 metal oxide on the system (Mani *et al.*, 2015; Anh, Chowdhury and Doong, 2017).

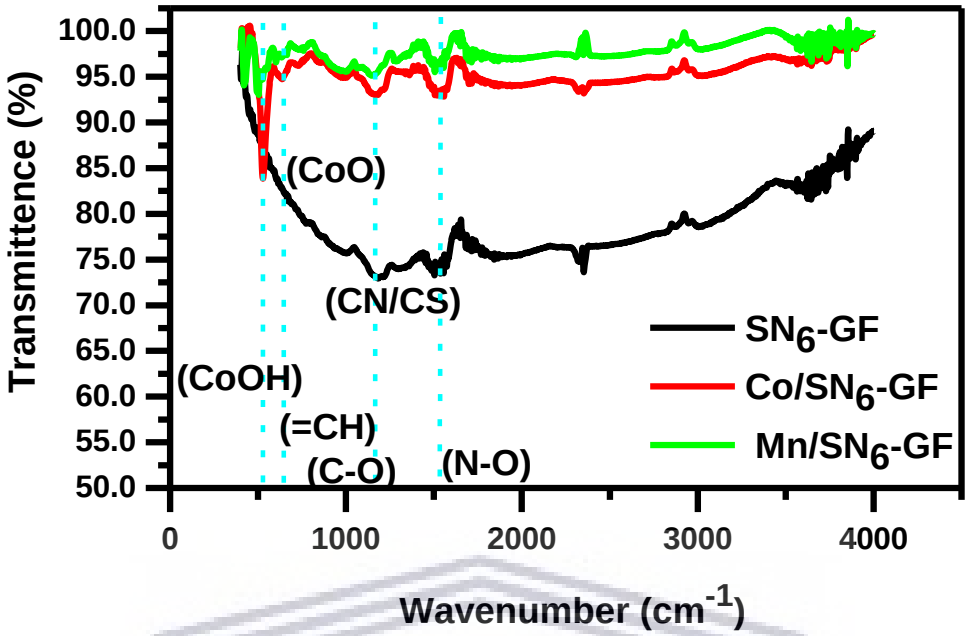

Figure 6.6: FTIR of samples prepared from SN_6 dopant and loaded with cobalt and manganese respectively.

Figure 6.6 shows the FTIR spectra of graphene doped with SN_6 and then loaded with MnO_2 and Co_3O_4 metal oxides. PM10 shows FTIR band stretching vibrations at 1521 cm^{-1}, 1188 cm^{-1}, 1013 cm^{-1} and 997 cm^{-1} for CN/CS from the dopant, C-O and =CH (from the benzene rings on grapheme) functional groups, respectively. When Co_3O_4 metal oxide was added to the doped grapheme system, new CoOH and CoO functional groups were observed at 538 cm^{-1} and 649 cm^{-1}, respectively on Co/SN_6-GF. The band vibration at 540 cm^{-1}, characteristic of MnO functional group was also observed on Mn/SN_6-GF. These FTIR results signify the successful synthesis of metal oxide containing S,N-doped graphene materials (Qu *et al.*, 2016; Mohammed *et al.*, 2018).

6.3.2 Raman

Raman spectroscopy is a high-resolution, fast, non-destructive technique for the characterization of the lattice structure and the electronic, optical, and phonon properties of carbon materials, including three-dimensional (3D) diamond and graphite, 2D graphene, 1D carbon nanotubes, and 0D fullerenes (Pourazadi *et al.*, 2018; Álvarez-Docio *et al.*, 2019). In this study, Raman spectroscopy is used to characterize doped graphene materials.

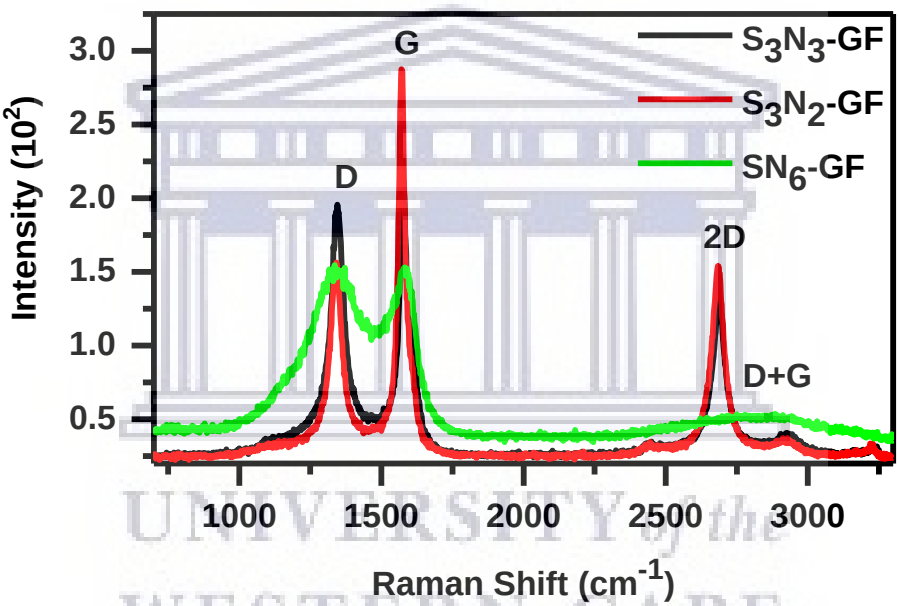

Figure 6.7: Raman spectra of S,N-dual doped graphene.

Stokes phonon energy shift because of laser excitation of graphene samples creates 2 main peaks on the Raman spectra; G band (~1580 cm^{-1}) a primary in-plane vibrational mode and 2D band (2690 cm^{-1}), a second overtone of a different in-plane vibration. In this study, graphene was dual doped with sulphur and nitrogen and thereafter loaded with cobalt/manganese for fuel cell reaction applications. The Raman spectra of the S,N-dual doped graphene shows peaks at 1350 cm^{-1} (D band), 1569 cm^{-1} (G band), 2687 cm^{-1} (2D band) and 2926 cm^{-1} (D+G band) for all

samples. However, SN_6-GF showed similar peaks as the other samples except for the broad peak on the far end of the spectrum, fusing the 2D band (2751 cm^{-1}) and the D+G band (2907 cm^{-1}) due to the increased number of defects (high number of sp^3 bonded carbon atoms) in the sample (Carrillo-Rodríguez *et al.*, 2017; Mukherjee *et al.*, 2018).

The bulk graphite, as well as intrinsic properties of samples from monolayer to few-layer graphene, can be distinguished from the spectral profile of the 2D modes. In addition, characterization of graphene-based materials with defects can be done by D peak. Experimental studies reveal that the G band is shorter than the 2D band in single layer graphene, contradicting what is observed on the presented spectra in **Figure 6.7**. Appearance of the D peak in all samples signifies their disordered nature, and Table 6.1 shows the results from I_D/I_G calculations and it may be seen that SN_6-GF is more disordered than the other samples. The concentration of disorder in graphene samples may be evaluated by calculating the ratio of I_D/I_G, for which a decrease in the value signifies a high degree in the amorphous carbon structure. However, I_D/I_G value increases as higher defect density creates more elastic scattering mostly in nanocrystalline graphene.

The two main structures of ordered crystal edges; zigzag and the armchair are caused by hexagonal structure of the graphene lattice as seen on **Figure 6.8**.

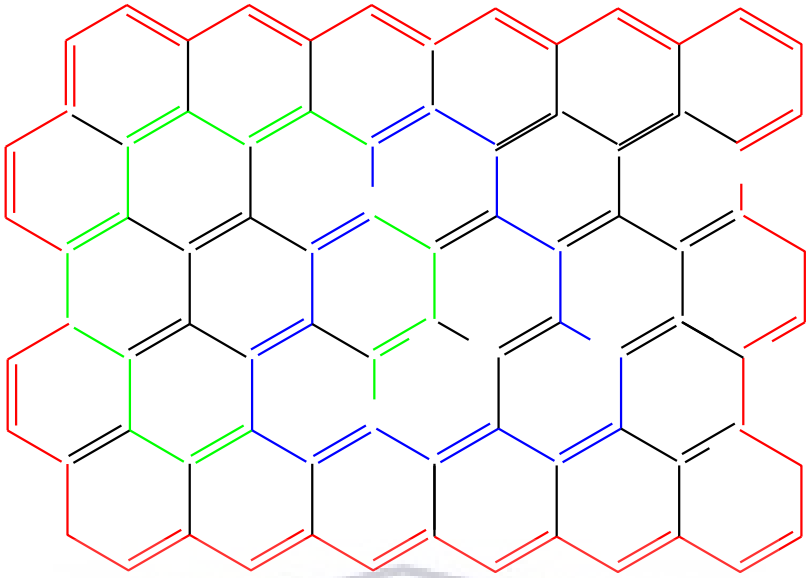

Figure 6.8: Zigzag and armchair configurations

Only armchair edges can elastically scatter charge carriers that give rise to the D peak, observed in all samples presented in **Figure 6.9**. However, a small amount of the D intensity may still be observed on zigzag edged samples due to the non-uniformity of the sample and roughness in the edge structure. This implies that appearance of the D band on the spectra does not give conclusive information on the type of edge structure that exist in the sample, therefore further characterisation still needs to be done. It has also been theorised and supported by experimental studies that activation of the longitudinal optical phonon mode occurs near the armchair edge and the activation of transverse optical phonon mode occurs near the zigzag edge so that is followed by the enhancement of the intensity of the G band when the polarization of the excited laser is perpendicular to a zigzag edge and parallel to an armchair.

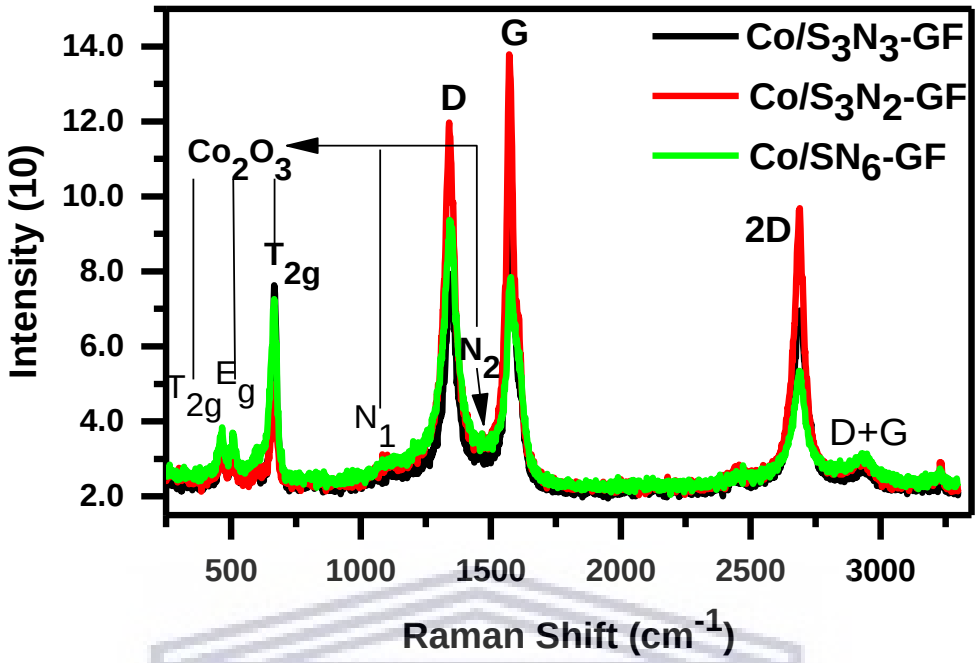

Figure 6.9: Raman spectra of Co metal on S,N-dual doped graphene with cobalt metal oxide

Graphene doping decreases the intensity of the 2D band, which may also be observed on the obtained results for Co/S_3N_3-GF which decreased from 135 (S_3N_3-GF) to 70 upon incorporation of the Co metal. The shift was also observed from 155.4 to 97 and from 53 to 52 on S_3N_2-GF and SN_6-GF, respectively upon addition of the Co metal to the samples. Graphene doping shifts the Fermi-level away from the Dirac point, decreasing the probability of charge carrier recombination. The reduced recombination increases and sharpens the G peak as can be seen in **Figure 6.9**. An increased electron (e^{-1}) concentration results in a decreased 2D band peak position, with an expanded crystal lattice, decreased Raman phonons and asymmetry in the doping effect of the G band peak position as already mention in the previous statements. Appearance of the T_{2g} (490 cm^{-1}), E_g (500 cm^{-1}), T_{2g} (750 cm^{-1}), N_1 (1300 cm^{-1}) and N_2 (1450 cm^{-1}) are due to the split in energies of the Co_2O_3

crystal lattice and signify the successful incorporation of the metal in the graphene framework (X. Jiang *et al.*, 2018; Zaghrioui *et al.*, 2018).

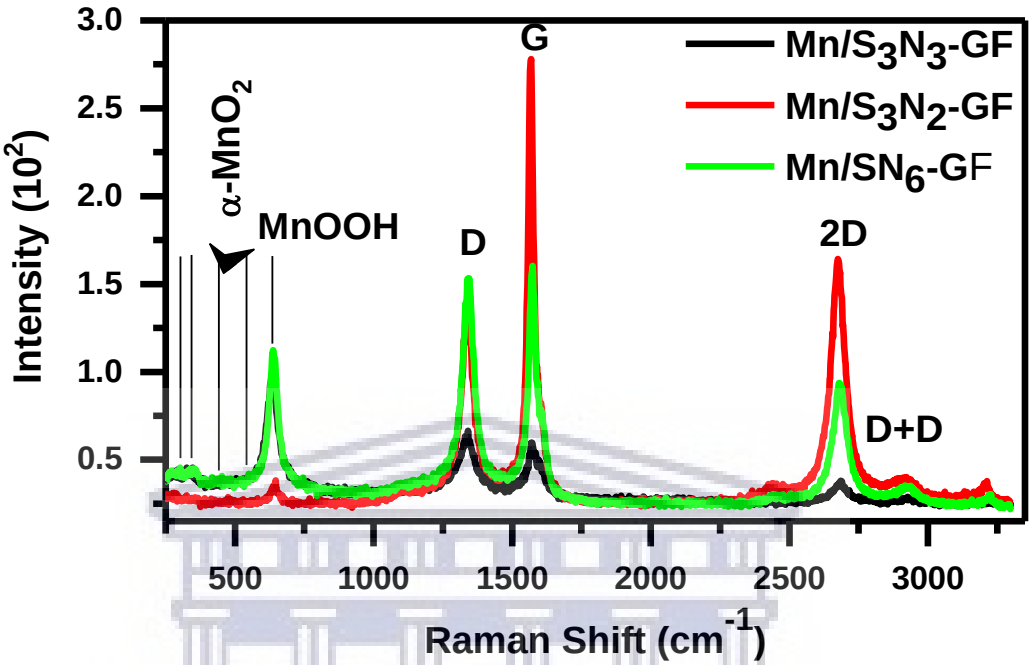

Figure 6.10: Raman spectra of Mn on S,N-dual doped graphene with manganese metal oxide

Introduction of Manganese on S,N-dual doped graphene shows appearance of new peaks on the spectra at 370 cm^{-1}, 390 cm^{-1}, 470 cm^{-1} for MnO_2 and 530 cm^{-1} and 680 cm^{-1} at MnOOH signifying successful incorporation of the sample and a change in the electronic structure of the sample. These results agree with the results obtained on FTIR spectroscopy. **Table 6.1** shows the number of layers obtained for each graphene sample (Deng *et al.*, 2018; Singu and Yoon, 2019).

Table 6.1: Summary of the Raman results

Sample	I_D/I_G	I_{2D}/I_G	I_G/I_{2D}	# of Gr layers
S_3N_3-GF	0.93	0.64	1.56	8
S_3N_2-GF	0.55	0.54	1.85	9
SN_6-GF	0.99	0.34	2.90	15
Co/S_3N_3-GF	0.77	0.68	1.47	7
Co/S_3N_2-GF	0.87	0.70	1.43	7
Co/SN_6-GF	1.19	0.67	1.49	7
Mn/S_3N_3-GF	1.10	0.64	1.56	8
Mn/S_3N_2-GF	0.51	0.60	1.67	8
Mn/SN_6-GF	0.96	0.58	1.72	9

6.3.4 **Morphological and size studies (TEM)**

Transmission electron microscopy is a unique and powerful tool for characterization of the nanostructures and morphology of the prepared metal oxide doped grapheme samples.

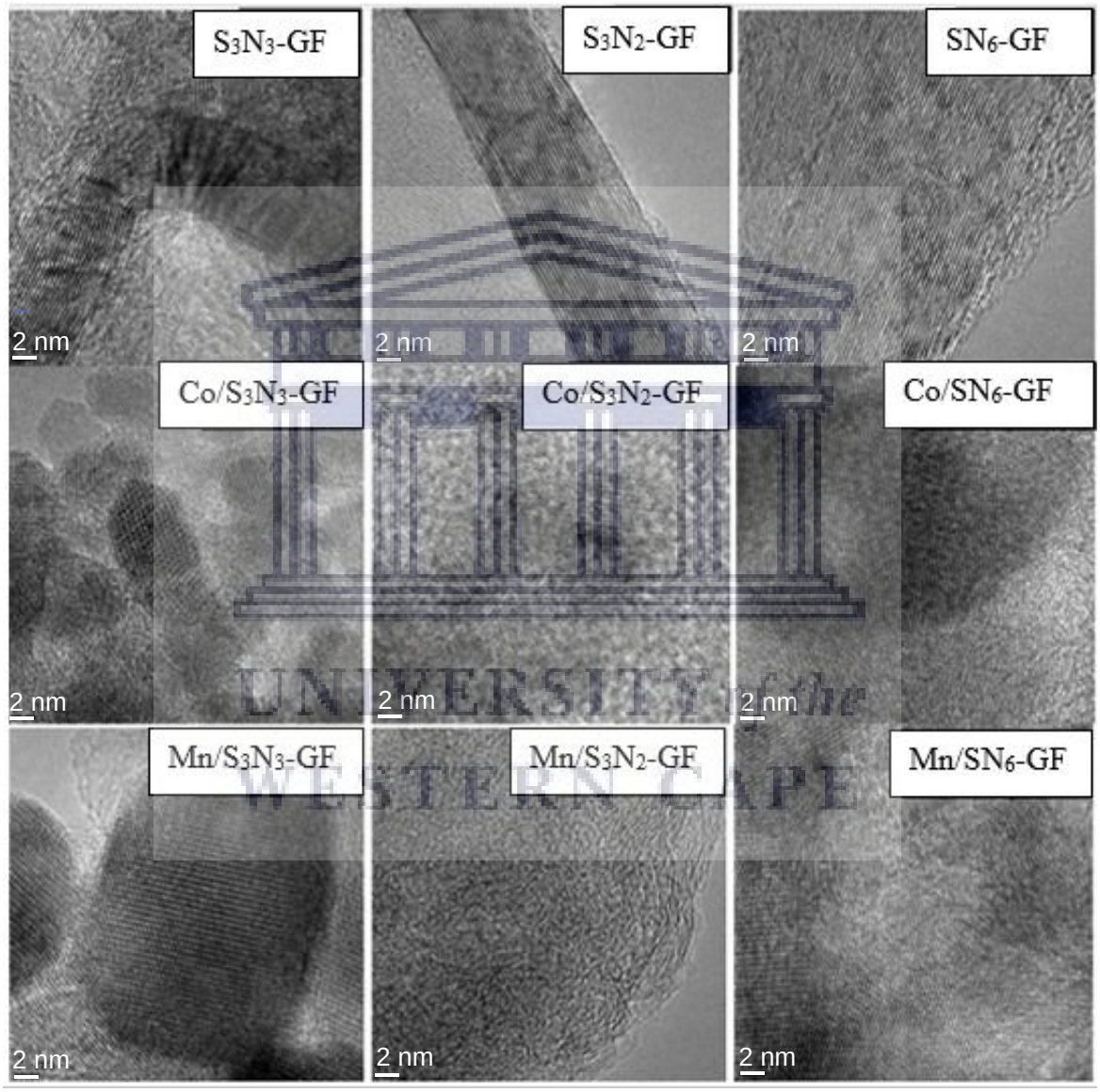

Figure 6.11: TEM micrographs of graphene sheets and graphene loaded with cobalt and manganse metals

Figure 6.11 shows TEM micrographs of the prepared materials. Samples S_3N_3-GF, S_3N_2-GF and SN_6-GF shows S,N-doped graphene sheets which appear trasparent and clear, consistenet with literature reports. Incorporation of Co_3O_4 and MnO_2 on the S,N-doped graphene samples shows the appearance of tetragonal particles dispersed on the surface of graphene (Sheikhshoaie, Ramezanpour and Khatamian, 2017; Cheng *et al.*, 2018; Mei *et al.*, 2018; Shahedi Asl, Nayebi and Shokouhimehr, 2018). Image j program was used to calculate the particle sizes of the metal oxides on the graphene samples and the particle sizes of Co/S_3N_3-GF, Co/S_3N_2-GF, Co/SN_6-GF, Mn/S_3N_3-GF, Mn/S_3N_2-GF and Mn/SN_6-GF were 5.3 ± 1.1 nm, 4.9 ± 1.0 nm, 7.6 ± 1.5 nm, 15.3 ± 3.5 nm, 15.5 ± 2.5 nm and 19.0 ± 3.1 nm, respectively. From the obtained particle sizes it may be concluded that Manganese nanoparticles have a bigger radius than the cobalt nanoparticles.

6.3.5 **X-ray diffraction (XRD)**

X-Ray diffraction analysis is a technique to determine relative configuration of solid compounds in an unequivocal way and its structure. The prepared materials were also evaluated for their crystal structures using XRD.

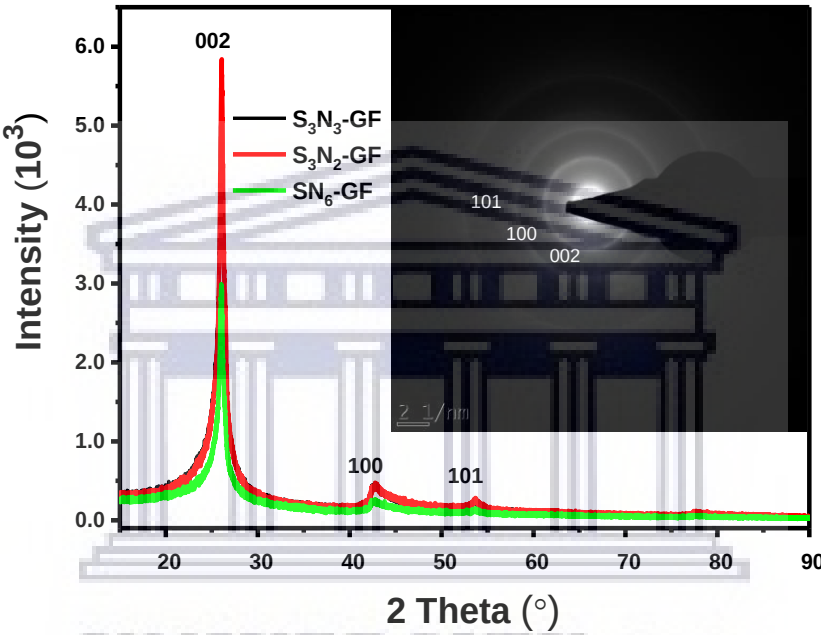

Figure 6.12: XRD of S,N-doped graphene sheets

Figure 6.12 shows the XRD spectra of the prepared S,N-graphene and from the obtained miller indexes it can be concluded that the crystal structure of the materials is a hexagonal close packed structure as shown in **Figure 6.13**. This is evidenced by the appearance of the 002, 100 and 101 XRD crystal planes at 25°, 43° and 54°, respectively, which correspond to hexagonal crystalline graphite (JCPDS No. 41-1487) (Yun, Ahmed and Jeon, 2015; Masteri-Farahani and Askari, 2019).

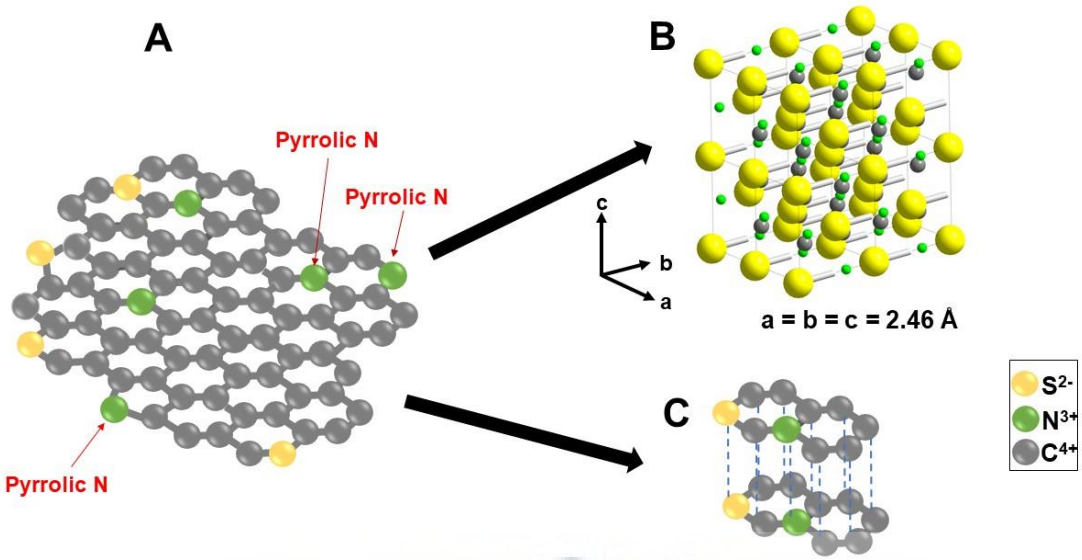

Figure 6.13: The modelled (using Endeavour software) proposed structure of the S,N-doped graphene primitive cubic, A shows the top view of bi-layer graphene rings and B shows the a side-view of the structure and C shows the interaction between the two graphene layers.

The sharp peaks on the XRD spectra correspond to the SAED image obtained from TEM microscope showing diffractive patterns of a crystalline sample and corresponding miller indexes for a primitive cubic. Further analysis of the materials using the inserted selected area diffraction (SAED) micrograph shows a pattern of a hexagonal crystal structure. Bright rings with solid lines describing the hexagonal structure are easy to observe. When a single layer graphene is used, an appearance of 6 distinguishable points would be observed on each ring (Aldana, Velandia and Hurtado-Morales, 2019; Ma *et al.*, 2020). However, the results obtained from Raman analysis have already outlined the number of layers on each material prepared in this study, hence the appearance of solid lines on the ring. The first bright ring is ascribed to the [002] reflection plane, while the second is ascribed to the [100] and

the third bright ring is ascribed to the [101] reflection plane. These three signals are clues for a hexagonal graphene structure.

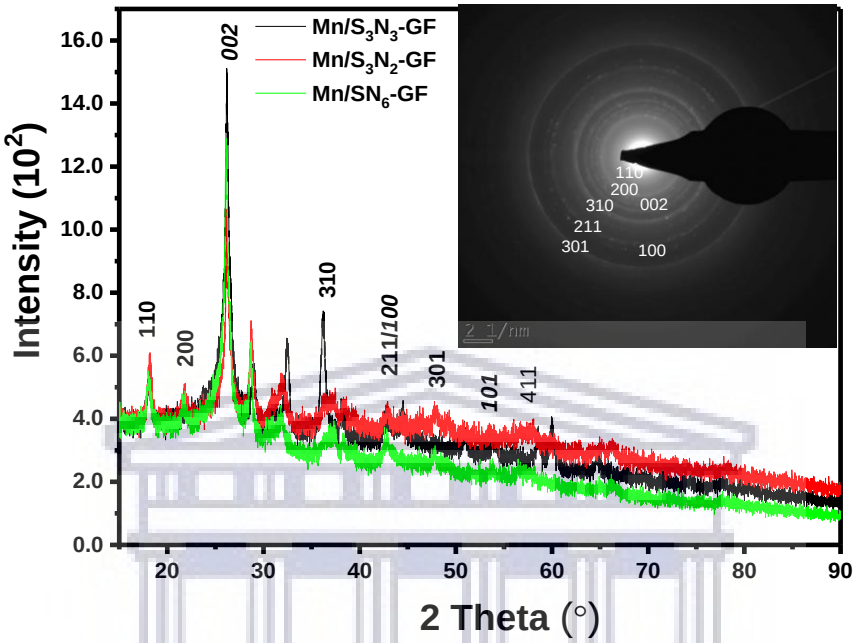

Figure 6.14: XRD of graphene sheets and graphene loaded with manganse spinel oxide.

Incorporation of the Mn_2O_3 metal oxide on S,N-doped graphene changed the crystal structure from a primitive cubic to a body-centered cubic. This is influenced by the fact that cobalt metal naturally exist as a body-centered cubic which then distorts the structure of graphene to take on the dominating cobalt structure. The XRD peaks observed at 18.2°, 21.7°, 36.2°, 42.8°, 47.7°, 57.7° correcspond to 110, 200, 310, 211, 301 and 411 XRD crystal planes of Mn_2O_3 which are in agreement with reported reflections (JCPDS 71-0636) (Shah *et al.*, 2018; Yao *et al.*, 2018).

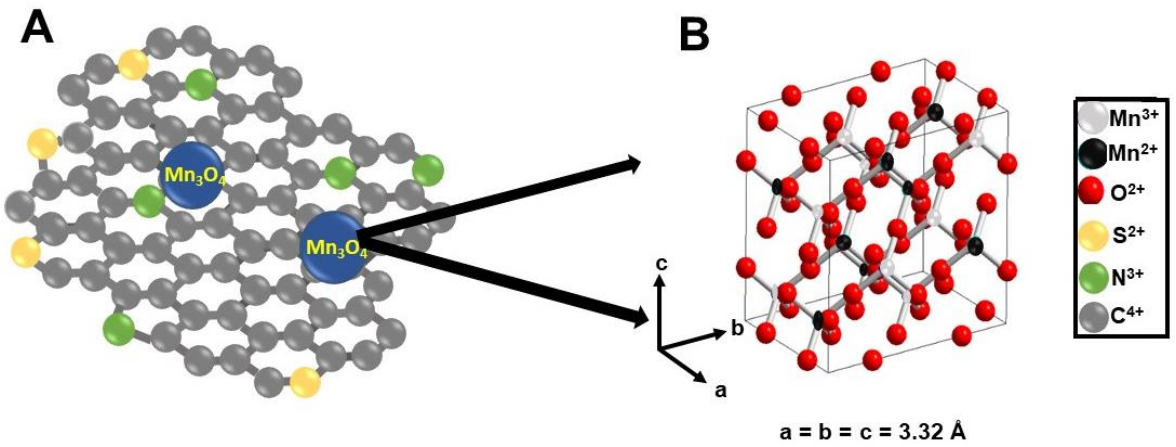

Figure 6.15: The modelled (using Endeavour software) proposed structure of the Mn/S,N-graphene; A is the top-view of the material with Mn_3O_4 sandwitched in between, while B is the side-view model of Mn_3O_4 that is ontop of the graphene material.

Further analysis of the crystal structure of the prepared materials using SAED (insert on **Figure 6.14**) shows the presence of a polycrystalline body centred cubic in accordance with XRD results. The presence of the bright rings which correspond to [002], [100] and [101] reflection planes are due to the presence of graphene in the structure as already outline in **Figure 6.12**. The other bright rings observed which corresponding to [111], [200], [310], [211] and [301] are due to the presence of Mn(II) and Mn(III) in the multivalence/polycrystalline structure of the Mn_2O_3 spinel oxide structure (Hoseini *et al.*, 2019; Kang *et al.*, 2019).

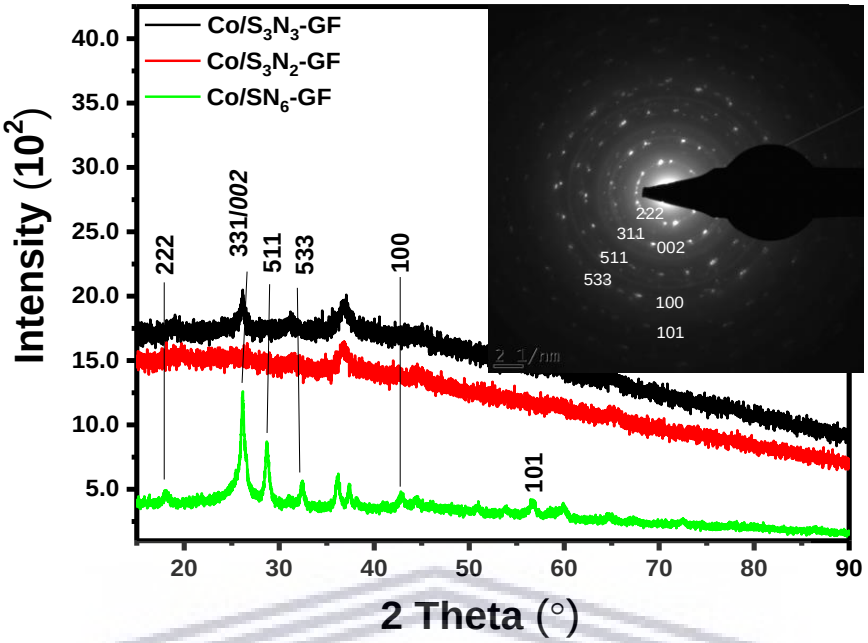

Figure 6.16: XRD of graphene sheets and graphene loaded with cobalt spinel oxide

Figure 6.16 shows the XRD patterns of S,N-doped grapheme with loaded with Co_3O_4 metal oxides. The intensely sharp XRD peaks of Co/SN_6-GF and the dotted diffractions on the SAED image signify that the sample is highly crystalline as compared to the others. However, the crystal structure obtained from the XRD characterization technique is a face-centred cubic as shown in **Figure 6.17**. This is supported by the appearance of peaks at 18.1°, 26.2°, 28.7° and 32.5° which correspond to the 222, 331, 511 and 533 crystal planes (Shi *et al.*, 2018; Xiao *et al.*, 2018).

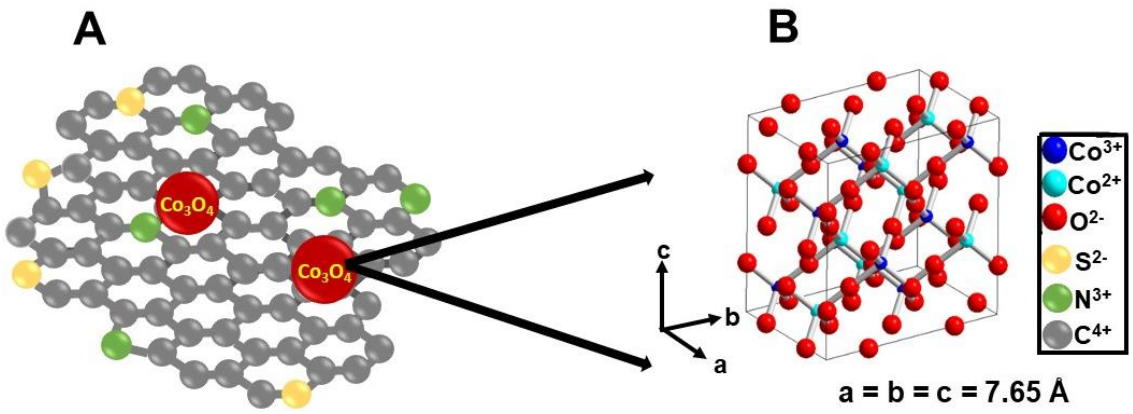

Figure 6.17: The modelled (using Endeavour software) proposed structure of the Mn/S,N-graphene; A is the top-view of the material with Mn_3O_4 sandwitched in between, while B is the side-view model of Mn_3O_4 that is ontop of the graphene material.

Further analysis of the crystal structure of the prepared materials using SAED (insert on **Figure 6.17**) shows the presence of a polycrystalline face centred cubic in accordance with XRD results. The presence of the bright rings which correspond to [002], [100] and [101] reflection planes are due to the presence of graphene in the structure as already outline in **Figure 6.12**. The other bright rings observed which corresponding to [222], [311], [511] and [533] are due to the presence of Co(II) and Co(III) in the multivalence/polycrystalline structure of the Co_3O_4 spinel structure (Fang *et al.*, 2019; Moridon *et al.*, 2019).

6.4 Material application

6.4.1 Cyclic voltammetry

The electro-catalytic activity of the prepared Co_3O_4/Mn_2O_3 on S,N-doped graphene towards oxygen reduction reactions (ORR) was initially evaluated using cyclic voltammetry in oxygen saturated 0.1 M KOH solution.

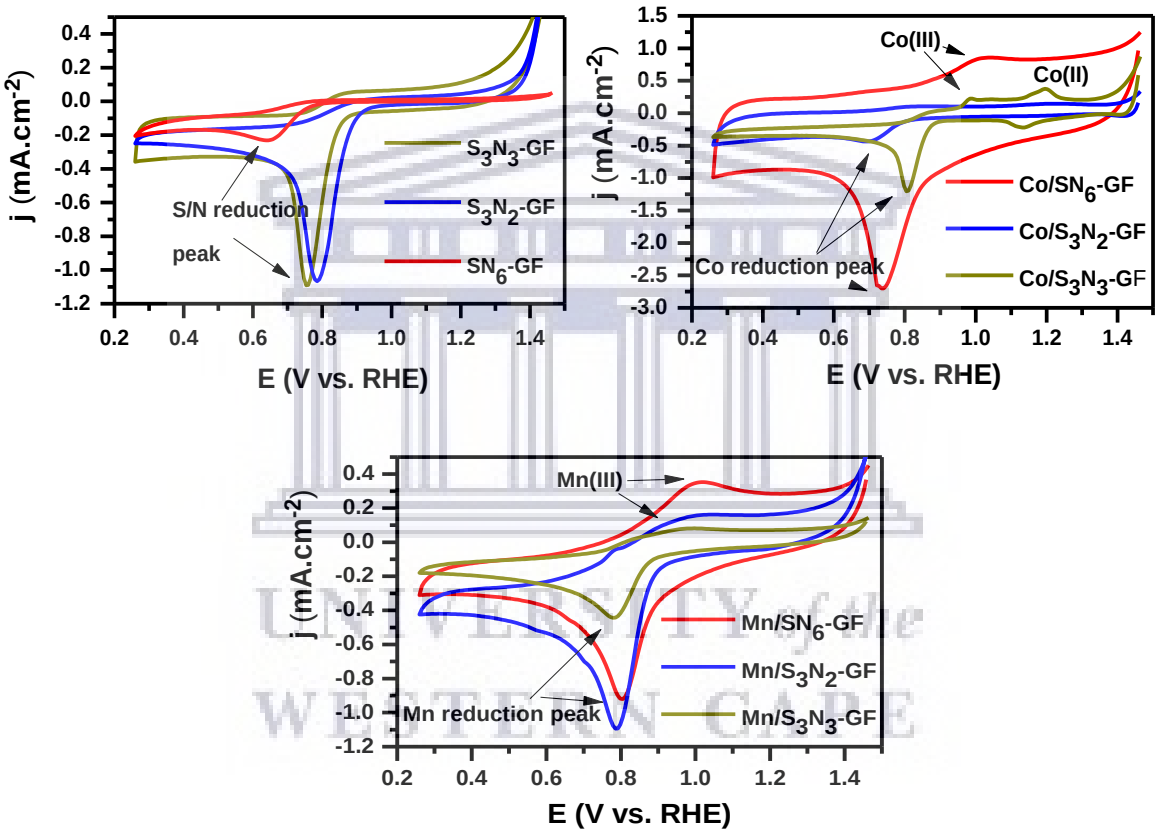

Figure 6.18: Cyclic voltammetry of graphene sheets and graphene loaded with cobalt and manganse metals.

Figure 6.18 shows the CV of the prepared materials and it can be observed from the voltammograms that they all exhibit well-defined cathodic peaks centred at the potential values presented in **Table 6.2** when the electrolyte solution is saturated with oxygen (Cai *et al.*, 2018; Wang *et al.*, 2018; Liu *et al.*, 2019). All the S,N-GF

materials show an irreversible reduction peak around 0.65 to 0.78 V (**Table 6.2**) due to the production of H_2O from O_2 molecules on the surface of the catalysts. The presence of sulphur and nitrogen on the surface of the materials serve as catalytic active centres for the ORR. In the presence of the spinel metal oxides (Mn_3O_4 and Co_3O_4), reduction peaks are observed due to the reduction of O_2 to H_2O while the oxidation peaks observed are due to the oxidation of the spinel metal oxides. The high current densities of the Co/SN_6-GF sample prove it a better electrocatalyst compared to the others. However, the high peak potential Co/S_3N_3-GF renders it more favourable for application in ORR. Nonetheless, the addition spinel cobalt metal oxide shows better catalytic efficiencies compared to the other electrocatalysts. Therefore, the order of catalytic efficiencies according to CV results is; Co/S,N-GF > Mn/S,N-GF > S,N-GF. The comparably high onset potential of Co/SN-GF than the Mn/SN-GF and SN-GF highlights the essential role of Co to boost the ORR activity of S_3N_2-GF electrocatalyst, owing to the synergistic effect from the bimetal activation on SN-GF and improved porosity. A study by Ming Li *et al.* (2017) shows that the concentration of Co^{2+} on N-doped graphene influences the ORR catalytic activity on the catalysts. For lower (0.1 mM) or higher (10 mM) Co^{2+} concentration, the resulting materials show improved ORR catalytic activity compared to N-doped graphene, but both inferior to that obtained with 1 mM Co^{2+} in terms of peak potential and onset potential (Ming Li *et al.*, 2017).

Table 6.2: Summary of the electrochemical results from CV

Sample	J ($mA.cm^{-2}$)	Potential (V vs RHE)
S_3N_3-GF	-1.07	0.75
S_3N_2-GF	-1.03	0.78
SN_6-GF	-0.26	0.65
Co/S_3N_3-GF	-1.11	0.81
Co/S_3N_2-GF	-0.44	0.70
Co/SN_6-GF	-2.74	0.74
Mn/S_3N_3-GF	-0.44	0.78
Mn/S_3N_2-GF	-1.08	0.79
Mn/SN_6-GF	-0.91	0.81

6.4.2 Linear sweet voltammetry

To gain further insight into the kinetics of ORR on the metal/S,N-GF samples, LSV curves were acquired at 1600 rpm in O_2-saturated KOH solution at 5 $mV.s^{-1}$ in comparison to the state-of-the-art PtC catalysts (**Figure 6.19**).

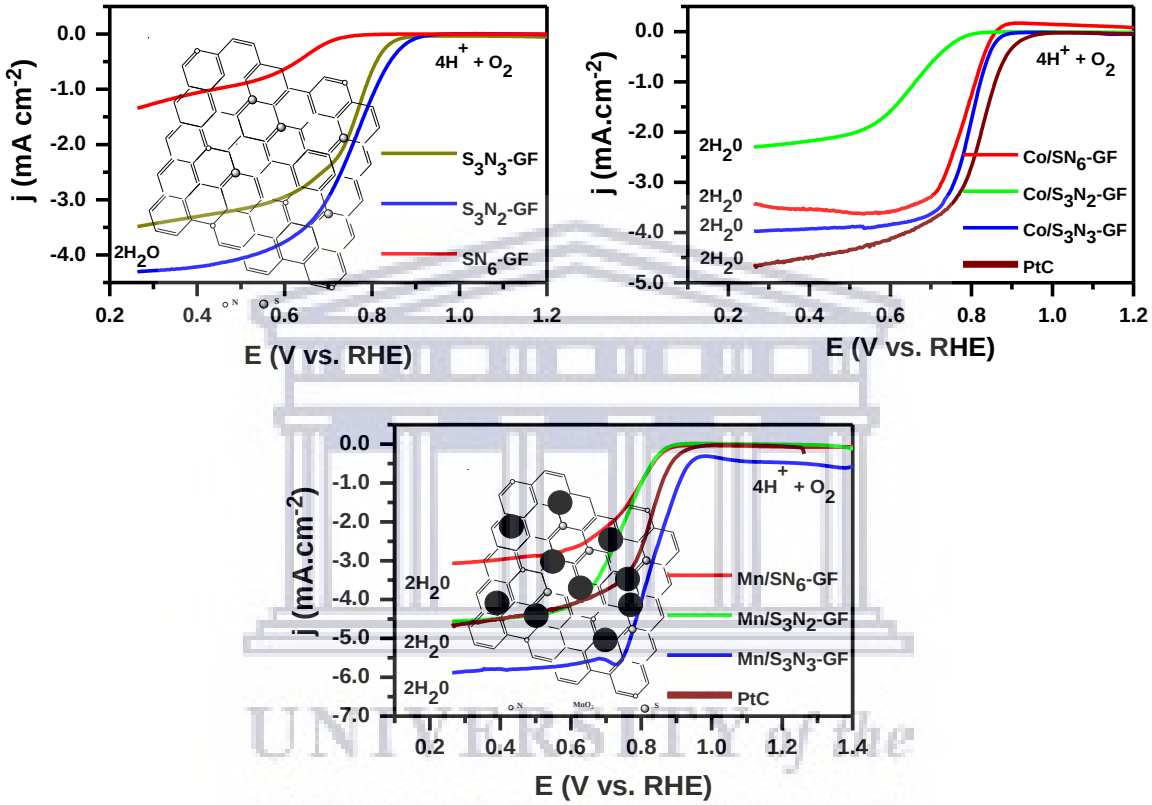

Figure 6.19: Liner sweep voltammetry of graphene sheets and graphene loaded with cobalt and manganse metals.

The highest diffusion-limiting current density ($j_{L,\ 0.26\ V,\ 1600\ rpm}$) was achieved with the Mn/S_3N_3-GF nanocomposite (-5.86 $mA.cm^{-2}$), followed by PtC (-4.62 $mA.cm^{-2}$) and the rest is presented in **Table 6.3**. The onset potential of the S_3N_2-GF electrocatalysts shifted to negative potentials upon addition of Co_3O_4 spinel metal oxide, signifying a comparatively lower onset potential. This low catalytic activity can be ascribed to the e^--h^+ recombination observed on Raman spectra and the

agglomerated particles on TEM. However, addition of Mn_3O_4 on S_3N_2-GF shows improved catalytic activity comparable to that of PtC. The order of catalytic activity according to LSV results is as follows; Mn/SN-GF > PtC>SN-GF > Co/SN-GF. The observed electrochemical test results of the Mn/SN-GF catalysts suggest the importance of the sulphur/nitrogen dual doped carbon to push the ORR activity closer to the benchmark PtC. The enhanced activity of Mn/SN-GF catalyst is attributed to (i) the synergetic interaction between the metal oxide nanoparticles and sulphur/nitrogen dual doped carbon and (ii) the unique structure of the catalyst that is strongly resistant toward self-accumulation and detachment of nanoparticles, as confirmed by TEM and the durability tests below.

Table 6.3: Summary of the electrochemical results from LSV

Sample	J ($mA.cm^{-2}$)	Potential (V vs RHE)
S_3N_3-GF	-3.47	0.26
S_3N_2-GF	-4.27	0.26
SN_6-GF	-1.33	0.26
Co/S_3N_3-GF	-3.93	0.26
Co/S_3N_2-GF	-2.24	0.26
Co/SN_6-GF	-3.44	0.26
Mn/S_3N_3-GF	-5.86	0.26
Mn/S_3N_2-GF	-4.57	0.26
Mn/SN_6-GF	-3.13	0.26
PtC	-4.62	0.26

6.4.3 Methanol stability tests

The application of electrocatalysts as cathode electrodes in DMFCs is dependent on their tolerance to the methanol crossover. Methanol from the anode may permeate through the polymer membrane to the cathode, causing severe decay in the performance of the catalyst for the ORR due to the use of active sites for methanol oxidation and progressive CO poisoning of the catalyst surfaces (Ye *et al.*, 2015; Yasmin, Cho and Jeon, 2018). To test methanol crossover effect O_2 and fuel molecules (methanol) were introduced into the electrolyte and the stability test results are presented in **Figure 6.20**.

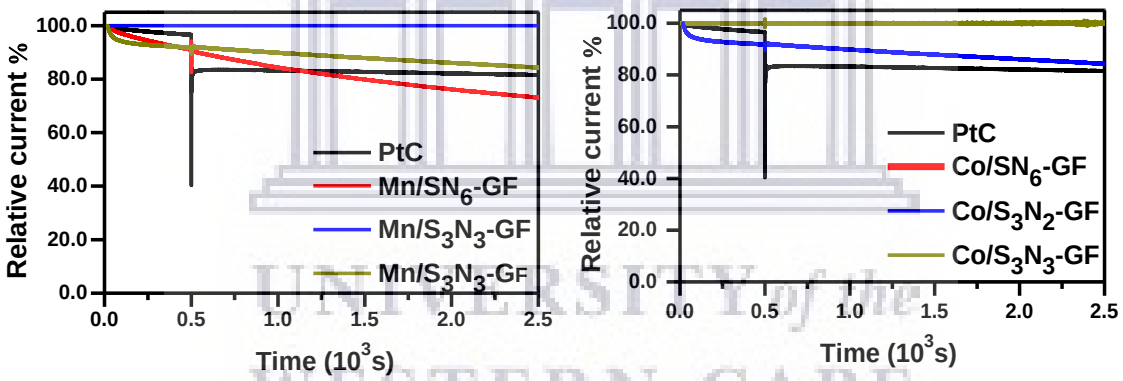

Figure 6.20: Methanol tolerance tests of graphene sheets and graphene loaded with cobalt and manganse metals.

The addition of methanol in the presence of PtC catalysts causes a current decrease of 17%. A current decrease of about 0.07%, 5.70% and 0.07% is observed for Co/S_3N_3-GF, Co/S_3N_2-GF and Co/SN_6-GF, respectively. In the presence of Mn_3O_4, a current decrease of 5.70%, 0.04% and 6.84% was observed for Mn/S_3N_3-GF, Mn/S_3N_2-GF and Mn/SN_6-GF, respectively. These results show that the presence of Co_3O_4 in SN-GF catalysts improves the stability of the electrocatalysts. However,

all the electrocatalyst show more tolerant to methanol compared to that of the state-of-the-art PtC catalyst.

6.4.4 Durability tests

The durability of ORR catalysts is a parameter that determines the lifetime of a fuel cell. The stability of the metal oxide loaded N-doped graphene was measured using RDE chronoamperometry under steady-state mass transport conditions (0.65 V vs RHE).

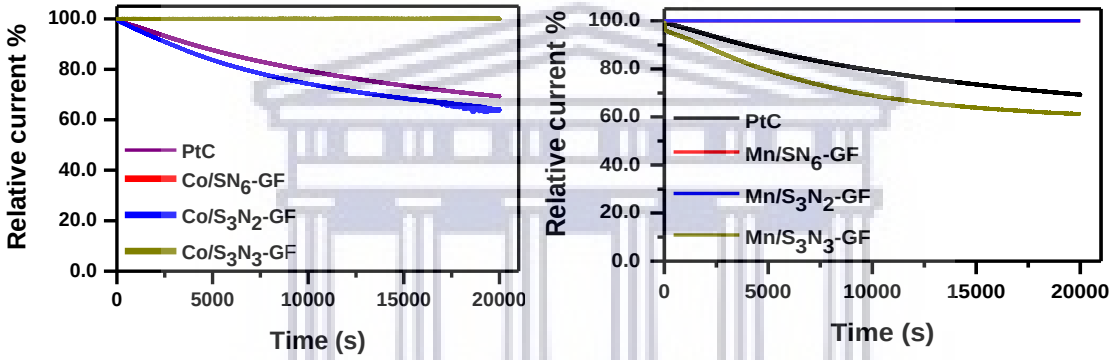

Figure 6.21: Durability tests of graphene sheets and graphene loaded with cobalt and manganse metals.

Figure 6.21 shows the stability of the metal oxide/S,N-doped graphene catalysts against the state-of-the-art PtC. From the above results, the state-of-the-art PtC catalyst shows 70.22% durability after 20 000 s. The durability of 100%, 63.98% and 100% was observed for Co/S_3N_3-GF, Co/S_3N_2-GF and Co/SN_6-GF electrocatalysts, respectively. Those of Mn/S_3N_3-GF, Mn/S_3N_2-GF and Mn/SN_6-GF were found to be 61.31%, 99.61% and 99.61, respectively. These results prove the presence of Co_3O_4 to improve the durability and stability of the S,N-doped graphene catalysts.

6.5 Conclusion

The synthesis of metal oxide (Mn_3O_4 and Co_3O_4) impregnated S,N-GF electrocatalyst with enhanced electrochemical properties towards ORR was reported in this Chapter using simple, scalable and cost-effective solid solution processes. This was supported by the appearance of the N-O, C-S and N-H vibrational bands on FTIR spectroscopy. When the S,N-doped graphene was further loaded with the Mn_2O_3 and Co_3O_4 metal oxides, the CoO, CoOH, MnOH and MnO vibrational band were observed on FTIR, signifying the success of the process. The structural characterisation of the prepared materials is further authenticated by using Raman spectroscopy where the appearance of the D and G bands signify that the graphitic structure of graphene was reserved after addition of the metal oxides. The T_{2g}, E_g, N_1 and N_2 vibrational bands for Co_2O_3 and those of MnO_2 and MnOOH observed on Raman spectroscopy further signify that the metal oxides were loaded on the graphene structures. The XRD and TEM results further confirmed the structure of the prepared nanomaterials, concurrent with the results already obtained from the other characterisation techniques to confirm the structure of the materials. Electrocatalytic testing of the nanomaterials for the ORR using linear sweep voltammetry proved the manganese oxide containing graphene materials, Co/S_3N_3-GF, the best ORR electrocatalyst compared to the state-of-the-art PtC electrocatalysts. However, when the durability and methanol stability tests were conducted on these catalysts, the Co/SN-GF showed better stability and durability as compared to the other electrocatalyst. These findings imply that the Co/SN-GF electrocatalysts behave better than the commercial PtC catalysts. Therefore, it may

be concluded that they have the potential to replace the expensive PtC catalysts in fuel cells.

References

Alegre, C. *et al.* (2018) 'NiCo-loaded carbon nanofibers obtained by electrospinning: Bifunctional behavior as air electrodes', *Renewable Energy*, 125, pp. 250–259.

Álvarez-Docio, C. M. *et al.* (2019) 'Investigation of thermal stability of 2D and 3D CoAl2O4 particles in core-shell nanostructures by Raman spectroscopy', *Journal of Alloys and Compounds*, 779, pp. 244–254.

Aldana, C., Velandia, F. and Hurtado-Morales, M. (2019) 'Synthesis of graphene and MoS2 and their characterization using microscopy and spectroscopy techniques', *Materials Today: Proceedings*. Elsevier Ltd, 14, pp. 130–133.

Anh, N. T. N., Chowdhury, A. D. and Doong, R. (2017) 'Highly sensitive and selective detection of mercury ions using N, S-codoped graphene quantum dots and its paper strip based sensing application in wastewater', *Sensors and Actuators B: Chemical*, 252, pp. 1169–1178.

Bezerra, C. W. B. *et al.* (2008) 'A review of Fe–N/C and Co–N/C catalysts for the oxygen reduction reaction', *Electrochimica Acta*, 53, pp. 4937–4951.

Cai, D. *et al.* (2018) 'Facile synthesis of N and S co-doped graphene sheets as anode materials for high-performance lithium-ion batteries', *Journal of Alloys and Compounds*, 731, pp. 235–242.

Carrillo-Rodríguez, J. C. *et al.* (2017) 'Easy synthesis of N-doped graphene by milling exfoliation with electrocatalytic activity towards the Oxygen Reduction Reaction (ORR)', *International Journal of Hydrogen Energy*, 42, pp. 30383–30388.

Chen, W. *et al.* (2018) 'Origins of high onset overpotential of oxygen reduction reaction at Pt-based electrocatalysts: A mini review', *Electrochemistry Communications,* 96, pp. 71–76.

Cheng, Y. *et al.* (2018) 'The shape effect of manganese(II,III) oxide nanoparticles on the performance of electrochemical capacitors', *Electrochimica Acta*, 284, pp. 408–417.

Choe, J. E., Ahmed, M. S. and Jeon, S. (2015) '3,4-Ethylenedioxythiophene functionalized graphene with palladium nanoparticles for enhanced electrocatalytic oxygen reduction reaction', *Journal of Power Sources*, 281, pp. 211–218.

Davodi, F. *et al.* (2018) 'Catalyst Support Effect on the Activity and Durability of Magnetic Nanoparticles: Toward Design of Advanced Electrocatalyst for Full Water Splitting', *ACS Applied Materials and Interfaces*, 10, pp. 31300–31311.

Deng, H. *et al.* (2018) 'Silver incorporated into cryptomelane-type Manganese oxide boosts the catalytic oxidation of benzene', *Applied Catalysis B: Environmental*, 239, pp. 214–222.

Ejaz, A. and Jeon, S. (2018) 'The individual role of pyrrolic, pyridinic and graphitic nitrogen in the growth kinetics of Pd NPs on N-rGO followed by a comprehensive study on ORR', *International Journal of Hydrogen Energy*, 43, pp. 5690–5702.

Fang, D. *et al.* (2019) 'Cobalt oxide nanoparticles anchored on discharged-graphene film for lithium-ion battery', *Solid State Ionics*, 340, p. 115006.

Gan, L. *et al.* (2013) 'Understanding and Controlling Nanoporosity Formation for Improving the Stability of Bimetallic Fuel Cell Catalysts', *Nano Letters*, 13, pp. 1131–1138.

Gebremariam, T. T. *et al.* (2018) 'Bimetallic Mn-Co oxide nanoparticles anchored on carbon nanofibers wrapped in nitrogen doped carbon for application in Zn-air batteries and Supercapacitors', *ACS Applied Energy Materials*, 1, pp. 1612–1625.

Giarratano, F. *et al.* (2018) 'Nanoporous Pt-based catalysts prepared by chemical dealloying of magnetron-sputtered Pt-Cu thin films for the catalytic combustion of

hydrogen', *Applied Catalysis B: Environmental*, 235, pp. 168–176.

Gupta, S. *et al.* (2016) 'Bifunctional Perovskite Oxide Catalysts for Oxygen Reduction and Evolution in Alkaline Media', *Chemistry - An Asian Journal*, 11, pp. 10–21.

Hoseini, S. *et al.* (2019) 'Application of plasma technology in the removal of volatile organic compounds (BTX) using manganese oxide nano-catalysts synthesized from spent batteries', *Journal of Cleaner Production*, 232, pp. 1134–1147.

Jiang, S. *et al.* (2018) '3D porous cellular NiCoO2/graphene network as a durable bifunctional electrocatalyst for oxygen evolution and reduction reactions', *Journal of Power Sources*, 399, pp. 66–75.

Jiang, X. *et al.* (2018) 'Raman analysis of cobalt blue pigment in blue and white porcelain: A reassessment', *Spectrochimica Acta Part A: Molecular and Biomolecular Spectroscopy*, 190, pp. 61–67.

Kang, L. *et al.* (2019) 'A new strategy for synthesis of hierarchical MnO2–Mn3O4 nanocomposite via reduction-induced exfoliation of MnO2 nanowires and its application in high-performance asymmetric supercapacitor', *Composites Part B: Engineering*, xxx, p. 107501.

Khandelwal, M. *et al.* (2018) 'Chemically controlled in-situ growth of cobalt oxide microspheres on N,S-co-doped reduced graphene oxide as an efficient electrocatalyst for oxygen reduction reaction', *Journal of Power Sources*, 407, pp. 70–83.

Li, C. *et al.* (2018) 'Emerging Pt-based electrocatalysts with highly open nanoarchitectures for boosting oxygen reduction reaction', *Nano Today*, 21, pp. 91–105.

Li, J. *et al.* (2018) 'Surface decorated cobalt sulfide as efficient catalyst for oxygen evolution reaction and its intrinsic activity', *Journal of Catalysis*, 367, pp. 43–52.

Liu, X. *et al.* (2019) 'Wet-chemistry grafted active pyridinic nitrogen sites on holey graphene edges as high performance ORR electrocatalyst for Zn-Air batteries', *Materials Today Energy*, 11, pp. 24–29.

Aldana, C., Velandia, F. and Hurtado-Morales, M. (2019) 'Synthesis of graphene and MoS2 and their characterization using microscopy and spectroscopy techniques', *Materials Today: Proceedings*. Elsevier Ltd, 14, pp. 130–133.

Fang, D. *et al.* (2019) 'Cobalt oxide nanoparticles anchored on discharged-graphene film for lithium-ion battery', *Solid State Ionics*, 340, p. 115006.

Hoseini, S. *et al.* (2019) 'Application of plasma technology in the removal of volatile organic compounds (BTX) using manganese oxide nano-catalysts synthesized from spent batteries', *Journal of Cleaner Production*, 232, pp. 1134–1147.

Kang, L. *et al.* (2019) 'A new strategy for synthesis of hierarchical MnO2–Mn3O4 nanocomposite via reduction-induced exfoliation of MnO2 nanowires and its application in high-performance asymmetric supercapacitor', *Composites Part B: Engineering*, xxx, p. 107501.

Ma, F. *et al.* (2020) 'Rapid production of few layer graphene for energy storage via dry exfoliation of expansible graphite', *Composites Science and Technology*, 185, p. 107895.

Mamtani, K. *et al.* (2018) 'Insights into oxygen reduction reaction (ORR) and oxygen evolution reaction (OER) active sites for nitrogen-doped carbon nanostructures (CNx) in acidic media', *Applied Catalysis B: Environmental*, 220, pp. 88–97.

Mani, V. *et al.* (2015) 'Synthesis and characterization of graphene-cobalt

phthalocyanines and graphene-iron phthalocyanine composites and their enzymatic fuel cell application', *Renewable Energy*, 74, pp. 867–874.

Masteri-Farahani, M. and Askari, F. (2019) 'Design and photophysical insights on graphene quantum dots for use as nanosensor in differentiating methamphetamine and morphine in solution', *Spectrochimica Acta Part A: Molecular and Biomolecular Spectroscopy*, 206, pp. 448–453.

Mauricio-Sánchez, R. A. *et al.* (2018) 'FTIR spectroscopy studies on the spontaneous neutralization of chitosan acetate films by moisture conditioning', *Vibrational Spectroscopy*, 94, pp. 1–6.

McKerracher, R. D. *et al.* (2016) 'A high-performance, bifunctional oxygen electrode catalysed with palladium and nickel-iron hexacyanoferrate', *Electrochimica Acta*, 206, pp. 127–133.

Mei, J. *et al.* (2018) 'Ordered mesoporous spinel Co3O4 as a promising catalyst for the catalytic oxidation of dibromomethane', *Molecular Catalysis*, 461, pp. 60–66.

Ming Li, C. *et al.* (2017) ' One-pot synthesis of Co/N-doped mesoporous graphene with embedded Co/CoO x nanoparticles for efficient oxygen reduction reaction ', *Nanoscale*, 9, pp. 10233–10239.

Moridon, S. N. F. *et al.* (2019) 'Cobalt oxide as photocatalyst for water splitting: Temperature-dependent phase structures', *International Journal of Hydrogen Energy*, 44, pp. 25495–25504.

Mohammed, I. *et al.* (2018) 'Electropolymerized film of cobalt tetrabenzimidazolephthalocyanine for the amperometric detection of H2O2', *Journal of Electroanalytical Chemistry*, 826, pp. 96–103.

Mukherjee, M. *et al.* (2018) 'One pot solvothermal synthesis of ZnPc nanotube and its composite with RGO: A high performance ORR catalyst in alkaline medium',

Applied Surface Science, 449, pp. 144–151.

Park, J. E. *et al.* (2018) 'Graphitic carbon nitride-carbon nanofiber as oxygen catalyst in anion-exchange membrane water electrolyzer and rechargeable metal–air cells', *Applied Catalysis B: Environmental*, 237, pp. 140–148.

Petit, T. and Puskar, L. (2018) 'FTIR spectroscopy of nanodiamonds: Methods and interpretation', *Diamond and Related Materials*, 89, pp. 52–66.

Pourazadi, E. *et al.* (2018) 'Identification of electrocatalytic oxygen reduction (ORR) activity of boron in graphene oxide; incorporated as a charge-adsorbate and/or substitutional p-type dopant', *Materials Chemistry and Physics*, 207, pp. 380–388.

Qian, L. *et al.* (2015) 'Trinary Layered Double Hydroxides as High-Performance Bifunctional Materials for Oxygen Electrocatalysis', *Advanced Energy Materials*, 5, p. 1500245.

Qu, K. *et al.* (2016) 'Graphene oxide-polydopamine derived N, S-codoped carbon nanosheets as superior bifunctional electrocatalysts for oxygen reduction and evolution', *Nano Energy*, 19, pp. 373–381.

Sadhasivam, T. *et al.* (2018) 'Electro-analytical performance of bifunctional electrocatalyst materials in unitized regenerative fuel cell system', *International Journal of Hydrogen Energy*, 43, pp. 18169–18184.

Shah, H. U. *et al.* (2018) 'Hydrothermal synthesis of reduced graphene oxide-Mn3O4 nanocomposite as an efficient electrode materials for supercapacitors', *Ceramics International*, 44, pp. 3580–3584.

Shahedi Asl, M., Nayebi, B. and Shokouhimehr, M. (2018) 'TEM characterization of spark plasma sintered ZrB2–SiC–graphene nanocomposite', *Ceramics International*, 44, pp. 15269–15273.

Sheikhshoaie, I., Ramezanpour, S. and Khatamian, M. (2017) 'Synthesis and

characterization of thallium doped Mn3O4 as superior sunlight photocatalysts', *Journal of Molecular Liquids*, 238, pp. 248–253.

Shi, X. *et al.* (2018) 'Facile synthesis of magnetic Co3O4/BFO nanocomposite for effective reduction of nitrophenol isomers', *Chemosphere,* xxx, pp. 914-922.

Singu, B. S. and Yoon, K. R. (2019) 'Exfoliated graphene-manganese oxide nanocomposite electrode materials for supercapacitor', *Journal of Alloys and Compounds*, 770, pp. 1189–1199.

Surya, K., Michael, M. S. and Prabaharan, S. R. S. (2018) 'A review on advancement in non-noble metal based oxides as bifunctional catalysts for rechargeable non-aqueous Li/air battery', *Solid State Ionics*, 317, pp. 89–96.

Tafen, D. N., Kauffman, D. R. and Alfonso, D. R. (2018) 'Electrocatalytic oxygen evolution with pure and substituted M6(SR)12 (M = Pd, Fe, Rh) complexes', *Computational Materials Science*, 150, pp. 283–290.

Tang, X. and Ng, H. Y. (2017) 'Cobalt and nitrogen-doped carbon catalysts for enhanced oxygen reduction and power production in microbial fuel cells', *Electrochimica Acta*, 247, pp. 193–199.

Tian, H. *et al.* (2017) 'N, S co-doped graphene quantum dots-graphene-TiO2 nanotubes composite with enhanced photocatalytic activity', *Journal of Alloys and Compounds*, 691, pp. 369–377.

Velasco-Vélez, J. J. *et al.* (2018) 'Electrochemically active Ir NPs on graphene for OER in acidic aqueous electrolyte investigated by in situ and ex situ spectroscopies', *Surface Science*, 861, pp.1-8.

Wang, Y. *et al.* (2018) 'Co3O4@g-C3N4 supported on N-doped graphene as effective electrocatalyst for oxygen reduction reaction', *International Journal of Hydrogen Energy*, 43, pp. 20687–20695.

Weisz, A. D. *et al.* (2002) 'FTIR study of the adsorption of single pollutants and mixtures of pollutants onto titanium dioxide in water : oxalic and salicylic acids', *Catalysis Today,* 76, pp. 103–112.

Wu, F. *et al.* (2018) 'Exploring the role of cobalt in promoting the electroactivity of amorphous Ni-B nanoparticles toward methanol oxidation', *Electrochimica Acta*, 287, pp. 115–123.

Xiao, B. *et al.* (2018) 'A green and facile synthesis of Co3O4 monolithic catalyst with enhanced total oxidation of propane performance', *Catalysis Communications*, 116, pp. 1–4.

Xu, S. *et al.* (2017) 'Building upon the Koutecky-Levich Equation for Evaluation of Next-Generation Oxygen Reduction Reaction Catalysts', *Electrochimica Acta*, 255, pp. 99–108.

Yao, J. *et al.* (2018) 'Reduced graphene oxide/Mn3O4 nanohybrid for high-rate pseduocapacitive electrodes', *Journal of Colloid and Interface Science*, 511, pp. 434–439.

Yasmin, S., Cho, S. and Jeon, S. (2018) 'Electrochemically reduced graphene-oxide supported bimetallic nanoparticles highly efficient for oxygen reduction reaction with excellent methanol tolerance', *Applied Surface Science*, 434, pp. 905–912.

Ye, D. *et al.* (2015) 'Co-calcination-derived Pd budded in N-Doped Ordered Mesoporous Graphitic Carbon Nanospheres for Advanced Methanol-tolerant Oxygen Reduction', *Electrochimica Acta*, 160, pp. 306–312.

Yun, M., Ahmed, M. S. and Jeon, S. (2015) 'Thiolated graphene oxide-supported palladium cobalt alloyed nanoparticles as high performance electrocatalyst for oxygen reduction reaction', *Journal of Power Sources*, 293, pp. 380–387.

Zaghrioui, M. *et al.* (2018) 'Raman study of high temperature insulator-insulator

transition in Ba2Co9O14', *Solid State Sciences*, 79, pp. 1–5.

Zaman, W. Q. *et al.* (2018) 'Iridium Substitution in Nickel Cobaltite Renders High Mass Specific OER Activity and Durability in Acidic Media', *Applied Catalysis B: Environmental*, xxx, pp.295-302.

Zhang, B. *et al.* (2017) 'Highly active and stable non noble metal catalyst for oxygen reduction reaction', *International Journal of Hydrogen Energy*, 42, pp. 10423–10434.

Zhang, J. *et al.* (2015) 'A metal-free bifunctional electrocatalyst for oxygen reduction and oxygen evolution reactions', *Nature Nanotechnology*, 10, pp. 444–452.

Zhang, X. *et al.* (2018) 'Bifunctional CoNx embedded graphene electrocatalysts for OER and ORR: A theoretical evaluation', *Carbon*, 130, pp. 112–119.

CHAPTER 7

Conclusive summary

7.1 Conclusions (Project 1)

Based on the aims and objectives of this study in the dissertation, it can be concluded that this study was conducted successfully, and some important breakthroughs were made. The main aim of this study was to strategically prepare band gap-engineered graphene quantum dot (GQD) structures at different synthetic temperatures. As was seen in Chapter 3, these band-gap engineered GQDs were prepared in such a way that they match the different energies of the visible region in the solar spectrum. Thereafter, in Chapter 4, these band gap engineered GQD structures were used as donor materials to create “rainbow” Schottky junction solar cells, targeting all the energies in the visible region of the solar spectrum for improved solar-to-electricity power conversion efficiency. Structural characterisation of the prepared GQD nanomaterials (Chapter 3) under SS-^{13}C-NMR showed appearance of bands at 40 ppm due to the presence of sp^3 hybridised carbon atoms from the peripheral region of the GQD structures. Other bands were observed at 130 ppm due to the presence of polycyclic aromatic carbon atoms from the benzene rings of the GQD backbone, and around 180 ppm due to the presence of carboxylic acid carbons from oxidation due to moisture. FTIR spectroscopy further confirmed the presence of aromatic carbon atoms and oxidised carbons, concurrent with SS-^{13}C-NMR results. The effect of synthesis temperature on the electronic structure of the nanomaterials was evaluated under TEM, UV-vis spectroscopy, PL and electrochemical studies. A reduction in the particle size was observed on TEM with increasing synthesis temperature, suggesting a shift/change in the electronic

structure of the quantum dots; i.e., electron confinement. The UV-vis spectroscopy showed appearance of n-π* and π-π* transitions due to the sp^2-hybridised carbons in GQD benzene ring backbones, supporting the FTIR and SS-NMR results. The observed blue-shift on the photoluminescence and UV-vis spectra with respect to increasing synthesis temperature (i.e., decreasing particle size) evidenced the quantum confinement effect and edge effects, which confirmed the existence of quantum dot structures in the samples. The obtained band gaps from the optical and electrochemical results were; 0.99 eV, 1.08 eV, 1.14 eV, 1.15 eV, 1.35 eV, 1.90 eV, 2.32 eV and 2.43 eV, all which prove to correspond to all energies in the visible region of the solar spectrum. To the best our knowledge, no study has reported the band gap engineered graphene quantum dot structures with absolute certainty and this makes this study (i.e., Chapter 3) unique.

The corresponding accepting materials (aluminium, Al; gold, Au and graphene, Gr metal nanoparticles) were prepared in the preceding chapter (Chapter 4) and then physically mixed with the GQD donor materials to create the charge-transfer complexes/Schottky junction (i.e., GQD:Al, GQD:Au and GQD:Gr). The interaction between the metal nanoparticles and semiconducting graphene quantum dots was evidenced by FTIR spectroscopy, XRD crystallographic analysis and PL spectroscopy. Morphological studies of the materials showed appearance of metal nanoparticles embedded on GQD structures, as anticipated. Quenching studies between the donor and acceptor (GQD and metal) at different metal ion concentrations, showed that the interaction followed both the static and dynamic quenching. This implies that there is good electron flow between the donor (GQD)

and the acceptor (metal ions). This was further confirmed by the low resistance observed on the Nyquist plots.

The Schottky junction photoactive films composed of graphene quantum dots (GQDs), Aluminium (Al), gold (Au) and graphene (Gr) metals have been prepared by spin coating to establish optimal concentration and composition of these materials of interest. Amongst the prepared donor to acceptor ratios of 1:1, 1:3. 1:6 and 3:1, the 1:3 ratio was found to possess optimal electrochemical efficiency and thus was used for fabrication of the solar cells. The metal/semiconductor Schottky junction solar cells were thereafter successfully prepared and characterized. Different concentrations (i.e., 10 mg/mL, 15 mg/mL and 20 mg/mL) of the active layer were prepared for optimisation of the solar cells. The optimal concentration was found to be 20 mg/mL (solar-to-electricity conversion efficiency of 1.02%) and was used to fabricate all other solar cell devices. When the solar cell devices were fabricated using the three different types of metals, the solar cell with GQD:Au as the active layer possessed high solar-to-electricity conversion efficiency upon light illumination. This can be subscribed to the reduction of the hot-electrons produced upon illumination by light. The results obtained in this study (solar-to-electricity conversion efficiency of 2.69%) are comparably close to the optimal Schottky junction solar cell, 3.8%. Therefore, this study was conducted successfully.

7.2 Conclusions (Project 2)

Work conducted during the international research visit proved Mn/S_3N_3-graphene electrocatalyst the best electrocatalyst for ORR compared to the state-of-the-art Pt/C catalyst. The Mn/S_3N_3-graphene showed high selectivity towards the ORR in the presence of methanol, possessed high stability during reproducibility tests and promise a reduction in cost in the price of fuel cells. The successful synthesis of the S,N-doped graphene electrocatalyst using solid solution processes was proven by the appearance of the N-O, C-S and N-H vibrational bands on FTIR spectroscopy. When the S,N-doped graphene was further loaded with the Mn_2O_3 and Co_3O_4 metal oxides, the CoO, CoOH, MnOH and MnO vibrational band were observed on FTIR, signifying the success of the process. The structural characterisation of the prepared materials is further authenticated by using Raman spectroscopy where the appearance of the D and G band signify that the graphitic structure of graphene was reserved after addition of the metal oxides. The T_{2g}, E_g, N_1 and N_2 vibrational bands for Co_2O_3 and those of MnO_2 and MnOOH observed on Raman spectroscopy further signify that the metal oxides were loaded on the graphene structures. The XRD and TEM images agreed with the results already obtained on the other characterisation techniques to confirm the structure of the materials. Application of the materials through linear sweep voltammetry proved the cobalt oxide containing graphene materials, Co/S_3N_2-GF, the best electrocatalyst for ORR. They also showed improved durability and methanol stability during ORR compared to the other electrocatalysts. These findings imply that the Co/SN-GF electrocatalysts behave better than the commercial PtC catalysts. Therefore, it may be concluded that they have the potential to replace the expensive PtC catalysts in fuel cells.

7.3 Recommendations (Project 1)

The optimal efficiency (3.8%) for Schottky junction solar cells reported thus far in literature has a different architecture from the one reported in this study. The recently reported Schottky junction solar cells employ an insulator in-between the metal and semiconductor, therefore, I would recommend introduction of an insulator on the solar cell architecture to reduce the production of hot electrons during solar conversion of the device.

The GQDs prepared in this study are biocompatible, photo-stable, with enhanced surface grafting and inherit superior electrical and mechanical properties from graphene. These features can greatly contribute to various state-of-the-art applications including: bio-imaging markers; fluorescent polymers; antibacterial, antifouling and disinfection systems; heavy metals, humidity and pressure sensors; batteries; flash memory devices and light emitting diodes.

APPENDIX

Table A1: Electrochemical efficiencies of graphene

Parameters					
Scan rate	J_{sc} (mA)	V_{oc} (V)	P_{max} (µW)	FF (%)	Ef (%)*e-3
10	0.067	0.025	1.162	68.5	0.24
20	0.121	31450	2.462	64.6	0.51
30	0.175	0.041	4.574	63.4	0.94
40	0.224	0.040	5.363	59.8	1.11
50	0.276	0.045	7.225	58.2	1.49
60	0.329	0.053	10.00	57.4	2.05
70	0.377	0.051	10.45	54.7	2.16
80	0.433	0.063	15.00	55.3	3.11
90	0.497	0.086	24.29	57.0	5.01
100	0.569	0.117	38.55	57.8	7.96

Table A2: Electrochemical efficiencies of GQD:G 1:1

Parameters					
Scan rate	J_{sc} (µA)	V_{oc} (V)	P_{max} (nW)	FF (%)	Ef (%)*e-6
10	0.021	40.583	0.369	43.7	0.076
20	4.882	0.252	0.432	35.2	0.089
30	6.604	0.270	0.593	33.2	0.122
40	9.202	0.395	1.204	33.1	0.248
50	14.34	0.521	1.894	25.4	0.391
60	21.34	0.754	3.294	20.5	0.680
70	36.00	0.772	5.487	19.9	1.130
80	59.00	0.814	8.621	17.9	1.780
90	104.0	0.874	14.80	16.3	3.050
100	387.0	0.938	0.049	13.6	0.010

Table A3: Electrochemical efficiencies of GQD:G 1:3

Parameters					
Scan rate	J_{sc} (µA)	V_{oc} (µV)	P_{max} (nW)	FF (%)	Ef (%)*e-6
10	25.0	1.262	0.033	104	6.72
20	27.0	2.333	0.074	118	15.3
30	30.0	3.411	0.119	117	24.5
40	4.32	20000	0.092	106	19.0
50	5.28	22250	0.113	95.9	23.2
60	6.34	0.020	0.116	91.0	24.0
70	7.46	0.024	0.149	84.1	30.8
80	8.25	20450	0.133	78.6	27.4
90	9.42	0.026	0.193	78.4	39.9
100	25.0	0.088	0.601	27.3	0.124

Table A4: Electrochemical efficiencies of GQD:G 1:6

Parameters					
Scan rate	J_{sc} (mA)	V_{oc} (V)	P_{max} (µmW)	FF (%)	Ef (%)*e-3
10	0.010	0.028	0.129	48.5	0.027
20	0.016	0.030	0.241	51.0	0.050
30	0.021	0.034	0.368	51.0	0.076
40	0.027	0.039	0.539	51.3	0.111
50	0.034	0.046	0.789	51.0	0.163
60	0.039	0.047	0.932	51.6	0.192
70	0.047	0.057	1.367	50.6	0.282
80	0.056	0.066	1.831	49.9	0.378
90	0.059	0.059	1.799	51.6	0.371
100	0.073	0.075	2.606	47.8	0.538

Table A5: Electrochemical efficiencies of GQD:G 3:1

Parameters					
Scan rate	J_{sc} (µA)	V_{oc} (V)	P_{max} (µW)	FF (%)	Ef (%)*e-6
10	0.697	0.129	0.037	41.6	7.71
20	0.943	0.076	0.036	49.6	7.34
30	1.167	0.055	0.044	68.9	9.17
40	1.385	0.051	0.066	93	13.6
50	1.632	0.050	0.095	116	19.5
60	1.824	0.047	0.070	81.6	14.5
70	2.044	0.042	0.092	106	19.0
80	2.232	0.040	0.099	112	20.5
90	2.507	0.046	0.118	102	24.4
100	3.745	0.149	0.492	88.3	101

Table A6: Electrochemical efficiencies of Al nanoparticles

Parameters					
Scan rate	J_{sc} (µA)	V_{oc} (V)	P_{max} (nW)	FF (%)	Ef (%)*e-6
10	0.045	0.097	2.116	48	0.44
20	0.068	0.047	1.599	50.7	0.33
30	0.084	0.033	1.440	51.2	0.30
40	0.106	0.037	0.002	50.5	0.41
50	0.123	0.032	1.930	49.3	0.40
60	0.137	0.027	1.805	48.7	0.37
70	0.148	0.026	1.836	48.5	0.38
80	0.157	0.026	0.002	50.1	0.41
90	0.182	0.024	2.038	46.2	0.42
100	0.192	0.023	2.073	47.4	0.43

Table A7: Electrochemical efficiencies of GQD:Al 1:1

Parameters					
Scan rate	J_{sc} (µA)	V_{oc} (V)	P_{max} (nW)	FF (%)	Ef (%)*e-6
10	0.070	0.075	2.05	39	0.424
20	0.099	0.071	3.00	42.5	0.616
30	0.128	0.073	3.96	42.4	0.817
40	0.154	0.077	5.09	42.6	1.050
50	0.180	0.082	6.26	42.6	1.290
60	0.195	0.084	7.00	43.4	1.460
70	0.219	0.093	8.79	43.1	1.810
80	0.244	0.103	10.6	42	2.190
90	0.264	0.110	12.0	41.2	2.470
100	0.291	0.127	15.0	40.4	3.080

Table A8: Electrochemical efficiencies of GQD:Al 1:3

Parameters					
Scan rate	J_{sc} (µA)	V_{oc} (mV)	P_{max} (nW)	FF (%)	Ef (%)*e-6
10	0.047	14.72	0.273	39.2	0.056
20	0.067	13.28	0.353	39.6	0.073
30	0.080	13,00	0.423	40.5	0.087
40	0.092	12.54	0.538	46.6	0.111
50	0.101	12.43	0.557	44.2	0.115
60	0.113	12.18	0.617	44.8	0.127
70	0.127	11.82	0.673	44.7	0.139
80	0.134	11.70	0.720	45.9	0.149
90	0.146	11.42	0.775	46.6	0.160
100	0.160	11.61	0.867	46.5	0.179

Table A9: Electrochemical efficiencies of GQD:Al 1:6

Parameters					
Scan rate	J_{sc} (µA)	V_{oc} (V)	P_{max} (nW)	FF (%)	Ef (%)*e-6
10	38.42	0.047	0.646	35.6	0.133
20	0.047	0.034	1.330	84.0	0.275
30	0.052	0.034	0.758	42.6	0.156
40	0.060	0.034	0.894	43.6	0.184
50	0.071	0.036	1.714	66.9	0.354
60	0.081	0.034	1.204	43.9	0.249
70	0.086	0.034	1.400	48.0	0.289
80	0.093	0.033	1.430	46.7	0.295
90	0.096	0.032	1.720	56.0	0.355
100	0.104	0.032	1.805	54.2	0.373

Table A10: Electrochemical efficiencies of GQD:Al 3:1

Parameters					
Scan rate	J_{sc} (nA)	V_{oc} (mV)	P_{max} (nW)	FF (%)	Ef (%)*e-9
10	2.09	4.591	0.005	48.2	0.954
20	3.00	3.232	0.008	82.5	1.640
30	7.39	3.100	0.010	43.4	2.050
40	7.69	2.627	0.010	50	2.080
50	7.72	3.782	0.010	34.1	2.050
60	6.72	2.431	0.012	73.2	2.470
70	10.3	3.038	0.015	48.5	3.150
80	12.2	4.202	0.017	32.4	3.430
90	12.7	4.000	0.019	37.7	3.950
100	13.0	4.125	0.020	37.5	4.140

Table A11: Electrochemical efficiencies of Au nanoparticles

Parameters					
Scan rate	J_{sc} (µA)	V_{oc} (V)	P_{max} (nW)	FF (%)	Ef (%)*e-6
10	0.059	0.039	1.055	45.5	0.218
20	0.095	0.045	0.002	46.7	0.414
30	0.124	0. 051	3.068	48.6	0.633
40	0.161	0.063	4.859	47.4	1.00
50	0.184	0.057	5.175	49.4	1.00
60	0.233	0.077	8.200	45.7	1.69
70	0.245	0.067	7.786	47.6	1.61
80	0.280	0.075	9.832	47	2.03
90	0.318	0.090	13.00	45.7	2.70
100	0.366	0.109	17.50	43.8	3.61

Table A12: Electrochemical efficiencies of GQD:Au 1:1

Parameters					
Scan rate	J_{sc} (µA)	V_{oc} (V)	P_{max} (nW)	FF (%)	Ef (%)*e-6
10	0.080	0.087	0.003	43.2	0.617
20	0.105	0.051	2.314	43.3	0.478
30	0.122	0.039	2.848	60.2	0.588
40	0.145	0.036	2.314	43.9	0.478
50	0.161	0.034	3.851	71.2	0.795
60	0.173	0.031	2.671	49.4	0.551
70	0.200	0.035	3.181	46	0.657
80	0.205	0.033	3.638	53.5	0.751
90	0.233	0.034	4.045	51.8	0.835
100	0.335	0.073	10.58	43.2	2.180

Table A13: Electrochemical efficiencies of GQD:Au 1:3

Parameters					
Scan rate	J_{sc} (µA)	V_{oc} (mV)	P_{max} (nW)	FF (%)	Ef (%) *e-6
10	0.056	11.4	0.368	57.4	0.076
20	0.093	9.73	0.498	54.9	0.103
30	0.135	11.0	0.767	51.9	0.158
40	0.165	11.2	0.949	51.4	0.196
50	0.199	12.6	1.315	52.4	0.271
60	0.234	14.7	1.784	51.7	0.368
70	0.276	17.3	2.481	51.7	0.512
80	0.317	21.4	3.533	52.0	0.729
90	0.376	29.0	5.591	51.7	1.150
100	0.448	45.0	10.24	51.2	2.110

Table A14: Electrochemical efficiencies of GQD:Au 1:6

Parameters					
Scan rate	J_{sc} (µA)	V_{oc} (mV)	P_{max} (nW)	FF (%)	Ef (%) *e-6
10	0.056	11.4	0.368	57.4	0.076
20	0.093	9.73	0.498	54.9	0.103
30	0.135	11.0	0.767	51.9	0.158
40	0.165	11.2	0.949	51.4	0.196
50	0.199	12.6	1.315	52.4	0.271
60	0.234	14.7	1.784	51.7	0.368
70	0.276	17.4	2.481	51.7	0.512
80	0.317	21.4	3.533	52.0	0.729
90	0.376	29.0	5.591	51.7	1.15
100	0.448	45.0	10.23	51.2	2.11

Table A15: Electrochemical efficiencies of GQD:Au 3:1

Parameters					
Scan rate	J_{sc} (µA)	V_{oc} (mV)	P_{max} (nW)	FF (%)	Ef (%) *e-6
10	0.129	18.0	1.06	45.1	0.218
20	0.199	18.7	1.77	47.6	0.364
30	0.266	19.0	2.41	47.5	0.498
40	0.321	20.0	3.11	48.4	0.642
50	0.380	21.3	3.93	48.5	0.810
60	0.438	22.7	4.87	48.9	1.00
70	0.498	24.7	6.00	48.8	1.24
80	0.526	22.0	5.79	50.4	1.19
90	0.582	23.5	7.10	51.9	1.47
100	0.648	26.0	8.72	51.4	1.80

Table A16: Electrochemical efficiencies of Al nanoparticles

Parameters					
Scan rate	J_{sc} (µA)	V_{oc} (V)	P_{max} (nW)	FF (%)	Ef (%) *e-6
10	0.059	0.039	1.06	45.5	0.218
20	0.095	0.045	2.00	46.7	0.414
30	0.124	0. 051	3.07	48.6	0.633
40	0.161	0.063	4.86	47.4	1.00
50	0.184	0.057	5.18	49.4	1.07
60	0.233	0.077	8.20	45.7	1.69
70	0.245	0.067	7.79	47.6	1.61
80	0.280	0.075	9.83	47	2.03
90	0.318	0.090	130	45.7	2.70
100	0.366	0.109	17.49	43.8	3.61

Table A17: Electrochemical efficiencies of GQD

Parameters					
Scan rate	J_{sc} (µA)	V_{oc} (mV)	P_{max} (µmW)	FF (%)	Ef (%) *e-9
10	0.058	8.79	0.238	46.7	49.1
20	0.090	8.17	0.356	48.5	73.4
30	0.116	8.00	0.478	51.4	98.6
40	0.151	7.88	0.591	49.6	122
50	0.155	8.41	0.742	56.8	153
60	0.190	9.32	0.979	55.3	202
70	0.219	8.612	1.052	55.7	217
80	0.248	9.00	1.291	58.1	267
90	0.267	9.56	1.576	61.7	325
100	0.277	9.76	1.591	58.8	328